ABSTRACT

Title of Document: SEMICONDUCTING CARBON NANOTUBE TRANSISTORS: ELECTRON AND SPIN TRANSPORT PROPERTIES

Yung-Fu Chen, Doctor of Philosophy, 2006

Directed By: Associate Professor, Michael S. Fuhrer, Department of Physics

Single-walled carbon nanotubes (SWNTs) have attracted great interest both scientifically and technologically due to their long mean free paths and high carrier velocities at room temperature, and possibly very long spin-scattering lengths. This thesis will describe experiments to probe the charge-and spin-transport properties of long, clean individual SWNTs prepared by chemical vapor deposition and contacted by metal electrodes.

A SWNT field-effect transistor (SWNT-FET) has been shown to be sensitive to single electrons in charge traps. A single charge trap near a SWNT-FET is explored here using both electronic and scanned-probe techniques, and a simple model is developed to determine the capacitances of the trap to the SWNT and gate electrode.

SWNTs are contacted with ferromagnetic electrodes in order to explore the transport of spin-polarized current through the SWNT. In some cases spin-dependent

transport was observed, verifying long spin scattering lengths in SWNT. However, in many cases no spin-dependent effects were observed; these results will be discussed in the context of the present state of results in the literature.

Semiconducting SWNTs (s-SWNTs) with Schottky-barrier contacts are measured at high bias. Nearly symmetric ambipolar transport is observed, with electron and hole currents significantly exceeding 25 μA, the reported current limit in m-SWNTs. Four simple models for the field-dependent velocity (ballistic, current saturation, velocity saturation, and constant mobility) are studied in the unipolar regime; the high-bias behavior is best explained by a velocity saturation model with a saturation velocity of 2×10^7 cm/s. A simple Boltzmann equation model for charge transport in s-SWNTs is developed with two adjustable parameters, the elastic and inelastic scattering lengths. The model predicts velocity saturation rather than current saturation in s-SWNTs, in agreement with experiment.

Contact effects in s-SWNT-FET are explored by electrically heating the devices. These experiments resolve the origin of nanotube p-type behavior in air by showing that the observed p-type behavior upon air exposure cannot be explained by change in contact work function, but is instead due to doping of the nanotube. Modest doping of the SWNT narrows the Schottky Barriers and provides a high-conductance Ohmic tunnel contact from electrode to SWNT.

SEMICONDUCTING CARBON NANOTUBE TRANSISTORS: ELECTRON AND SPIN TRANSPORT PROPERTIES

By

Yung-Fu Chen

Dissertation submitted to the Faculty of the Graduate School of the
University of Maryland, College Park, in partial fulfillment
of the requirements for the degree of
Doctor of Philosophy
2006

Advisory Committee:
Associate Professor Michael S. Fuhrer, Chair
Professor Richard L. Greene
Assistant Professor Min Ouyang
Professor Neil Goldsman
Associate Professor Romel D. Gomez

Acknowledgements

About six years ago, I left my family to pursue higher physics education in the US. My parents, sister and brother were full of tears while we were in the airport, so was I. We had not separated before, so it was a hard time for all of us. When I sometimes recall that moment, I still struggle whether this travel is worthy. Thank you so much for your support through the period I study in the US.

In physics department, I am lucky to have so many nice classmates: Mike, Hanhee, Tor, Minyoung, Xing, Junjie, Tosh, … We not only shared the homework when we took courses in the first year study, but also share life of the whole graduate study.

I would like to show special appreciation to my advisor of my research study, Prof. Michael Fuhrer. He encourages me in many ways, especially when I make no progress at all. Although he offers me many great suggestions in my study to push me on the right track, he gives me a lot of freedom to work on the things I enjoy, which I believe will help me do research independently in the future. In my memory, he has not blamed me; of course it is not because I am perfect, but he is so patient. There was only once I felt he was not happy: I was not able to finish printing the PowerPoint slides and give a presentation on time when I gave my first talk in the Center. I then had better sense of doing things ahead of time. He also serves as a great model to utilize time efficiently for me. Also his wife, Cynthia, always welcomes me and warms my shy heart.

I am glad that I have so many considerate and supportive labmates. I bother them whenever I want: Todd teaches me the most basic and important things to begin

with as an experimentalist; Enrique reads every kind of my drafts; Tobias shares his favorite music with me; Dave eats lunch in the lab with me the most; Gohkan's dreams about future look so realistic to me; Adrian always lets me know how much he likes the dish I cook; Anthony is willing to discuss physics with me when he knows what is going on and I don't; Stephanie still invites me to join lunch even I keep saying no to her; Byong always encourages to do good research; Tarek shows his friendship to me in many ways; Dan and Alex let me know how to devote yourself to something interesting, like bicycles; Sungjae likes to share his physics ideas with me; Sasha let me know how good a fresh Ph.D. can be; … Right, also thank Masa for encouraging and helping me search postdoc positions. There are countless memories in Fuhrer lab.

I thank my dissertation committee, Prof. Richard Greene, Prof. Ouyang Min, Prof. Neil Goldsman and Prof. Romel Gomez, for their precious time and suggestions to help me improve my dissertation. I am grateful for the help from Prof. Romel Gomez with the aid of his student Seok-Hwan Chung when I studied spin transport in nanotubes, and for useful discussions of high bias transport in nanotubes with Prof. Neil Goldsman.

Thank you all the hardworking staff in our department. Because of you, I do not worry about the administrative work that I am not good at.

My roommates in Maryland, Che-Rong, Daw-Wei and Shu-Hsien, Yi-Te, Yao-Hing, Chung-Ching and Wei-Yen, taught me how to live with people. We spent many hours together, and thank them for bearing my unacceptable behaviors and words sometimes.

I meet so many good friends in Maryland Chinese Bible Study Group and Chinese Bible Church at College Park, who follow the teachings in Bible, and therefore treat me just as their brother. You are indeed my family, especially Prof. Chang, like father of many. Thank you very much for helping me to seek the One who creates me, and therefore I see the meaning of my life. I know I am forgiven because my personal savior, Jesus Christ, pays my debts. May God use my temporary life in the world as a channel of blessing to others.

During my graduate study, how lucky I am that I can meet my lovely wife, Hsin-Ping. We talk together, sing together and walk together. We will do that till the end of one of our lives. I thank my parents-in-law because they agree to let their daughter to marry a guy who is nothing and has nothing.

I will miss my graduate study here because all of you.

Table of Contents

List of Tables

List of Figures

Chapter 1

Introduction to Carbon Nanotubes

1.1 Nanotube Overview

Carbon nanotubes (CNTs) are novel materials which were discovered over a decade ago [1], and studied [2,3] intensively ever since. Single-walled carbon nanotubes (SWNTs) [4] consist of a single graphite sheet wrapped into a seamless tube, while multi-walled carbon nanotubes (MWNTs) have several concentric graphite shells. They are extremely tiny (in nanometer scale in diameters), but nonetheless have been studied individually in a variety of experiments [5-18]. They can be extremely long (nanotubes of length 4 cm [19] and 10 cm [20] have been reported, apparently limited only by the furnace sizes [20]), which is good for various applications. They are one of the few one-dimensional materials grown in nature, and have many exceptional mechanical [5,6], chemical [7-9], and electrical properties [10-18] which open doors to various kinds of researches and applications.

The carbon-carbon sp^2 bond in CNTs is one of the strongest chemical bonds in nature. Such bonds make CNTs very strong [21]. Combined with chemical cross-linked techniques [22], CNTs make the strongest fibers in the world, and CNTs have been suggested as a material for a continuous cable tethered to a satellite in geosynchronous orbit, an “elevator to space” [23].

Every carbon atom in SWNTs is a surface atom, which makes SWNTs electronic properties very sensitive to their environment, especially to the electron

donors or acceptors which are physically absorbed on SWNTs. Such a unique material geometry makes SWNTs very good candidates for chemical sensors.

Based on unique electronic properties, SWNTs can be metallic or semiconducting as predicted theoretically [10,12] and observed experimentally [13-17], depending on their chirality. (Some metallic SWNTs will have a gap open due to surface curvature and become small-gap semiconducting SWNTs. [24]) Many electronics applications of SWNTs, such as molecular circuit interconnects [25], single electron transistors (SETs) [26], p-n junctions [27], high mobility field-effect transistors (FETs) [28], nonvolatile memory elements [29], logic circuits, field emission elements [30,31], and so on, have been proposed and realized.

Luttinger liquid (LL) behaviors are predicted in general one-dimensional electron systems due to non-negligible electron-electron interaction [11,32]. In CNTs, researchers have for the first time found experimental evidence of LL behavior [33,34].

Due to weak spin-orbital coupling in carbon-based material, spin-scattering lengths are predicted to be very long in CNTs. CNTs should be a very good conductor to preserve spin information during transport. Spin-related transport in both MWNTs [35] and SWNTs [36,37] have also been proposed and realized.

Containing such rich physics and applications, CNTs have attracted the attention of many researchers, including myself. My work is mainly concentrated on electrical properties of SWNTs, although I am also interested in other properties of CNTs.

1.2 Electronic Band Structure

To understand the CNT electronic band structure, we start with its family material: graphene, a single graphite sheet. Figure 1-1 shows a honeycomb graphene sheet, a simple two-dimensional hexagonal Bravais lattice, with bases containing two identical carbon atoms. Each black dot and red bar represents a carbon atom and a carbon-carbon sp^2 bond, respectively. The carbon-carbon distance $a_{C\text{-}C}$ in graphite is 1.42 Å.

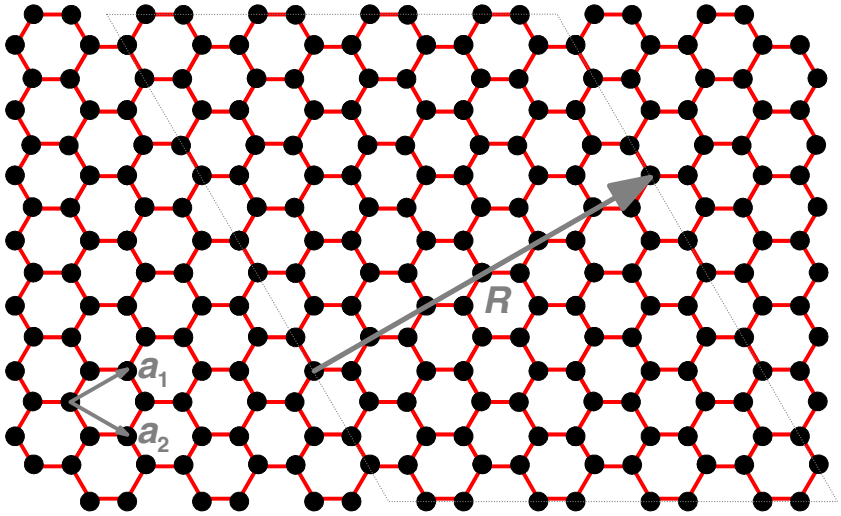

Figure 1-1. Hexagonal lattice of a graphene. $\boldsymbol{a_1}$, $\boldsymbol{a_2}$ are primitive vectors. $\boldsymbol{R}$ is a nanotube rolling vector. In the case the figure represents, $\boldsymbol{R} = 6\boldsymbol{a_1}$.

In structure, SWNT is a seamless tube of rolled graphene. Depending on how a graphene is rolled, various SWNTs can be formed. Conceptually, a rolling vector $\boldsymbol{R} = n\boldsymbol{a_1} + m\boldsymbol{a_2}$ is picked on the graphite sheet, starting from one carbon atom and ending at another. Then the strip whose sides are perpendicular to $\boldsymbol{R}$ and passing the start and the end of $\boldsymbol{R}$ is determined. The strip is rolled along $\boldsymbol{R}$, connecting the start and the end of $\boldsymbol{R}$, to form the SWNT. A SWNT is usually characterized by a pair of

indexes (n, m). Figure 1-2 shows three types of SWNTs: (a) armchair SWNTs with indexes (n, n), (b) zigzag SWNTs with indexes (n,0) and (c) chiral SWNTs with indexes (n, m) other than the previous two specifically symmetric indexes.

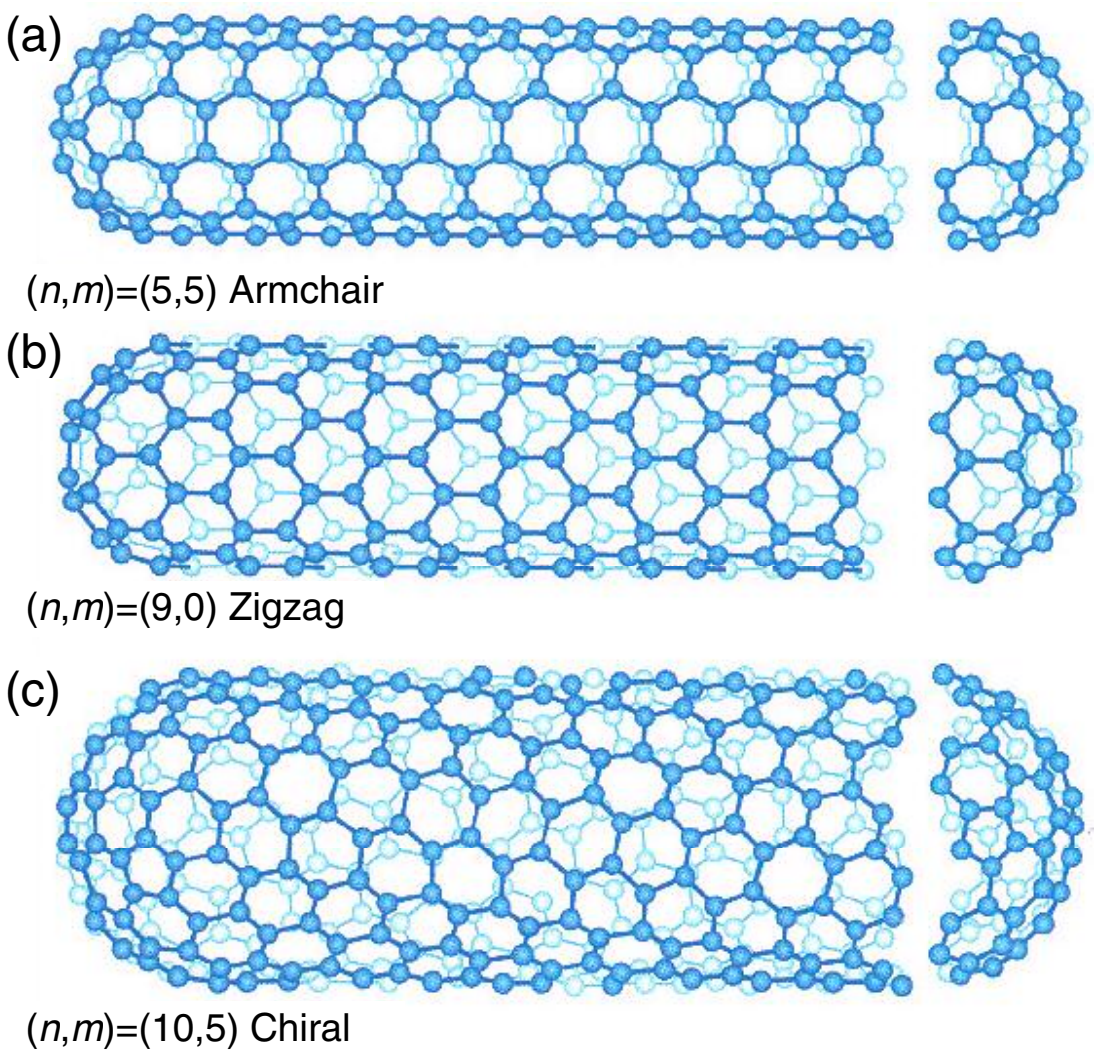

Figure 1-2. SWNTs with different chiralities. (a) (5, 5) armchair SWNT. (b) (9, 0) zigzag SWNT. (c) (10, 5) chiral SWNT. (courtesy R. E. Smalley)

SWNT electronic band structures are close related to graphene band structure due to the similarity between SWNTs and graphene. In 1947, P. R. Wallace wrote

down the graphene two-dimensional electronic dispersion relation of the π bonding band (lower sign) and the π^* anti-bonding band (upper sign)[38] :

$$E_{2D}(k_x, k_y) = \pm\gamma_0\left(1 + 4\cos\left(\frac{\sqrt{3}k_x a}{2}\right)\cos\left(\frac{k_y a}{2}\right) + 4\cos^2\left(\frac{k_y a}{2}\right)\right)^{\frac{1}{2}} \quad \text{Equation 1-1}$$

approximated by tight binding calculation, where γ_0 = 2.89 eV [39] is the nearest-neighbor carbon-carbon overlap integral, and $a = |\boldsymbol{a_1}| = \sqrt{3}a_{C\text{-}C}$ is the length of primitive vectors ($a_{C\text{-}C}$ = 1.44 Å in nanotubes, which is slightly larger than $a_{C\text{-}C}$ in graphite) [40,41]. The π^* band and the π band are degenerate at *K* and *K′* points. Figure 1-3(a) shows the graphene band structure in reciprocal space near the Fermi surface: the gray bands (π^* band) are empty; the yellow bands (π band) are filled; the six points at the hexagon corners (*K*, *K′*) are Fermi surfaces or Fermi points. Therefore, graphene is a semi-metal. Near the Fermi surface, the bands can be approximated to cones, and the dispersion relation is linear.

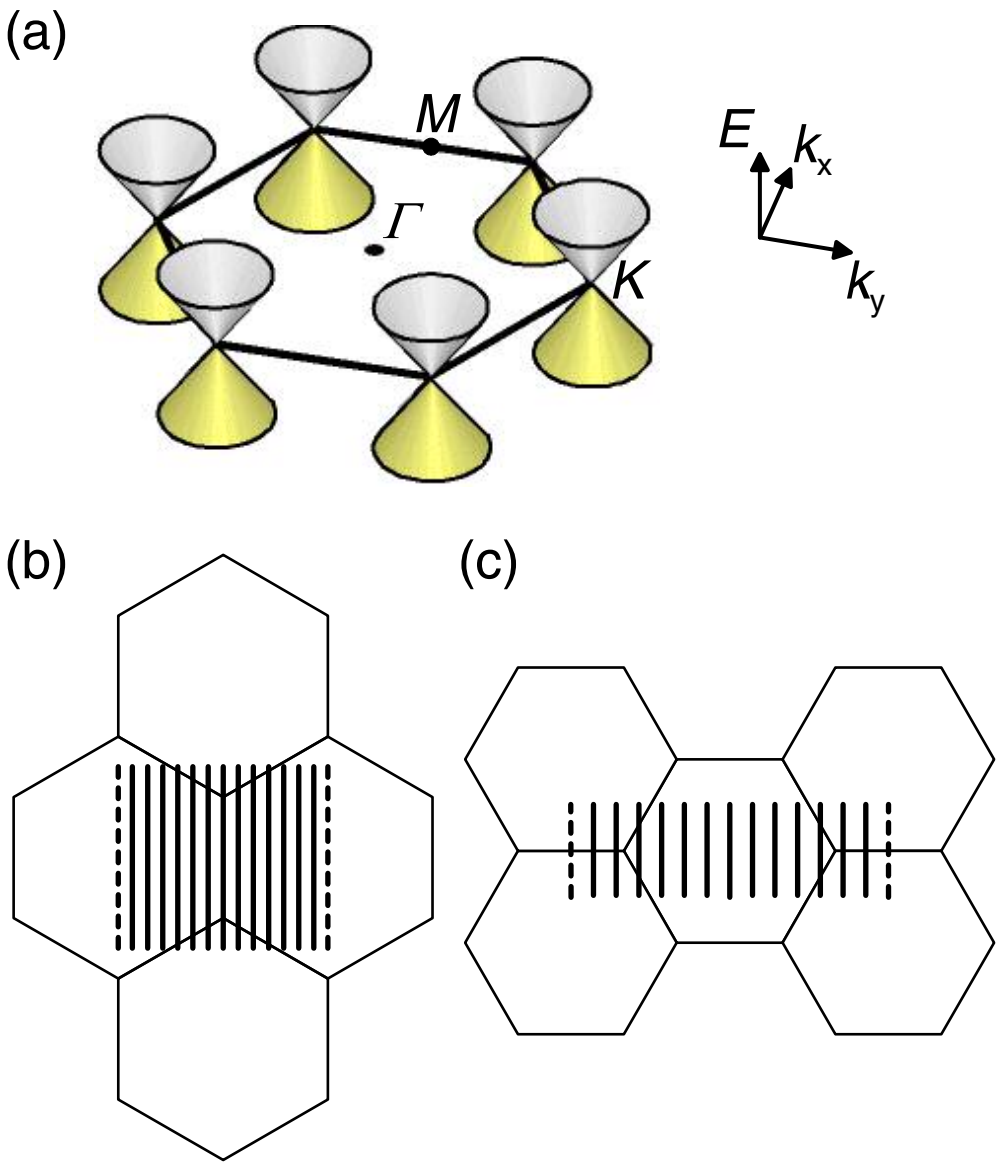

Figure 1-3. Graphite approximate electronic band structure and zone folding method. (a) Graphite approximate electronic band structure. Allowed k state in a reduced zone (b) in (7, 7) SWNT, and (c) in (7, 0) SWNT.

Not all the k-states of graphene are available for SWNTs since they are quasi-one-dimensional material. Due to the tubular structure of SWNTs, the phase of the electron wavefunction has to be identical when traveling one complete circumference of the tube; that is, $k_r|\boldsymbol{R}| = 2\pi n$, where n is an integer. This causes a quantization of

the wavevector along the circumferential direction, k_r [10]. Figure 1-3(b) and (c) show the examples of quantized k_r in graphene reciprocal space in an extended-zone scheme. The thick lines are allowed *k*-states, and the dashed lines represent identical states in a reduced-zone scheme. Such a method to determine SWNTs allowed *k*-states is called the zone folding method [40,41].

The energies corresponding to SWNTs' allowed *k*-states make one dimensional subbands. When $n - m$ is not multiple of 3, where (n, m) are the indexes of a SWNT, the allowed *k*-states contain the Fermi points of graphene (K, K'), and the dispersion relation looks like Figure 1-4(a). The first subbands are crossing each other; there is no gap between them. The tube is metallic. Otherwise, the dispersion relation looks like Figure 1-4(b). There is a bandgap between the first valence bands and conduction bands. The tube is semiconducting. The bandgap is

$$E_g = 2\Delta = \frac{2\gamma_0 a_{C-C}}{d} \approx \frac{830\,\text{meV}}{d\,[\text{nm}]}, \qquad \text{Equation 1-2}$$

where

$$d = a\sqrt{n^2 + m^2 + nm}\Big/\pi \qquad \text{Equation 1-3}$$

is the diameter of the tube. Here we see nanotubes are direct bandgap materials.

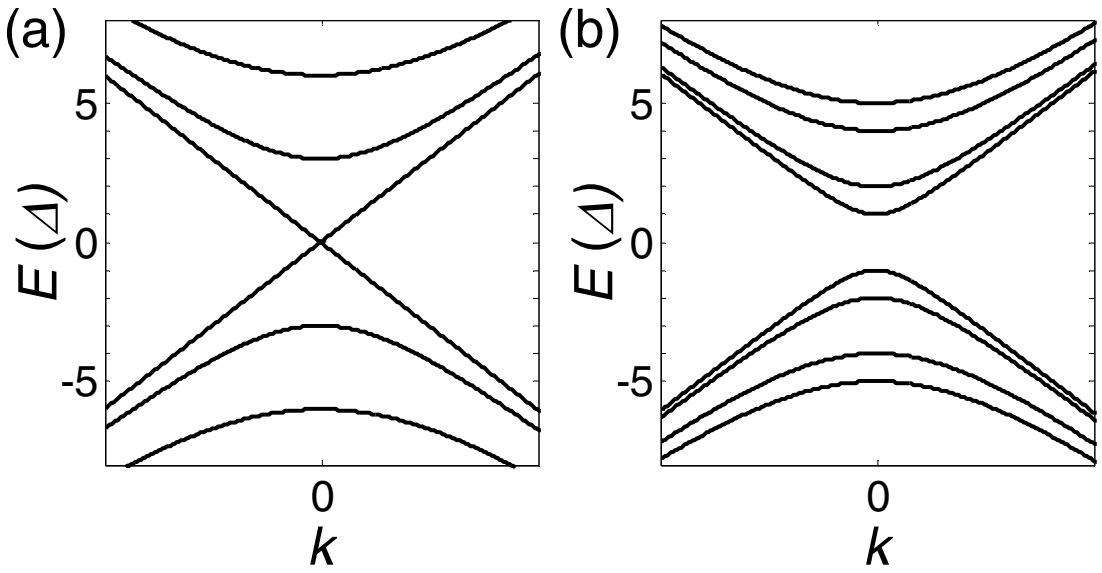

Figure 1-4. Electronic band structure of SWNTs. (a) Metallic SWNT. (b) Semiconducting SWNT.

The dispersion relations of SWNTs can be approximated by the universal dispersion relations [18]:

$$E(k) = \pm\sqrt{(\frac{\hbar v_{\mathrm{F,m}} k}{2})^2 + (\nu\Delta)^2}\ , \qquad \text{Equation 1-4}$$

where ν = 0, 3, 6, 9, … for metallic nanotubes, ν = 1, 2, 4, 5, 7, 8, … for semiconducting nanotubes, $\hbar = \frac{h}{2\pi}$ (h is Planck's constant), and $v_{\mathrm{F,m}}$ = 9.3 × 10^7 cm/s is the Fermi velocity of graphene (the upper and lower signs are for conduction and valance bands, respectively). Each subband of the metallic nanotubes has a degeneracy of four (except ν = 0 has degeneracy of two), but each subband of the semiconducting nanotubes has a degeneracy of two.

1.3 Electronic Properties

As mentioned in section 1.2, SWNTs are either metallic or semiconducting. This aspect of SWNTs has been confirmed experimentally in electronic transport measurement by many research groups. Figure 1-5 shows the transfer characteristic curves of two types of nanotube devices in FET geometry (this will be discussed in more detail in Chapter 2). Figure 1-5(a) shows a metallic SWNT device, where the conductance is almost independent of a gate bias. Figure 1-5(b) shows a semiconducting SWNT device, where the conductance is modulated by a gate bias, like a FET. Each of them is very useful and promising for future electronic applications.

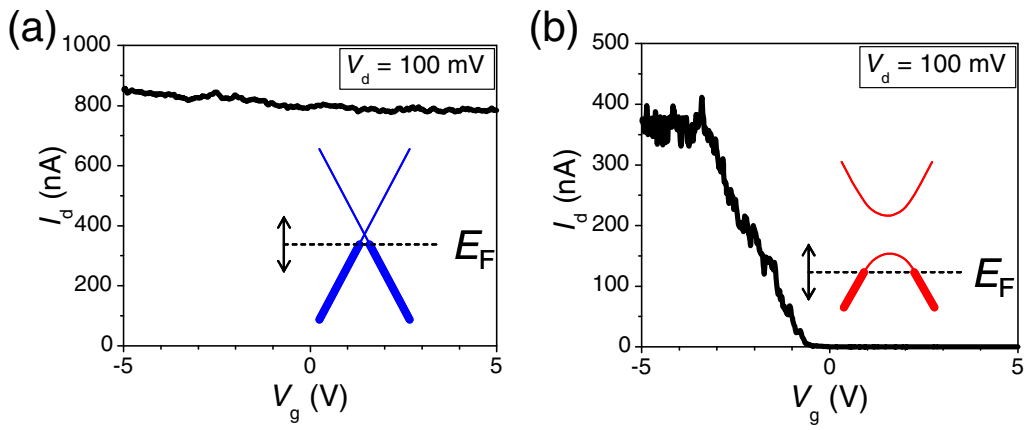

Figure 1-5. Transfer characteristic curves of (a) metallic SWNT, and (b) semiconducting SWNT.

Nanotubes have long mean free paths for electron transport. Ballistic transport has been observed in both metallic [42,43] and semiconducting SWNTs [44] over micron length scales at low biases. In the diffusive regime, SWNTs can carry current density up to 10^9 A/cm^2, as observed for both metallic [45] and

semiconducting SWNTs [46]. This current density is about 3 orders of magnitude better than that at which copper wires typically fail due to electromigration, while CNTs are robust at such high current densities in air and at elevated temperatures [47]. The current-carrying reliability studies of MWNTs under current densities grater than 10^9 A/cm^2 show no observable failure in the nanotube structure and no measurable change in the resistance are detected up to 2 weeks [48]. CNTs are therefore very good for interconnections. Also SWNTs have extremely high mobility (over 10^5 cm^2/Vs at room temperature) in the low electric field [28], and very high carrier velocity (~ 2×10^7 cm/s) in the high electric field regime [46]. Nanotubes are direct bandgap materials (with bandgap sizes a few hundreds of meV according to , Equation 1-2), and an electrically-driven infrared light emitter has also been demonstrated [49].

In my dissertation I will focus on CNTs electronic transport properties in several aspects. In Chapter 3 I will talk about how to use scanning probe microscopy (SPM) to characterize CNTs, especially in two techniques: electrostatic force microscopy (EFM) and scanned-gate microscopy (SGM). In Chapter 4 I will demonstrate using SGM technique detects a local defect in a nanotube single electron memory device. In Chapter 5 I will discuss spin-related magnetoresistance with CNTs as channels and recent progresses in this field. In Chapter 6 to 9 I will focus on high bias transport in semiconducting SWNTs in both unipolar and ambipolar regimes, and discuss how electron-phonon interactions affect semiconducting SWNT devices behave. In Chapter 10 I will introduce electrical high-power treatment to

undope CNTs devices in vacuum, concluding that air-exposed doping explains high on-currents in Schottky-barrier nanotube transistors.

The materials in Chapter 4 have been published in the open literature as Ref. [50], Chapter 6 and 7 as [46], and Chapter 10 as [51].

Chapter 2

Nanotube Synthesis and Device Fabrication

2.1 Nanotube Chemical Vapor Deposition Synthesis

Carbon nanotubes were originally discovered as products of the arc discharge between graphite rods [1]. Researchers have since found more methods to synthesize nanotubes, such as laser ablation [52], and chemical vapor deposition (CVD) [53,54].

The advantages of CVD growth include producing very long [19], clean (fewer defects) [55] SWNTs, and also producing large amounts of SWNTs [56]. Our group grows the nanotubes by CVD methods to meet the purpose of producing very long, clean (few defects) SWNTs directly on substrates. Also the system is simple to set up (see Figure 2-1).

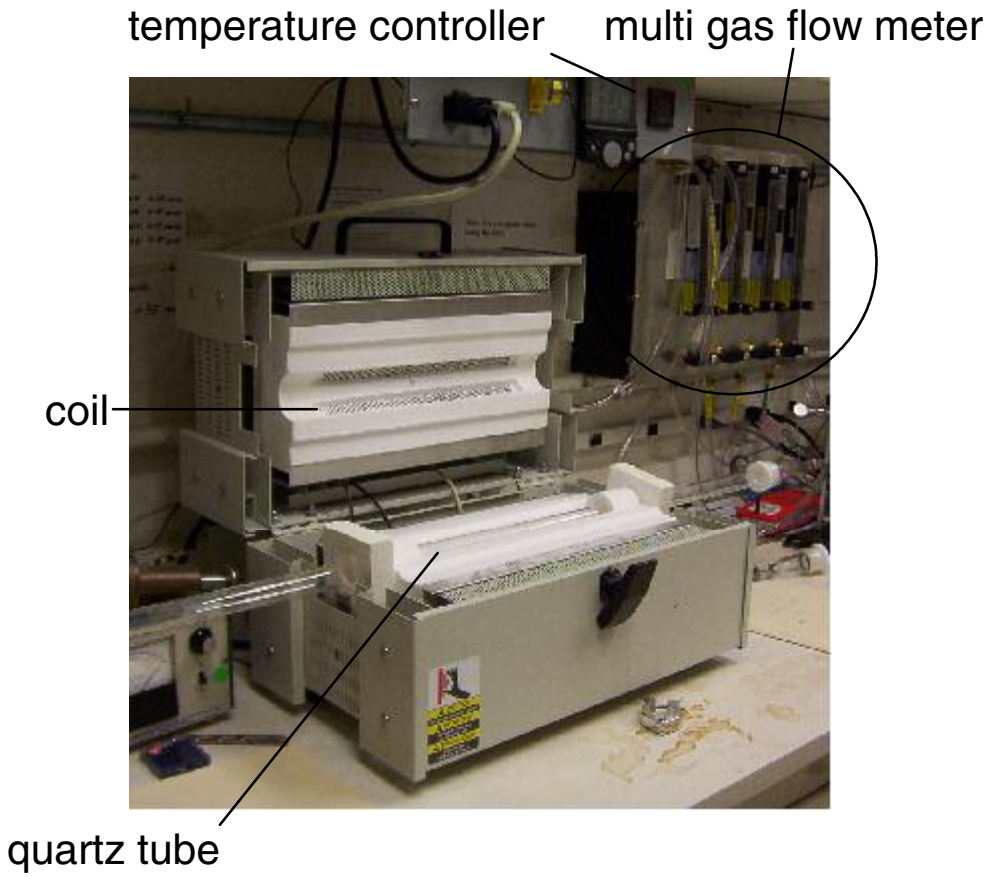

Figure 2-1. Nanotube chemical vapor deposition setup. The oven was bought from Lindberg/Blue. The gases from the cylinders (not shown here) flow through the flow meters and through the quartz tube. The oven heats the gases and samples, where the nanotubes grow. The temperature controller (from Omega) allows ramping, fixing the temperatures and timing.

Iron nanoparticles can catalyze the growth of CNTs and are used in our nanotube CVD growth [57]. The size of the iron nanoparticles is believed to determine the diameter of resulting nanotubes [58]. To prepare iron nanoparticles on the substrates (typically small chips of SiO_2-capped Si), ferric nitrate ($Fe(NO_3)_3$) is dissolved in an isopropyl alcohol (IPA) solution, and then mixed well by stirring for a couple of hours. The concentrations of $Fe(NO_3)_3$/IPA solution directly control the density of catalyst particles for nanotube growth. The substrates are dipped in

$Fe(NO_3)_3$/IPA solution for 10 seconds and hexane for another 10 seconds to force $Fe(NO_3)_3$ to precipitate on the substrates. The substrates are placed in a quartz boat and then the boat is placed in the quartz tube, in the center of the oven (see Figure 2-1). After the gas lines are purged, Ar and H_2 are introduced to the quartz tube and the oven starts heating toward 850 ^oC. During the heating, iron nitrate is expected to be reduced to iron nanoparticle catalyst. After the temperature is stabilized at 850 ^oC, the carbon feedstock gases, such as methane and ethylene, are fed into the oven. The carbon feedstock gases are expected to decompose catalytically over the iron to carbon and hydrogen; carbon atoms interact with the iron nanoparticles, and nanotubes grow. Nanotube growth ends when the carbon feedstock gases are shut off and the oven is cooled.

Table 2-1 shows a typical example of nanotube growth. The growth parameters, such as gases, flow rates, flow times, and temperatures, are all adjustable to optimize the growth yield or for other purposes (such as length or density control).

Action	Gas	Flow (sccm)	Temp (ºC)	Time (minute)
Purge	Ar	730	RT	22
Heat	Ar	730	RT→650	15
Soak	Ar	730	650	5
Heat	Ar	730	650→730	2
Soak	Ar	730	730	3
Heat	Ar	730	730→800	3
Soak	Ar	730	800	3
Heat	Ar	730	800→850	5
Soak	Ar	730	850	10
Nanotube Growth	H_2	1900	850	10
	CH_4	1300		
	C_2H_4	86		
Cool Down	Ar	730	850→RT	Wait for hours

Table 2-1. A recipe of nanotube growth.

Figure 2-2 shows an SEM image of nanotubes [59] grown according to the recipe of Table 2-1 with about 0.3 μg/ml (30μg/100ml) $Fe(NO_3)_3$/IPA. Most of the nanotubes are tens of microns long; some of the nanotubes are hundreds of microns long. The density of nanotubes is controllable by controlling the catalyst concentration. This sample, with long, well isolated nanotubes, is good for electrical device fabrication. By checking with atomic force microscopy (AFM, which will be described in next chapter), most of CVD-grown CNTs are thin (with diameters about 1~3 nm); therefore, most of them are expected to be SWNTs, although it is likely that some few-walled CNTs and small bundles of SWNTs are present.

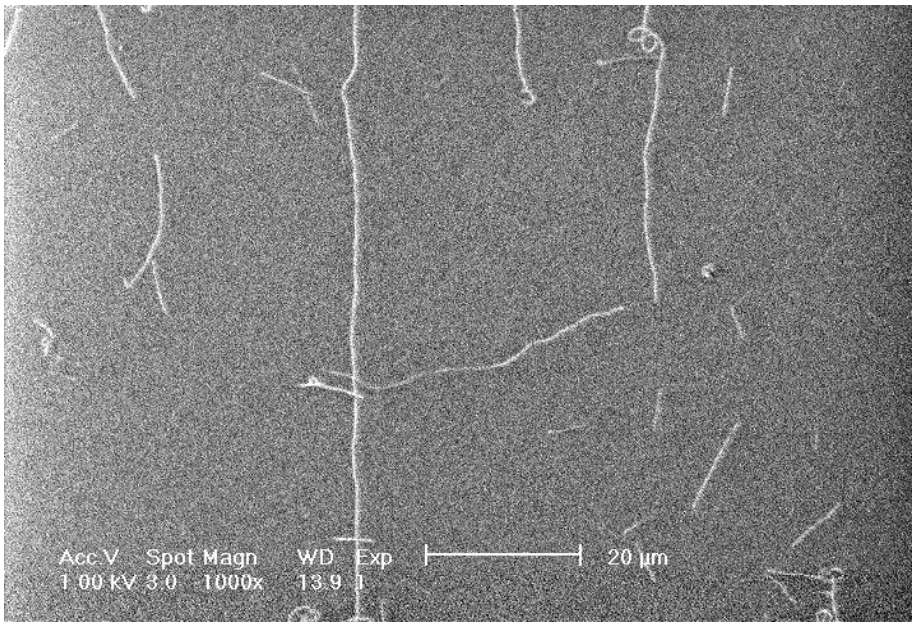

Figure 2-2. An SEM image of nanotubes on Si substrate.

2.2 Electron-Beam Lithography and Electrical Contact Preparation

When discussing the manufacture of electronic devices, lithography is the term used to describe the patterning of material on the surface of the substrate. Optical lithography, which uses light directed through a mask to create the pattern in a polymer resist layer (photoresist), is the most extensively used lithography technique in the electronics industry. In my study, however, electron-beam lithography is chosen to pattern thin films for device purposes because feature sizes from hundreds of microns down to tens of nanometers are easy to prepare. The major drawback of electron-beam lithography, that it is a serial process and therefore inherently slow due, is not a disadvantage here because each device is custom-designed for the particular nanotubes on a chip.

Making alignment marker patterns and nanotube contacts are two major steps during device fabrication with electron-beam lithography. Here we use a technique

called “find-and-wire” to fabricate nanotube devices. In the first lithography step alignment markers are made randomly on a chip with already grown nanotubes. We find the nanotubes relative to the alignment markers. Then we wire the nanotubes we find through the second lithography. The chief advantage of the find-and-wire technique is that the wired nanotubes can be chosen for specific purposes.

Figure 2-3 explains how electron-beam lithography works. Figure 2-3(a) shows a clean diced chip or wafer. Figure 2-3(b) shows a chip with bi-layer resists. Resists are the chemicals which are easy to cover the whole surface of chips and whose chemical structures are sensitive to exposure to energetic beams (light or electrons, for instance). Depending on the dosage, the solubility of resists in some specific solvents (developers) can be varied. The bottom layer is methyl methacrylate (MMA), and the top is polymethyl methacrylate (PMMA). Typically, MMA is spun on with 4500 rpm for 45 seconds, and followed by 5 ~10 minutes baking at 150 ^{o}C on a hot plate. PMMA is spun on with 6000 rpm for 45 seconds, and followed by 5 ~ 10 minutes baking at 150 ^{o}C on a hot plate. The resist thicknesses of MMA and PMMA layers are about 300 and 100 nm, respectively. The bi-layer resist is used to create big undercuts and ease the lift-off process (described below) because MMA is more sensitive to electron dosage and easy to dissolve in Acetone (the solvent which is used for lift-off). Sometime a single PMMA layer is prepared if an e-beam mask with very big undercut is not needed and/or the MMA does not coat the chip surface evenly. Figure 2-3(c) shows a part of resists exposed under the electron beam. The patterns to be exposed are designed with CAD software, and the Nano Pattern Generation System (NPGS) is used to control a Scanning Electron Microscope (SEM,

FEI model XL-30). The electron beam scans the patterns, so the resist at the desired locations is exposed to the electron beam. Figure 2-3(d) shows the resist after development; a larger portion of the more sensitive MMA layer is removed by the developer, creating an undercut. The resist developer is methyl isobutyl ketone (MIBK):IPA = 1:3. Typically the exposed resist can be removed in developer within 20 ~ 70 seconds, then followed by IPA cleaning. Figure 2-3(e) shows the chip after deposition of the contact material (usually a metal film prepared by thermal evaporation). Figure 2-3(f) shows the result of the lift-off step. After the resist is dissolved (typically in acetone) the contact material in the developed patterns remains on the surface, while the contact material on the resist has been removed. To accomplish lift-off, typically the chip is soaked in acetone for a few hours for most deposited materials. For some materials (like permalloy), lift-off can be done within minutes. Afterward, the chip is rinsed with acetone and IPA, completing the lithography process.

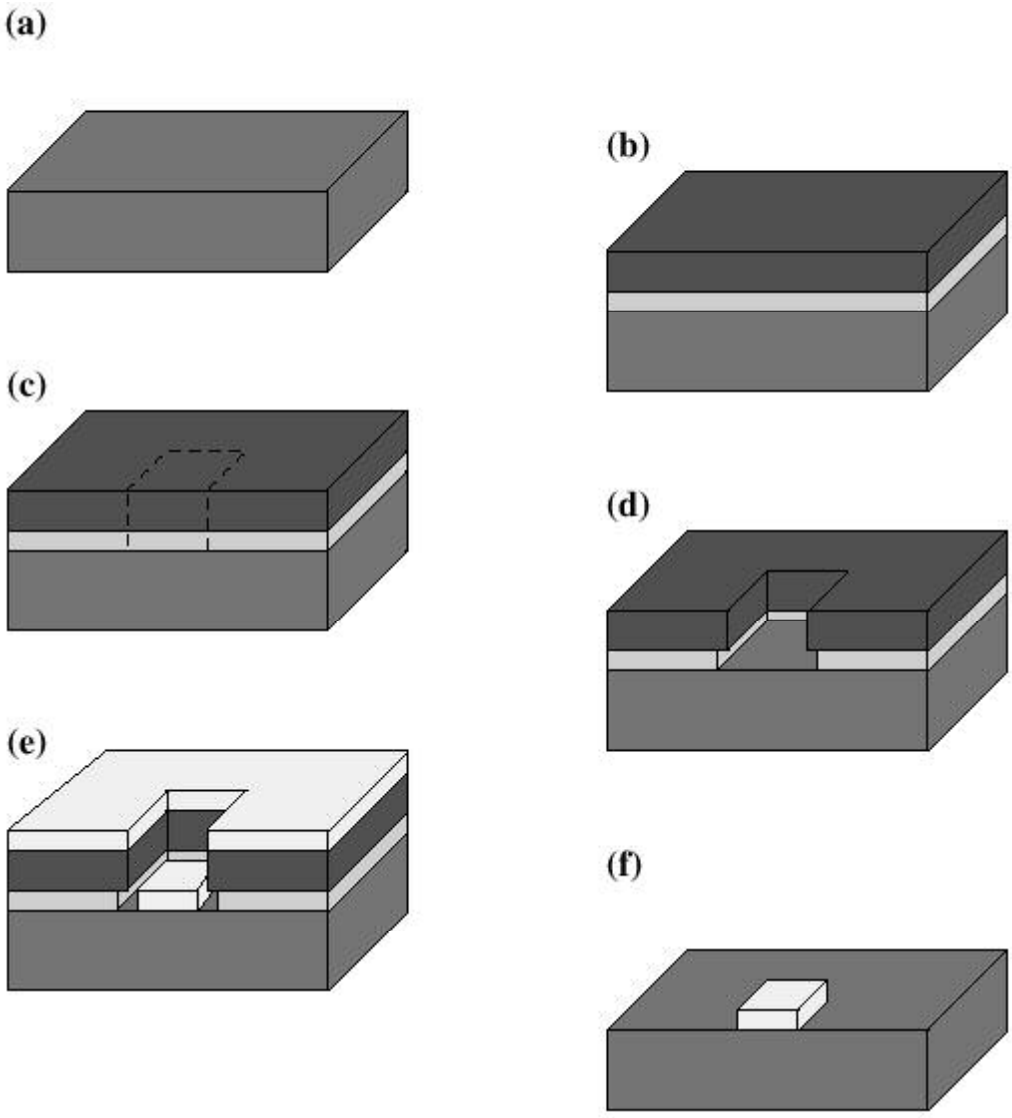

Figure 2-3. Scheme of lithography. (a) a clean chip. (b) two layers of resist on top of a clean chip. (c) part of resist exposed. (d) exposed resist is removed by a developer. (e) a thin film is deposited. (f) the film on the resist is removed by lift-off. The thin film where the resists was exposed is left. (courtesy Tobias Durkop)

In the find-and-wire scheme, the first lithography step is used to make alignment marker patterns usually after nanotube CVD growth. Cr/Au films are thermally evaporated to make alignment marker patterns because Au is easy to see under SEM. A Cr wetting layer is necessary for Au to stick on SiO_2. Typically Cr

and Au thicknesses are 1 and 30 nm, respectively, and the deposition conditions are not crucial in this step.

In nanotube device fabrication, locating nanotubes is the challenging (but fun) part owing to the random CVD nanotube growth. Figure 2-4(a) shows an alignment marker pattern. The zoomed-in picture shows a nanotube relative to the alignment markers. Many similar images have to be collected in order to get enough information to fabricate devices properly. In the Fuhrer lab, techniques were developed to take these kinds of images are with SEM rather than AFM [59], greatly speeding up the whole device fabrication process.

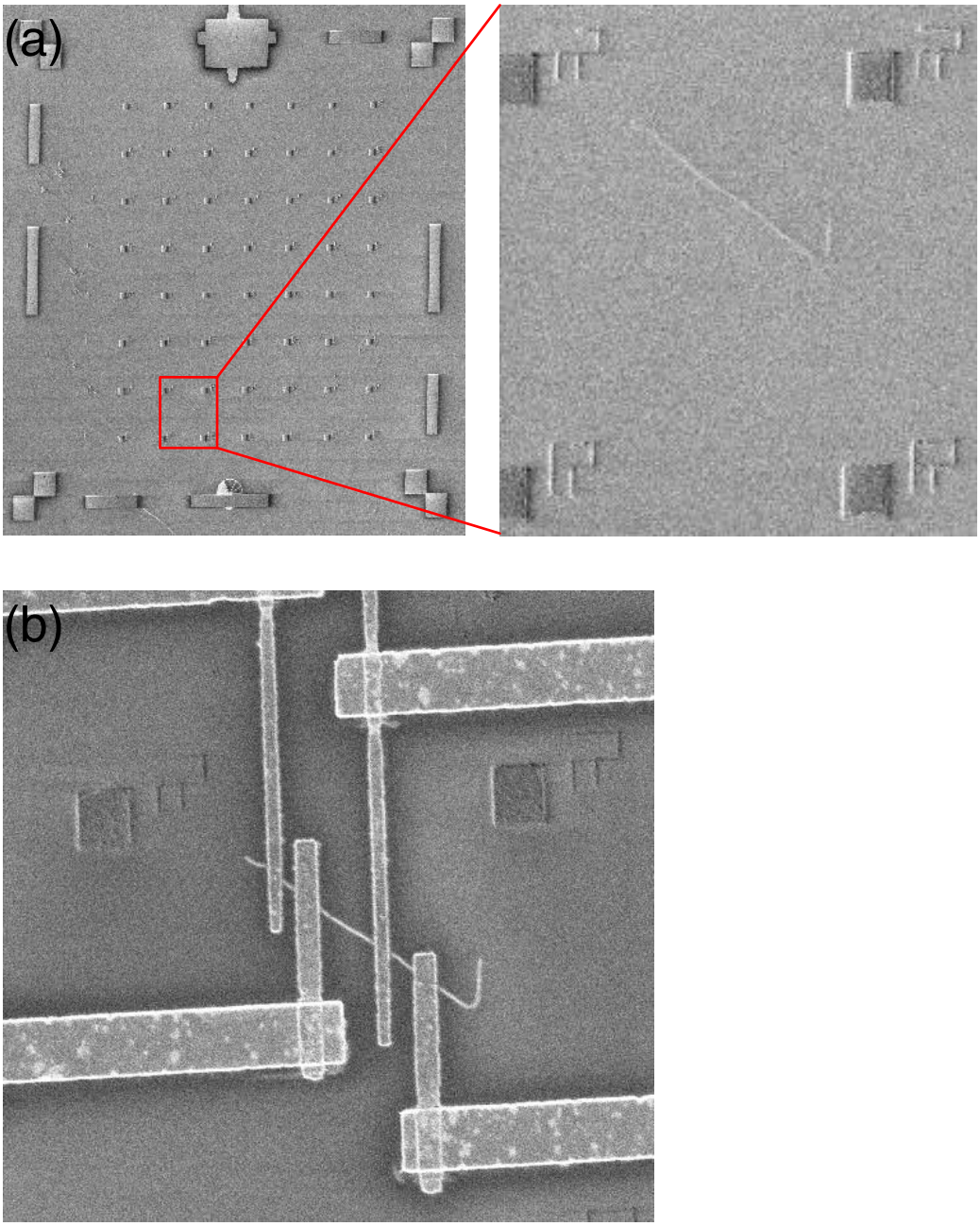

Figure 2-4. A nanotube selected to make a device. (a) an alignment marker pattern. The zoomed-in picture shows a nanotube relative to alignment markers. (b) a finished device with electrical contacts made of the same tube shown in the zoomed-in of (a).

The second lithography is needed for making electrical contacts to the selected nanotubes. Thermal evaporations for nanotube contacts are done with more

careful deposition conditions. The vacuum in the deposition chamber ranges from 3 $\times 10^{-6}$ to 4 $\times 10^{-7}$ torr to minimize the impurities in metals during evaporation. Figure 2-4(b) shows a finished device with the tube shown in the zoomed-in picture of Figure 2-4(a) contacted by four permalloy electrodes.

2.3 Annealing

Annealing has been found to often lower the contact resistance of nanotube devices [60]. It is not clear exactly how annealing results in better electrical contacts; likely possibilities are that impurities in the contact region are removed, the metal atoms in the contacts rearrange to form a better physical contact to the nanotubes, or that the gold diffuses through the wetting layer to make a better electrical contact to the nanotubes. The same oven system for nanotube growth (see Figure 2-1) is also used for annealing nanotube devices.

Table 2-2 shows a typical example of nanotube-metal contact annealing. The annealing parameters, such as gases, flow rates, flow times, and temperatures, are all adjustable to optimize the device performances.

Action	Gas	Flow (sccm)	Temp (°C)	Time (minute)
Purge	Ar	1500	RT	10
	H_2	1000		
Heat	Ar	1500	RT→400	4
	H_2	1000		
Soak	Ar	1500	400*	2
	H_2	1000		
Cool Down	Ar	1500	400→RT	4
	H_2	1000		

Table 2-2. A recipe of nanotube device annealing. (* indicate the temperature overshoot to 415 °C)

2.4 Electrical Measurement Setup

The major part of my research here is related to electrical measurements of nanotube devices. Figure 2-5 shows the device image, basic geometry and measurement setup. Figure 2-5(a) shows an SEM image of the nanotube device with the working parameters of the SEM. The CVD-grown nanotube is contacted by two Cr/Au electrodes. The ground, applied voltages V_g, V_d, and measured current I_d are labeled; V_g is applied to the conducting silicon substrate. The DC voltages applied to devices are sourced from a National Instruments BNC-2090 data acquisition device (DAQ), Keithley 2400 sourcemeter, Kepco BOP 100-1M power supply, or the auxiliary outputs of Stanford Research 830 Lock-in amplifier. The DC currents are translated into the voltage signals by Ithaco 1201 Current Preamplifier, and the voltages then are measured by National Instruments BNC-2090 DAQ or Agilent 34401A. The instruments are controlled by the computer programs written in

Labview or other comparable computer languages. The inset shows an AFM image of a section of the nanotube used to determine the diameter. Figure 2-5(b) depicts the side view of a nanotube device with device geometry.

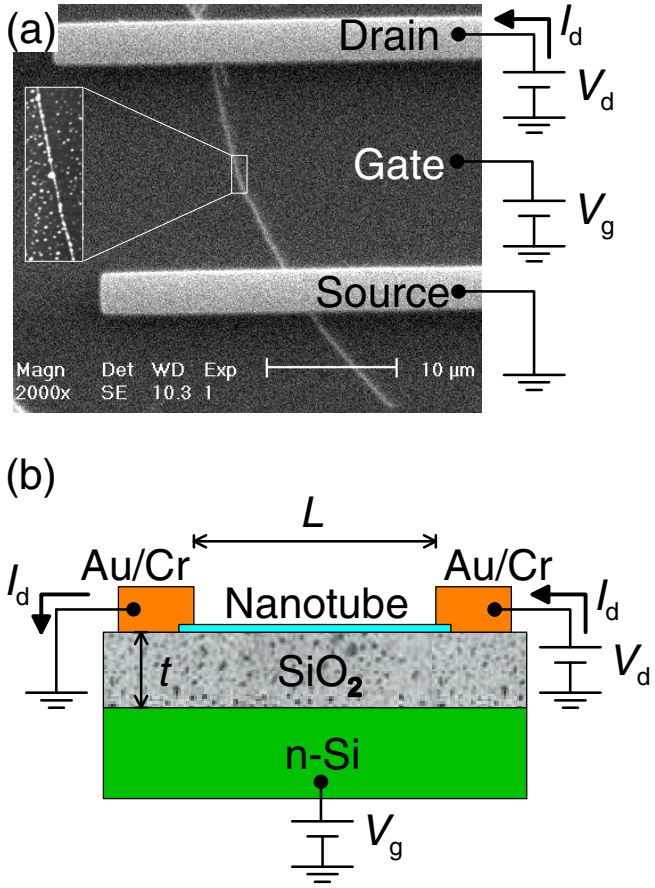

Figure 2-5. A nanotube device. (a) an SEM image of a nanotube device with basic electrical setup. The inset is an AFM image, which is usually used to determine a nanotube diameter *d*. (b) side view of a nanotube device with device geometry. *t* is the oxide thickness and *L* is the channel length.

Electrical measurements are performed at one of several setups which have been established in our laboratory; three of these are described below.

Cascade Probe Station (Cascade Microtech):

This probe station has a 1000X optical microscope, good to visualize devices and probe movement. The operational temperature range is 200 K ~ 500 K, and the environment may be controlled by constant gas flow. An air table is available to isolate mechanical vibration. The Cascade probe station is especially suitable for the study of large numbers of devices; many devices with identical device geometry can be measured automatically because the stage position (and also the position of one probe) is controlled by computer.

Cryo-Probe Station (Desert Cryogenics):

This probe station also has a 1000X optical microscope. The operational temperature range is 1.5 K ~ 475 K, good for short-term low temperature measurements. The chamber can be pumped to 10^{-6} torr at room temperature and different gas environments can be established. An air table is available as well.

Cryostat (Desert Cryogenics):

Temperature operational ranges are 1.2 K ~ 325 K in ^{4}He gas environment for ^{4}He probe and 300 mK to 325 K in vacuum for ^{3}He probe. The superconducting coil is able to produce magnetic field range from -9 to 9 Tesla.

Chapter 3

Scanning Probe Microscopy to Characterize Nanotube Devices

3.1 Introduction to Scanning Probe Microscopy

People use light to see the world around them. Optical microscopes were the first instruments to aid people in seeing small objects. However, because of diffraction of light, the sizes of the objects which can be imaged by optical microscopy are limited by the wavelength of visible light, which is on the order of 100 nm. Electron beams, whose wavelengths are much short than the wavelength of visible light, are used in electron microscopes, e.g. scanning electron microscopes and transmission electron microscopes.

People can also touch objects in the world around them. Instead of using our fingers, microfabricated cantilevers with sharp tips at the end can be used to touch small objects, and thus form an "image" of them. Scanning probe microscopy (SPM) includes a large group of microscopes which utilize this idea to image physical properties of materials, especially surface properties. The principles of SPM are founded on the invention of scanning tunneling microscopy (STM). STM was invented and demonstrated by Gerd Binnig and Heinrich Rohrer at IBM in Zurich [61], who therefore were awarded by Nobel Prize in 1986. The core of the SPM includes three parts: scanner (in xyz directions), probe (a sharp tip or a cantilever with a sharp tip), and feedback electronics (to maintain the constant interaction between tip

and surface). Atomic resolution imaging was achieved [62] by these simple pieces of equipment. Figure 3-1 shows the schematic diagram of STM.

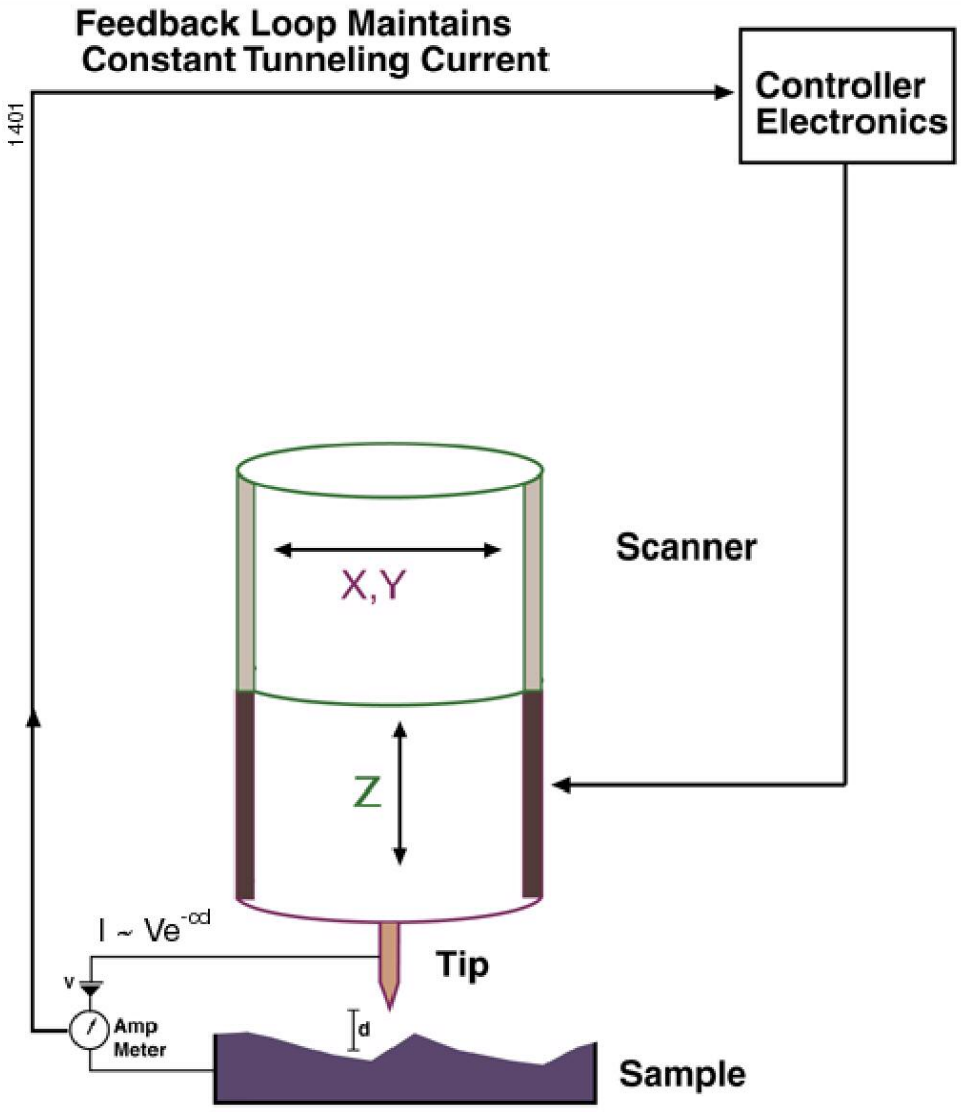

Figure 3-1. Schematic diagram of STM. (courtesy Digital Instruments)

However, the applicability of STM is greatly limited by the need of conducting samples since tunneling current between the tip and the sample is used as a feedback signal; non-conducting samples are not accessible by STM. Another

feedback scheme is then needed in order to access non-conducting samples. Gerd Binnig and his colleagues again invented another SPM technique called atomic force microscopy (AFM) which uses the force between tip and sample as a feedback signal [63]. AFM is more sample-friendly and therefore used more widely in many areas of research. Atomic resolution in a clean and flat surface can also be attained with AFM [64]. AFM is a landmark of nanotechnology; without the help of SPM, nanotechnology likely could not have developed so fast. For general reviews of AFM, please read Ref. [65,66].

Nanotubes and nanotube devices are characterized by SPM by many researchers. STM is used to determined the atomic structures (chiralities and indexes (n,m)) of SWNTs from atomic resolution images and electronic properties from scanning tunneling spectroscopy [8,13-15]. AFM is used to measure diameters of nanotubes. Conducting tip AFM has been used to as one of the contact electrodes to measure nanotube electronic transport [67-70]; as a local gate to deplete carriers [71], study barriers in nanotube-metal contacts [72] or nanotube-nanotube junctions [71], and probe defects of nanotubes [73,74]; or in electrostatic force microscopy (EFM) to measure the conductance of nanotubes [75] and local electronic structure [76].

In our lab, there are two SPM setups: JEOL 4210 and DI Dimension 5000. Both of them have varieties of features. JEOL 4210 has vacuum capability (2.6×10^{-7} torr at room temperature) and temperature tunability from 130 K to room temperature by using the cooling stage and from room temperature to 773 K by using the heating stage (both stages have to be operated under vacuum conditions). DI Dimension 5000 has a very wide sample stage which allows large wafer scanning or

extra setups (for example probes for electrical measurements) on it. I have used the JEOL 4210 to do SPM characterize on nanotube devices because I need the features it offers.

In this chapter, I will focus mainly on two specific SPM techniques, EFM and scanned gate microscopy (SGM), to probe the electronic properties of nanotubes. My work was initiated by the previous work done by Prof. Adrian Bachtold and my advisor Prof. Michael Fuhrer in Berkeley [42]. At the end I will introduce one more commonly used SPM technique, Magnetic Force Microscopy (MFM). In Chapter 5 I will mention using MFM to characterize the magnetization of ferromagnetic contacts of nanotube spin-valve devices.

To be able to access the devices electrically while doing SPM scanning, an extra wiring setup is needed. Figure 3-2 shows the SPM system I used, JEOL-4210, combined with the setup of electrical connection to devices on a surface.

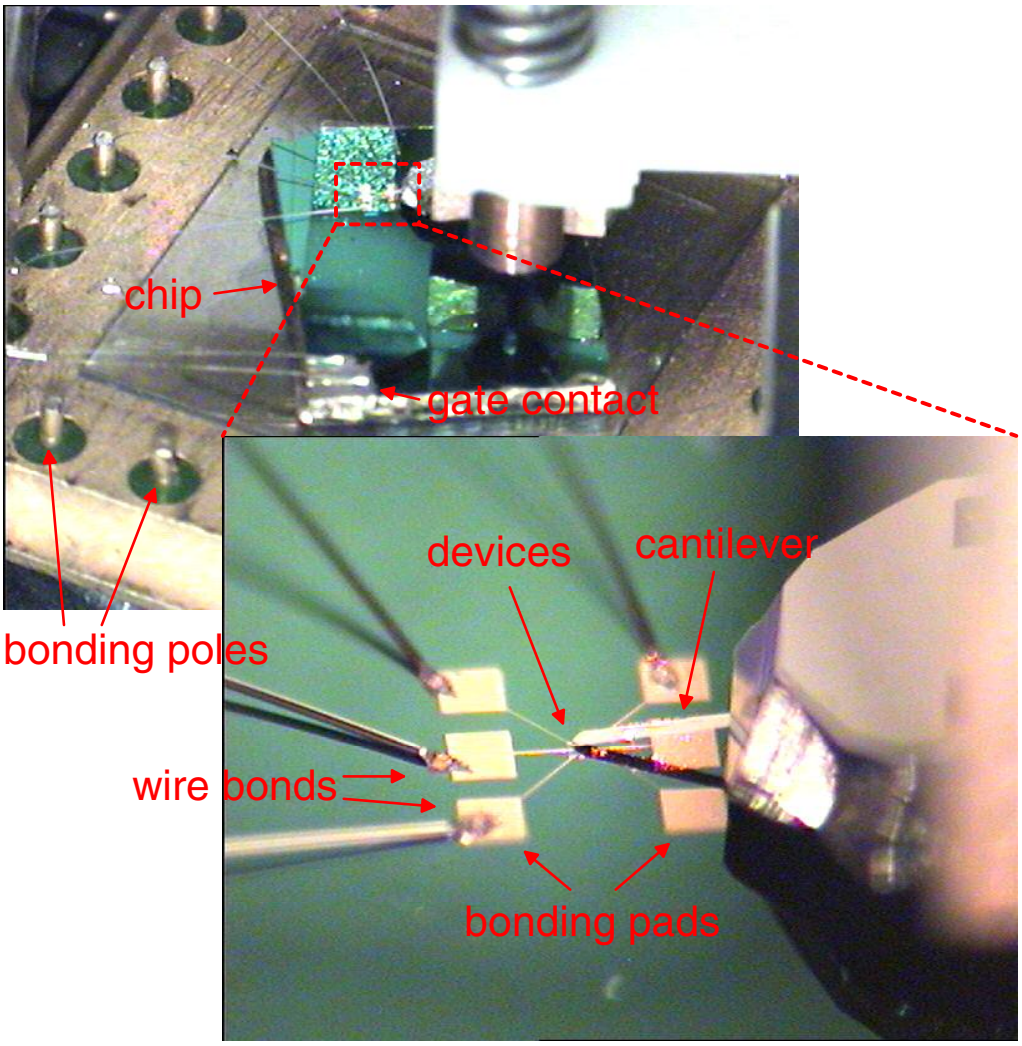

Figure 3-2. SPM with electrical measurement setup.

3.2 Electrostatic Force Microscopy

In nanotube devices, we are not able to do four-probe measurements to determine the intrinsic resistivity of nanotubes due to strongly invasive nature of the electrical contacts in one-dimensional systems; in order to measure voltage with an electrical contact, scattering into the contact is necessary to achieve electrochemical potential equilibrium, but such scattering adds significantly to the measured resistance. However, researchers are interested in the resistance distribution within a

nanotube device; to determine e.g. whether the contact resistance or the channel resistance dominates the device resistance. One way to measure the resistance distribution is to map the potential profile along the device while applying a voltage across to the device. EFM is a good candidate for this purpose [42]. EFM is a SPM technique utilizing the electrostatic force between the scanning tip and the samples to measure the capacitances between the tip and the surface, charge distribution, and the surface potentials [77-79].

The easiest EFM implementation is DC-EFM, so-called because the voltage between tip and sample does not oscillate. The electrostatic force between the tip and some local position of the sample F is

$$F = -\frac{\partial U}{\partial z} \approx -\frac{\partial}{\partial z}\left(\frac{1}{2}C(V_{\text{tip}} - V_{\text{local}}(x,y) + \phi)^2\right) = -\frac{1}{2}\frac{\partial C}{\partial z}(V_{\text{tip}} - V_{\text{local}}(x,y) + \phi)^2,$$

Equation 3-1

where U and C are the electrostatic energy and the capacitance between the tip and the local position of the sample, respectively; V_{tip} and $V_{\text{local}}(x,y)$ are the potential of the tip and the local position of the sample, respectively; ϕ the work function difference between the tip and the local position of the sample. The force constant change Δk due to the electrostatic force is

$$\Delta k \approx -\frac{\partial F}{\partial z} = \frac{1}{2}\frac{\partial^2 C}{\partial z^2}(V_{\text{tip}} - V_{\text{local}}(x,y) + \phi)^2. \qquad \text{Equation 3-2}$$

The force constant change of the cantilever causes a shift of the natural frequency $\Delta\omega_0$, therefore, a phase shift of the amplitude of the tip cantilever

$$\Delta\varphi \propto \Delta\omega_0 \propto \Delta k \propto (V_{\text{tip}} - V_{\text{local}}(x,y) + \phi)^2, \qquad \text{Equation 3-3}$$

where the potential constant equals Q/k. Q and k are the quality factor and the force constant of the cantilever, respectively. The DC-EFM signal is the phase shift $\Delta\varphi$, which is sensitive to the surface potential. However, the DC-EFM phase shift signal is quadratic in the surface potential [42]. Thus it is hard to map the signal to the potential in data manipulation.

AC-EFM avoids this difficulty: as will be shown below, the signal of AC-EFM is linearly proportional to the surface potential, which helps to get quantitative information about the surface potential and reduces many difficulties in processing and understanding the data.

I will describe below a slightly modified version of AC-EFM compared to Ref. [42] which was necessitated by the lack of "lift mode" in the JEOL-4210 microscope. Lift mode (patented by the company Digital Instruments) is a technique in which the tip is scanned at a fixed height above the sample during the detection of electrostatic or magnetic forces in e.g. EFM or MFM. In my setup, the electrostatic force is detected at one frequency, simultaneous to the topographic scan which requires feedback at the tip oscillation frequency. My modified AC-EFM setup is sketched in Figure 3-3.

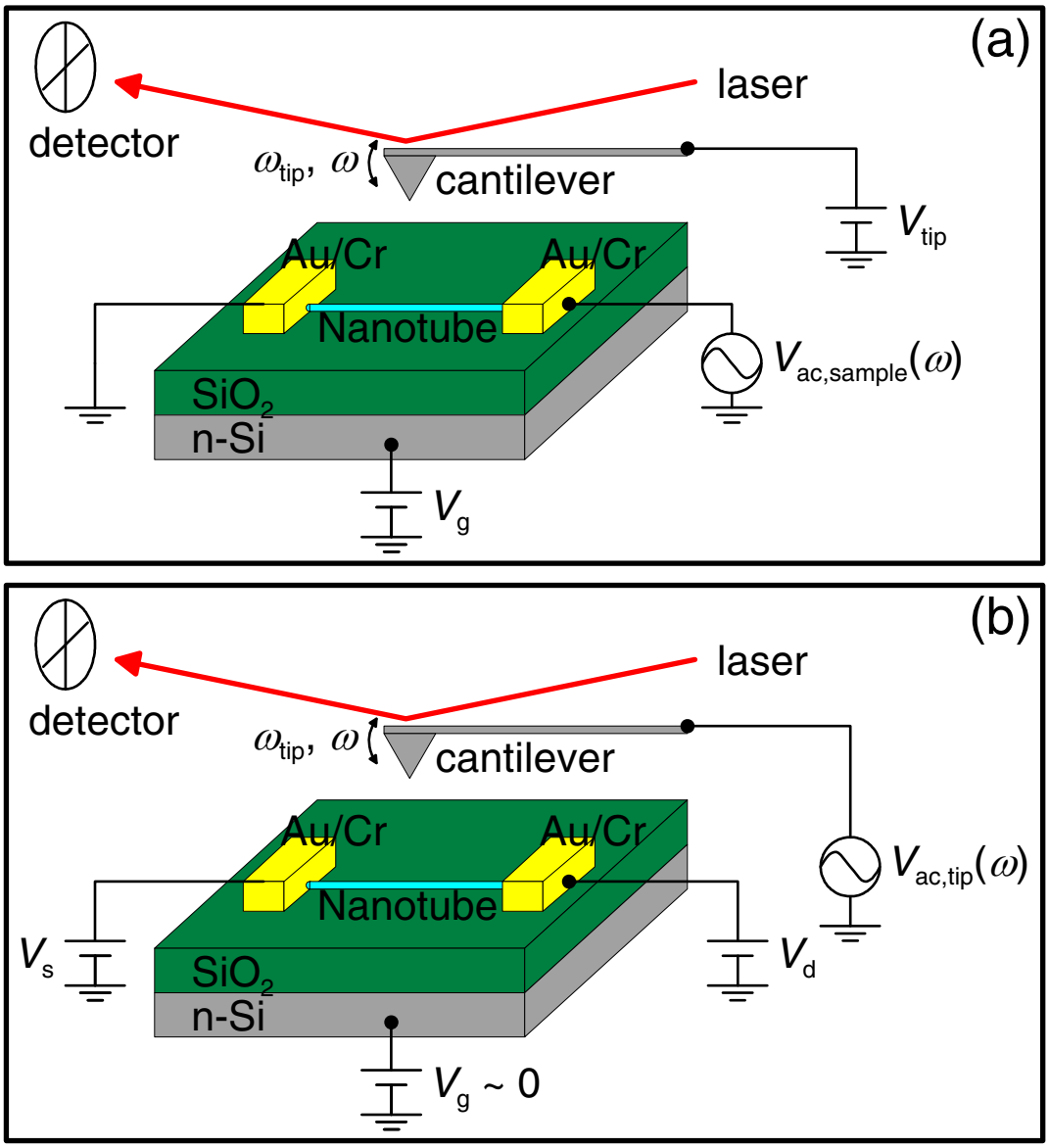

Figure 3-3. Schemes of AC-EFM. (a) AC-device-EFM. (b) AC-tip-EFM.

Like the usual "tapping mode" AFM, the tip is driven by the piezoelectric at frequency ω_{tip}, which is very close the tip natural resonant frequency. The electronic feedback system controls the amplitude of tip, which determines the tip-sample distance. By doing tapping mode AFM, a topography image can be taken. While doing tapping mode AFM scanning, another AC bias with frequency ω (which is usually chosen to be close to tip natural resonant frequency, too) is then applied either

to the device (see Figure 3-3(a)) or the tip (see Figure 3-3(b)). Due to the electrostatic interaction between the tip and the sample, the tip also oscillates at frequency ω. The amplitude and the phase of the tip oscillation at frequency ω are detected by the photo detector, and recorded with respect to x-y positions to form EFM images.

To quantitatively extract the surface potential, the following analysis is needed. The electrostatic interaction between the tip and the sample is depicted in Figure 3-4. The electrostatic force between the tip and some local position of the sample F is also expressed by Equation 3-1.

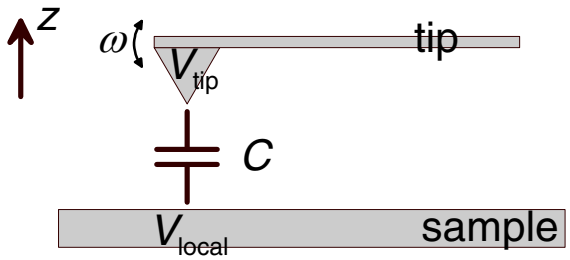

Figure 3-4. Electrostatic force interaction between tip and sample.

For AC-device-EFM, an AC signal with frequency ω is applied to the device. The local surface potential at certain position (x,y) has AC component $V_{\text{local}}(\omega,x,y)$. The amplitude signal $A(\omega,x,y)$ is proportional to the AC force component $F_{\text{ac}}(\omega)$. Therefore,

$$A(\omega, x, y) \propto F_{\text{ac}}(\omega) = -\frac{\partial U}{\partial z}(\omega) \approx \frac{\partial C}{\partial z} \cdot (V_{\text{tip}} + \phi) \cdot V_{\text{local}}(\omega, x, y), \qquad \text{Equation 3-4}$$

which shows a linear relationship between $A(\omega,x,y)$ and $V_{\text{local}}(\omega,x,y)$.

For AC-tip-EFM, the AC signal $V_{\text{tip}}(\omega)$ is applied to the tip. Therefore,

$$A(\omega, x, y) \propto F_{ac}(\omega) = -\frac{\partial U}{\partial z}(\omega) \approx \frac{\partial C}{\partial z} \cdot (V_{local}(x, y) - \phi) \cdot V_{tip}(\omega), \quad \text{Equation 3-5}$$

which also shows a linear relationship between $A(\omega,x,y)$ and $V_{local}(x,y)$.

AC-device-EFM and AC-sample-EFM have different advantages. The major advantage of AC-device-EFM is that the image shows strong signal at the positions electrical connected to the device and zero signals at all other place. The major advantage of AC-tip-EFM is that various DC device bias (V_d and V_s) dependent studies can be done, especially good for high DC device bias studies.

Figure 3-5 shows a broken nanotube device. Both AFM image in (a) and EFM image in (b) are taken simultaneously. The technique for this EFM image is AC-device-EFM. The top electrode is AC biased, while the bottom one is grounded. In the AFM topography image, the break of the tube can not be seen, although the transport data show that the device is not conducting; probably indicating the break is atomic in scale. In EFM image, a clear contrast is seen. The reason for that is due to the open circuit; the potentials of the top and the bottom parts of the nanotube are the same as top electrode ($V_d = V_{ac,sample}$) and the bottom ($V_s = 0$), respectively. One important point: although the two images are taken simultaneously, there is no correlation between them. The topography information is not observed in EFM images.

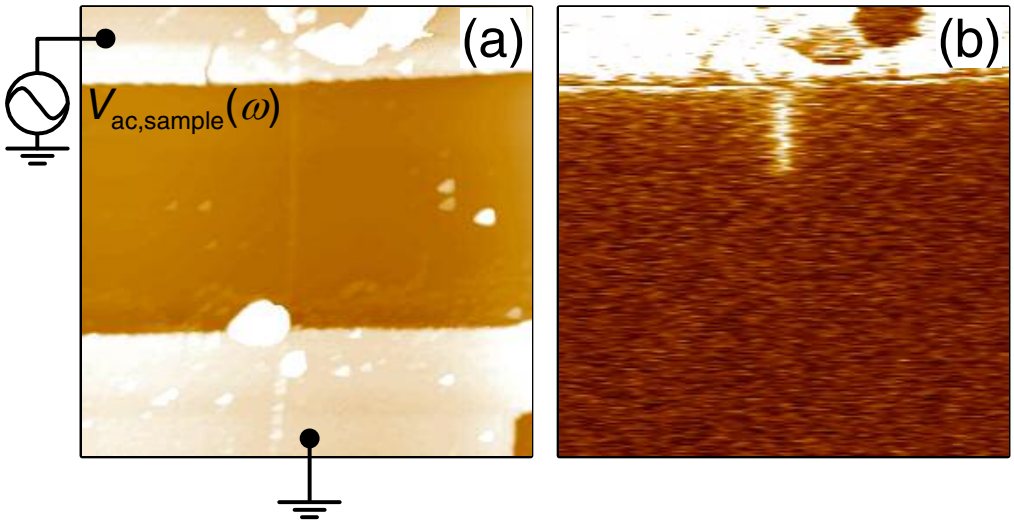

Figure 3-5. A broken nanotube device. (a) AFM image. (b) EFM image. The break is not visible under AFM, but shows up clearly under EFM. The scan size is 5.4 × 5.4 μm^2. The two pictures are taken simultaneously.

Figure 3-6(a) shows another EFM image. There are two electrodes on the top and bottom of the image (see Figure A-1(a) in Appendix A for AFM image of the device). The top and bottom electrodes are DC biased, separately (V_d = 0 and V_s = -1 V). The technique for this EFM image is AC-tip-EFM. There are EFM signal gradients from the top to the bottom both along the nanotube and on the bare SiO_2 substrate mainly due to the long-range capacitive coupling of the tip to the electrodes. After the signal background subtraction, the potentials at each point of the nanotube are able to be extracted (the detailed data processing is in Appendix A). Figure 3-6(b) shows the derived potential along the nanotube. The potential drops along the nanotube as expected. From the derived potential, we can say that at this specific bias condition, the major resistance of the device is distributed in the nanotube itself although the potential extraction near the contacts is more difficult and uncertain (see the discussion in Appendix A).

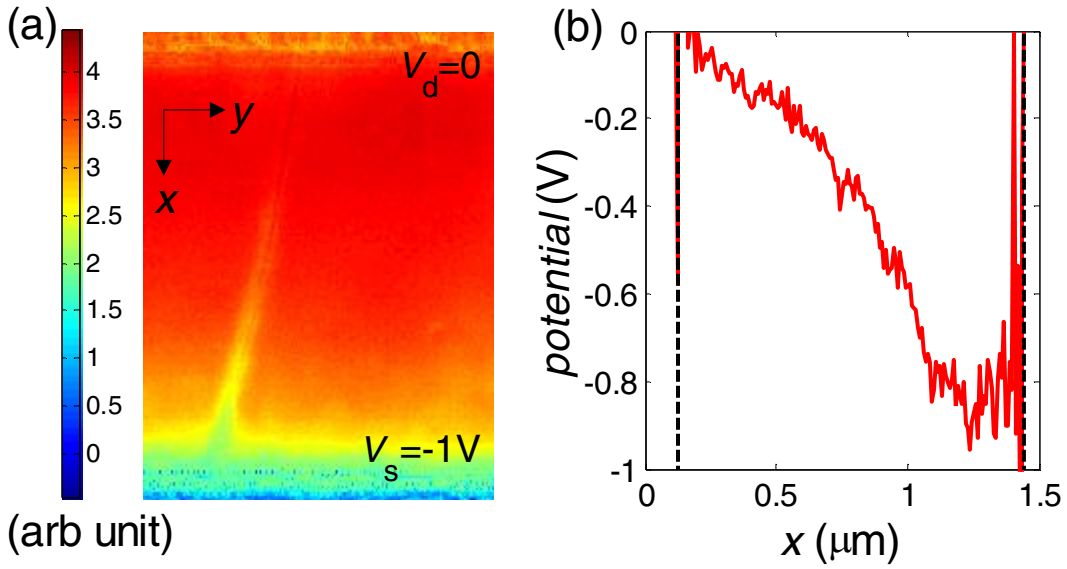

Figure 3-6. EFM data. (a) An EFM image of nanotube device. The top electrode is grounded (V_d = 0), while the bottom electrode is biased with -1 V (V_s = -1 V). The gate bias V_g equals 0.4 V. The amplitude and frequency of AC tip bias $V_{ac,tip}(\omega)$ equals 0.2 V and 13 kHz, respectively. The scan size is 1.5 × 1.5 μm^2. (b) The potential profile along the nanotube extracted from (a). The black dashed lines indicate the edges of the electrodes. The processes of extracting nanotube potential profiles from EFM images is discussed in Appendix A.

3.3 Scanned Gate Microscopy

SGM is a SPM technique which treats an AFM conducting tip as a local gate to modulate the local charges or potentials of devices and monitor the conductances (or resistances) of devices [80,81]. By scanning a device, the regions which are sensitive the local field changes display very clearly in SGM images. SGM has been used to study 0D point contacts [80,82,83], quasi-1D electron gases [81], and 2D electron gases [84]. SGM has also been used to investigate defects and/or contacts on carbon nanotube devices [42,50,72-74,85-87].

The SGM techniques I have used consist of AC-SGM and DC-SGM. Figure 3-7 shows both SGM schemes over a nanotube device. While doing tapping mode AFM scanning, the conducting AFM cantilever also acts like a local gate over devices which are electrically biased. The major difference between AC-SGM and DC-SGM is that AC-SGM measures the AC current of the device responding to the vibration of the tip with respect to the local gate position over the device while DC-SGM measures the DC current.

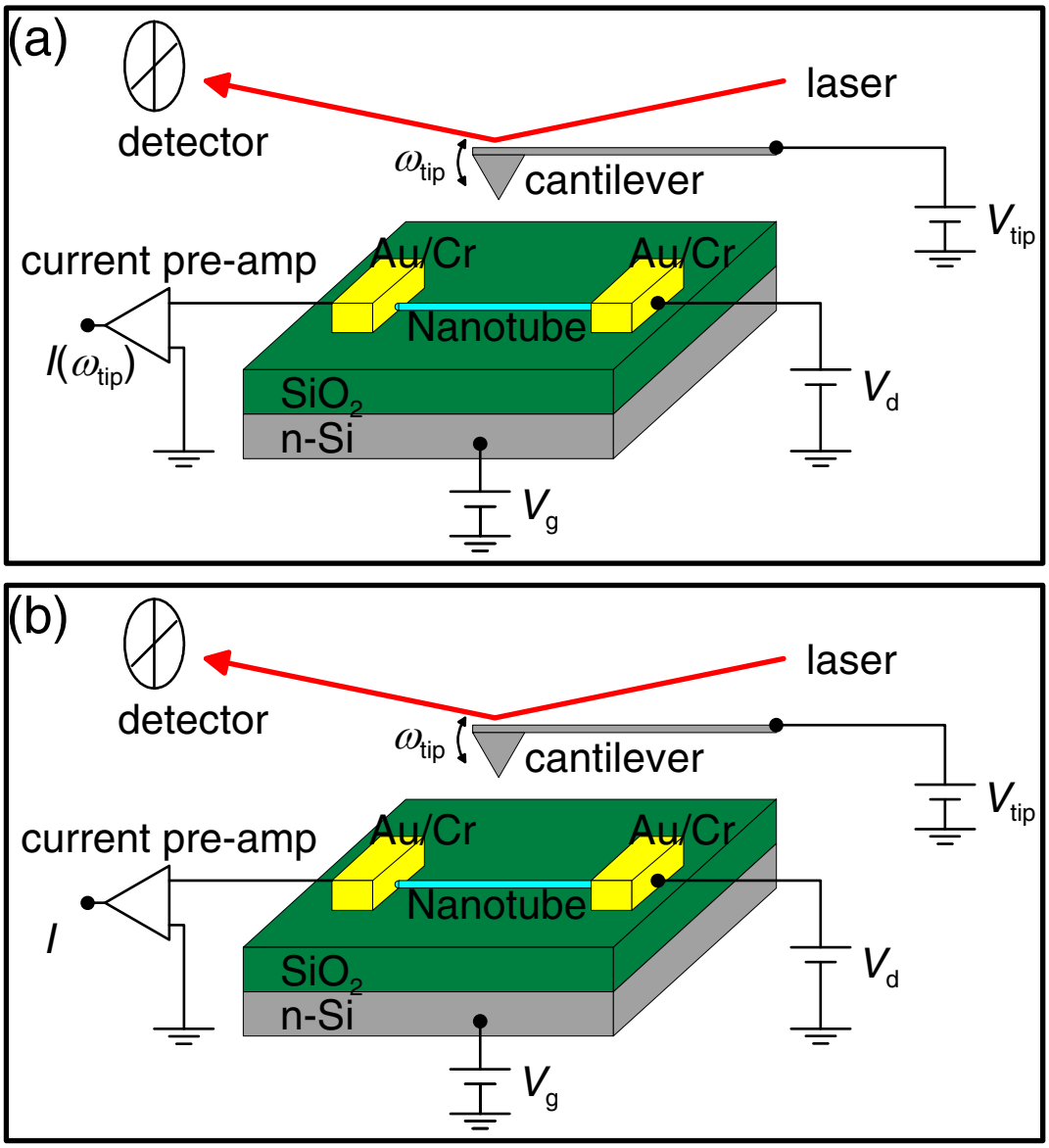

Figure 3-7. Schemes of SGM. (a) AC-SGM. (b) DC-SGM.

Figure 3-8 shows the AFM and SGM images of a nanotube device with two contacts. Figure 3-8(a) is an AC-SGM image, and Figure 3-8(b) is an AFM image taken simultaneously with Figure 3-8(a). The first thing to notice is that the SGM image does not show the information of device topography. The only thing matter in the SGM image is whether the device charge transport reacts to the tip gate. In Figure 3-8(a), two nanotube positions near the contacts are very sensitive to the tip

gate. The contacts play a very important role in such bias conditions. Figure 3-8(c) shows AC-SGM image of the same device at different bias condition. In Figure 3-8(c), many positions along the nanotube are sensitive to the tip gate, even one section of nanotube reacts to the tip gate oppositely (the bright spot). The device behaves very differently at two bias conditions according to SGM images, which can not be known in transport measurement only. Figure 3-8(d) shows a DC-SGM image of the same device. Unlike the unit of the signal in AC-SGM is arbitrary, the color scale in DC-SGM is the magnitude of the device DC current. At this particular bias condition, the tip enhances the device current while it is close to nanotube-metal contacts. From the image, we know the tip actually reducing the thickness of Schottky barriers of the contacts, which will be discussed more in Chapter 8.

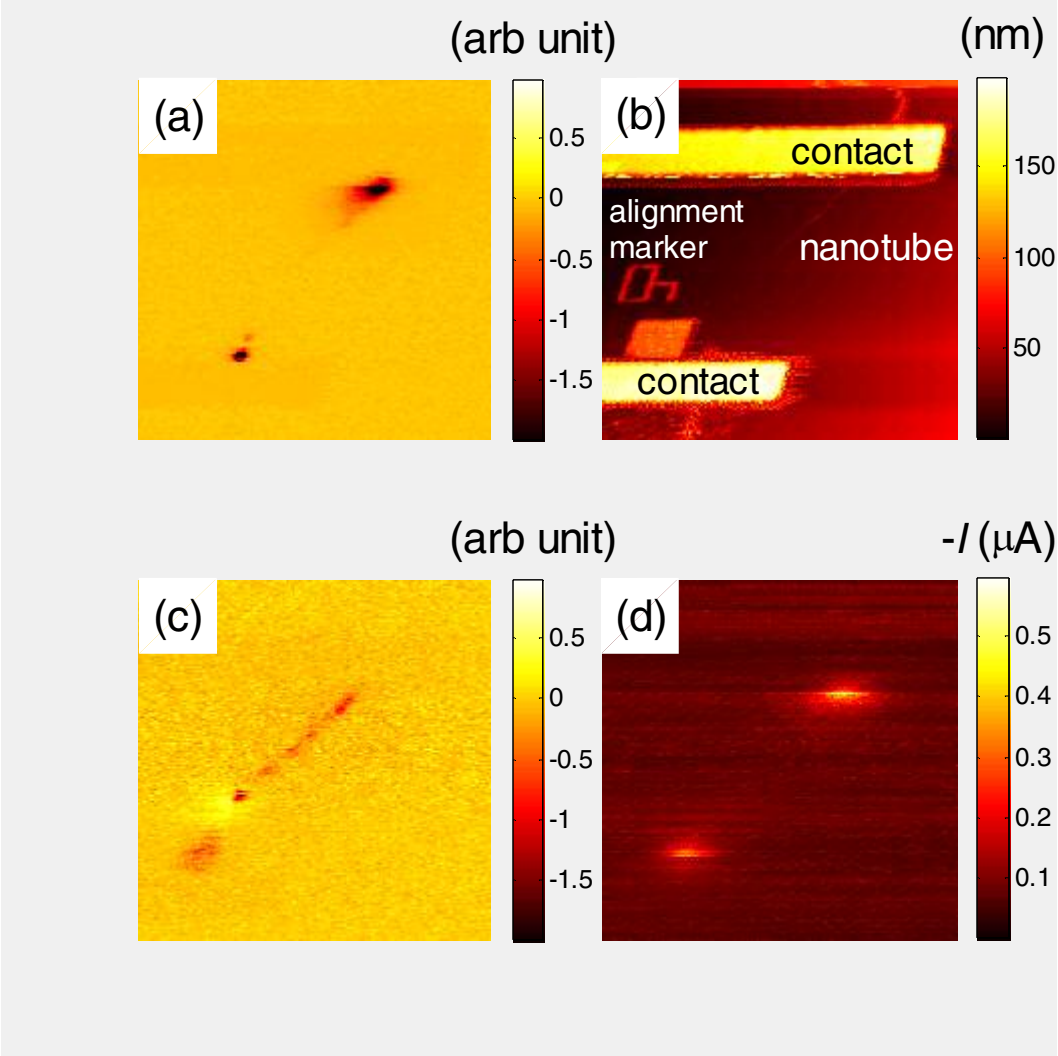

Figure 3-8. SGM and AFM images. The scan sizes for all images are 6 × 6 μm^2. (a) AC-SGM image. The top electrode is biased with -6 V (V_d = -6 V), while the bottom electrode is grounded (V_s = 0). The gate bias V_g and the tip bias V_{tip} are all equal to -2 V. (b) AFM image taken simultaneously with (a). (c) AC-SGM image taken at V_d = 0, V_s = -4 V and V_g = V_{tip} = -2 V. (d) DC-SGM image taken at V_d = -8 V, V_s = 0, V_g = -4.2 V, and V_{tip} = -4 V.

Either AC-SGM or DC-SGM technique has its own advantages. AC-SGM has more spatial sensitivity, which provides more localized information on a small-scale device. DC-SGM images are easier to interpret in view of the fact that the signal is the DC current through the device.

In chapter 8, I will describe how DC-SGM and AC-tip-EFM are further used to characterize nanotube devices under high DC biases.

3.4 Magnetic Force Microscopy

Magnetic Force Microscopy (MFM) is a SPM technique which detects the magnetic field distribution of a surface by an MFM tip, an AFM tip coated by a magnetic material. Similar to DC-EFM described above, the magnetic force between the tip and some local position of the sample causes a phase shift of the amplitude of the tip cantilever, which is the signal of MFM. MFM is frequently used to detect magnetic moments on the surface of a magnet since the magnetic moment produces a strong magnetic field locally.

Chapter 4

Single Electron Memory

4.1 Single Defect Detection Using Scanned Gate Microscopy

Low power nonvolatile memory has been the subject of much research. The lowest power consumption electronic memory conceivable would have a node which stores a single electron [88-90]; such a device is a called a single electron memory. There are many candidates for the readout elements in a single electron memory; a NTFET is one of them. NTFETs have advantages in that they are relatively easy to fabricate (a single processing step defines source, drain, and channel), they have high carrier mobility [28], and they are intrinsically nanoscale. The last two are necessary in order that small changes in charge produce large conductivity changes. Recently our group succeeded to make single electron memories using NTFETs [29,50]. These memory devices took advantage of the many charge traps intrinsic to the SiO_2 substrate, which were used as electron storage nodes. However, in a nanotube single electron memory the nanotube should only be sensitive to one single storage node. We then assumed that only one small piece of the nanotube is the readout and responsible for the single electron memory effect. SGM is then an ideal tool to test this assumption and identify the responsible piece of the nanotube.

Figure 4-1 shows I_d as a function of V_g of a p-type NTFET. V_g is swept back and forth many times. Several discrete states are shown due to I_d vs. V_g is multi-valued. The most possible explanation for the device showing these discrete states is the charge storage node close to the nanotube readout contains few electrons; each

state corresponds to an electron storage configuration and the adjacent states are with one electron difference. The hysteresis loops are also shown between states. Any hysteresis loop is then available for a single electron memory.

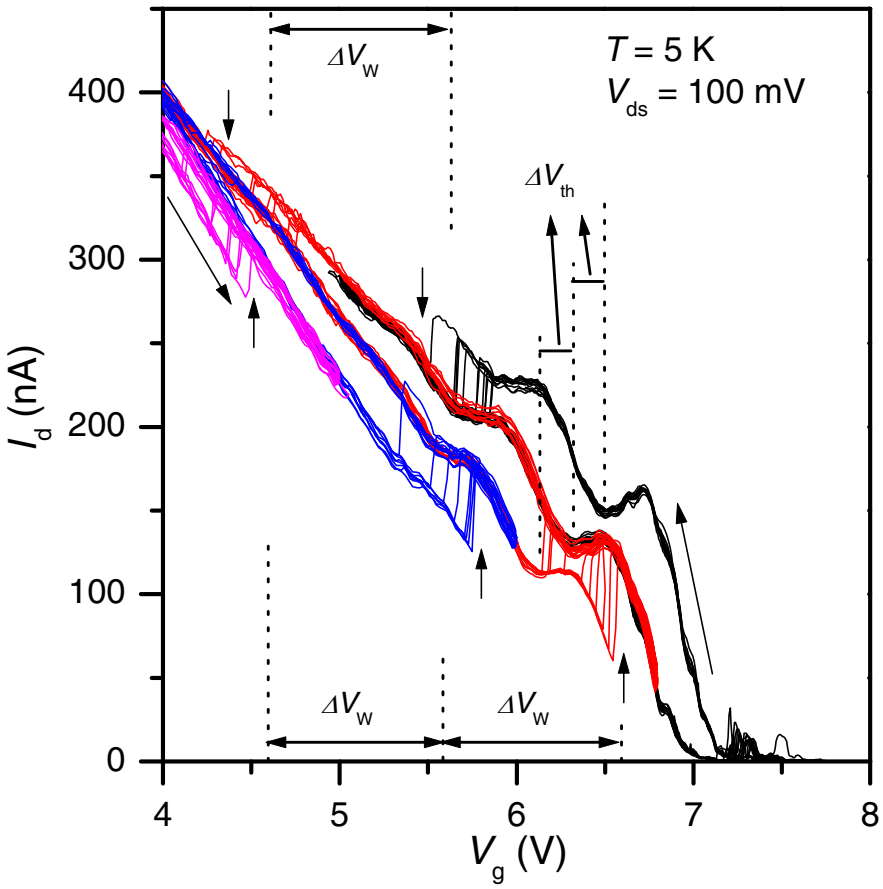

Figure 4-1. Drain current I_d as a function of gate voltage V_g for the nanotube single electron memory device at a temperature of 5 K. Five discrete curves are seen, with no intermediate values of I_d. Hysteresis loops are evident in the figure. Several sweeps back and forth over Vg ranges are shown. Arrows indicate sweep directions and switches. ΔV_{th} indicates the shift in V_g between the I_d-V_g curves; ΔV_{th} = 0.2 V. ΔV_w indicates the shift in V_g between the jumps between I_d-V_g curves; ΔV_w = 1 V.

Figure 4-2 show an AC-SGM image in (b) and its corresponding AFM-topography image of the device in (a), whose transport data are shown in Figure 4-1. The contrast in AC-SGM image indicates that the change of the device resistance responds to the conducting tip. Bright means large resistance change. The SGM signal along the nanotube is stronger which is consistent to that the nanotube is semiconducting; every piece of the nanotube reacts to the tip. One spot is particularly bright, but is not visible in corresponding AFM-topography image. We guess that this may be a single atomic-scale defect in the nanotube. The line trace alone the nanotube in Figure 4-2(c) shows the width of the peak is ~ 30 nm, which is not indicative of the actual size of the defect and probably limited by the size of the tip. However, here we still demonstrate the ability of SGM to detect a piece of nanotube, which is sensitive to local potential variance, in a nanotube device.

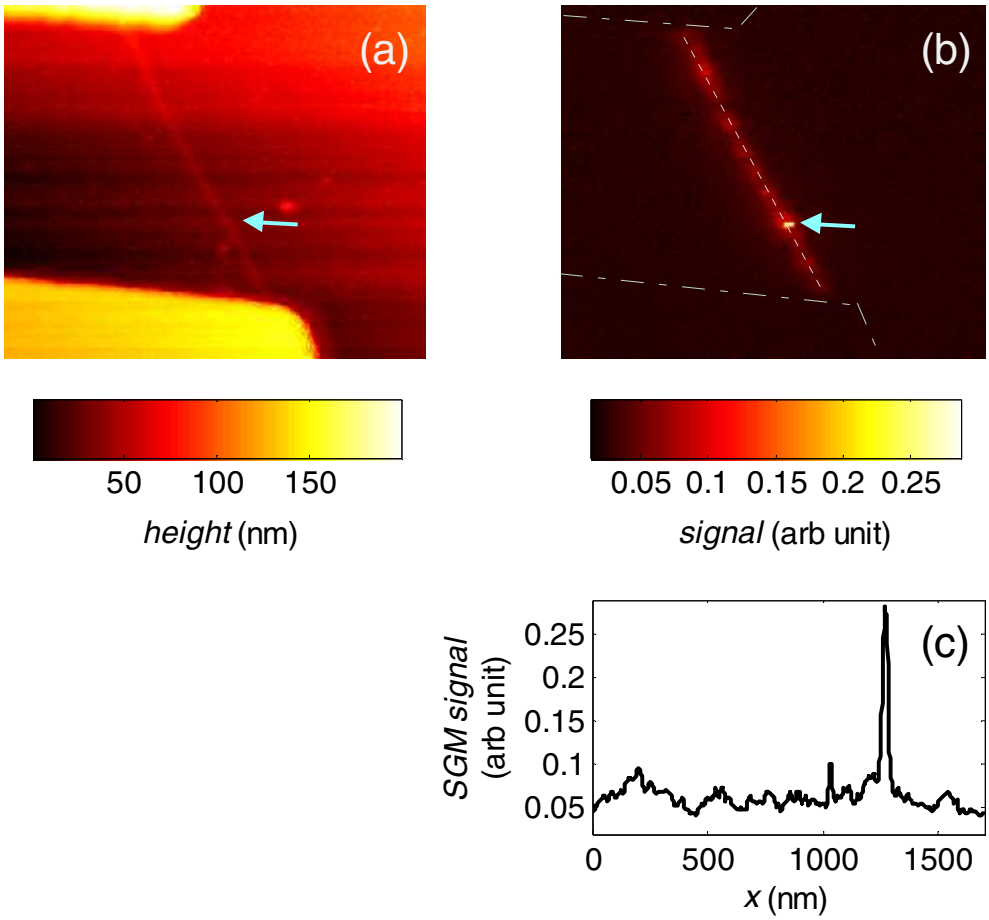

Figure 4-2. SPM images of a nanotube single electron memory. (a) AFM image and (b) AC-SGM image are taken simultaneously. The scan size is 2.26 × 2.26 μm^2. The bias settings are V_d = 100 mV, V_g = 0, and V_{tip} = 4 V. The arrows point to a possible atomic defect in the nanotube. The dotted line in (b) indicates the nanotube position, and the dash-dotted lines indicate the edges of the electrodes. (c) shows the line trace of the dotted line in (b) along the nanotube.

4.2 Capacitance Analysis of a Single Electron Memory

Figure 4-3 shows a probable schematic of our device described above. The charge trap (either at the SiO_2 surface or in the SiO_2 bulk) is coupled capacitively to the defect in the nanotube channel through a capacitance C_{TC}, and to the gate through a capacitance C_{GT}. There is also in additional capacitance between the gate and

channel, C_{FC}. In addition, a non-linear resistor R_{TC} must be present between the nanotube channel and the charge trap to allow charging and discharging of the defect. Such a device structure has been considered in detail in Ref. [91], where it was shown that this structure forms the basis of a single electron memory. The I_d-V_g characteristics of a transistor coupled to a charge trap in this way will show discrete curves, separated in gate voltage by an amount

$$\Delta V_{th} = \frac{eC_{TC}}{(C_{TC} + C_{GT})C_{GC}}, \qquad \text{Equation 4-1}$$

where e is the electronic charge and C_{GC} is the total gate capacitance given by

$$C_{GC} = C_{FC} + \frac{C_{TC}C_{GT}}{C_{TC} + C_{GT}}. \qquad \text{Equation 4-2}$$

Periodic switching events will occur between curves with a spacing

$$\Delta V_W = \frac{e}{C_{GT}} \qquad \text{Equation 4-3}$$

and the hysteresis width (the distance in gate voltage between the switching events between two charge states of the trap when increasing gate voltage and decreasing gate voltage) is determined by the nonlinear characteristics of the resistor R_{TC} between channel and charge trap [91].

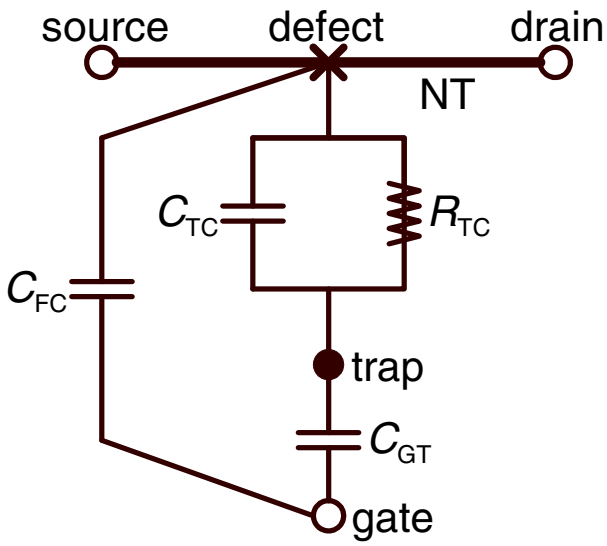

Figure 4-3. Schematic of a single electron memory device. Source and drain denote the contacts to the nanotube channel, the defect is the spot of high gate-voltage dependence on the nanotube observed in the scanned gate microscopy image in Figure 4-2(a), the gate is the conducting silicon substrate, and the trap is a charge trap located presumably at the surface or in the bulk of the SiO_2 dielectric.

For our device, we observe a threshold shift $\Delta V_{th} = 0.2$ V, and a write voltage periodicity $\Delta V_W = 1$ V (see Figure 4-1). These two numbers are insufficient to determine the three capacitances in Figure 4-3. We may estimate one of the capacitances, C_{FC}, by estimating the size of the defect region in the channel. From the SGM line trace (Figure 4-2(c)), the defect region is approximately 30 nm in extent (or perhaps smaller, this distance is comparable to the resolution of the image). This distance can be interpreted as the screening length in the nanotube at the defect. From Coulomb blockade measurements of other devices, we know that the gate capacitance per length of our nanotube transistors is approximately 10 aF/μm. This gives a capacitive coupling $C_{FC} \approx 0.30$ aF between the defect region and gate. Solving for the other capacitances, we find $C_{TC} = 0.14$ aF and $C_{GT} = 0.16$ aF. The total capacitance

of the charge trap $C_{TT} = C_{TC} + C_{GT} = 0.30$ aF. From this value we can make a rough estimate of the size of the charge trap. The self-capacitance of a sphere of radius r is given by $C_{self} = 4\pi\varepsilon\varepsilon_0 r$, where ε_0 is the permittivity of free space and ε the dielectric constant of the medium in which the sphere is embedded, ~ 4 for SiO_2. Setting $C_{TT} = C_{self}$ gives $r = 6.7$ Å, reasonable for a vacancy site or complex of dangling bonds in the SiO_2 dielectric.

Chapter 5

Magnetoresistance in Spin Valves with Nanotube Channels

5.1 Introduction to Magnetoresistance due to Spin-Valve Effect

Electrons have two degrees of freedom: charge and spin. Electron charges have been utilized in device aspect for decades and become the central part of modern electronic device technology, especially semiconductor technology [92]. On the other hand, electron spins are late to be noticed for device purposes compared with charges. An electron has two spin states, up and down, since it is a spin-½ fermion. In the Seventies, pioneering researchers [93] showed that tunneling between ferromagnetic films can depend on electron spins, which has inspired much research and applications in both academia and industry. The word "spintronics" (from "spin electronics") is used to describe the manipulation of electron spins in solid materials in this new active field [94,95].

Materials which have non-zero magnetization in zero magnetic field (B-field) are called ferromagnetic (FM) materials. Such materials have different densities-of-state (DOS) for spin up and spin down, which causes unbalanced spin populations of spin up and spin electrons. Figure 5-1(a) depicts a FM material with magnetization pointing up or down, and its corresponding schematic DOS. The most common examples are iron, cobalt, nickel, and their alloys.

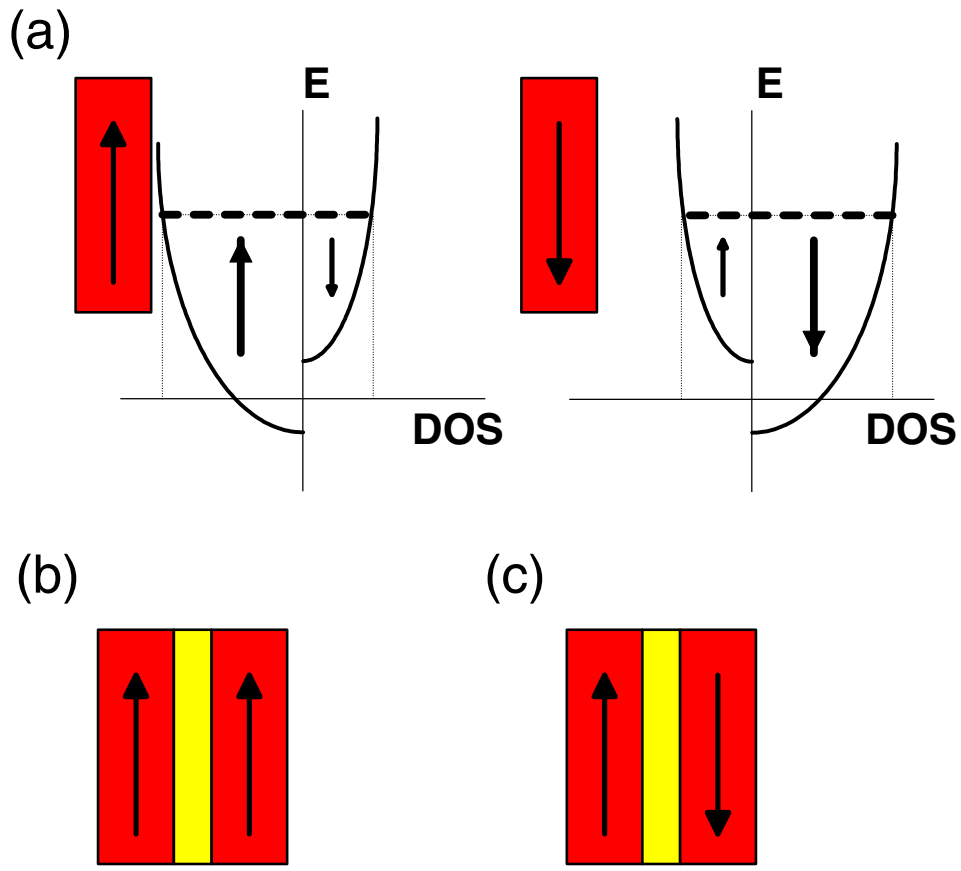

Figure 5-1. DOS of ferromagnetic metals and scheme of MR devices. (a) DOS of ferromagnetic metals with the magnetization pointing up or down. (b) and (c) show MR device with two parallel and anti-parallel magnetizations of ferromagnetic metals, respectively. The middle part of the device is made of non-ferromagnetic materials.

Electrons with different spins will experience different spin scattering strengths in FM materials because the DOS for spin-up and spin-down electrons at the Fermi level in FM materials are different; spin-up electrons travel more easily without spin scattering through the FM material with up magnetization than with down magnetization, and vise versa. For devices with a non-FM material sandwiched by two FM layers, the ease with which electrons go through depends on the configurations of the magnetizations of the two FM layers. For instance, when the

device is in the parallel state (p-state, see Figure 5-1(b)), spin-up electrons travel easily although spin-down electrons are blocked. However, when the device is in the anti-parallel state (ap-state, see Figure 5-1(c)), both spin-up and spin-down electrons are blocked. The result is that the overall resistance of the device in the parallel state is smaller than that in the anti-parallel state. Such an effect, called giant magnetoresistance (MR), is already utilized in read-out heads of magnetic hard drives as commercial products, while other applications are proposed, like magnetic random access memory [96,97] and spin-FETs [98].

The MR ratio is defined

$$MR\ Ratio \equiv \frac{R_{ap} - R_p}{R_{ap}} = \frac{G_p - G_{ap}}{G_p}, \qquad \text{Equation 5-1}$$

where R_p and R_{ap} (G_p and G_{ap}) are the resistances (conductances) in the p-state and ap-state, respectively. The simplest mechanism for giant MR effect (GMR) is that electrons from layer one FM tunnel through non-FM layer to the other FM without spin scattering. Suppose the conductance for spin-up (spin-down) electrons is proportional to the multiplication of the spin-up (spin down) DOS fractions of the two FM layers, then G_p and G_{ap} are

$$G_p \propto a_1 a_2 + (1 - a_1)(1 - a_2) \qquad \text{Equation 5-2}$$

and

$$G_{ap} \propto a_1 (1 - a_2) + (1 - a_1) a_2 \qquad \text{Equation 5-3}$$

respectively, where a_1 (a_2) is the fraction of the major tunneling electrons (the electrons with the spin parallel to the magnetization) of the first (second) FM layer. The expected tunneling MR ratio (*TMR*) should be [93]

$$TMR = \frac{2P_1P_2}{1+P_1P_2}, \qquad \text{Equation 5-4}$$

where $P_1 = 2a_1 - 1$ ($P_2 = 2a_2 - 1$) is spin polarization of first (second) FM layer.

The non-FM middle layer in MR devices not only can be an insulator, but also semiconductor, normal metal, or superconductor, depending on different purposes. In order to maximize GMR, the spin-polarized current injected from one FM layer needs to be preserved for a long distance while electrons are traveling in the non-FM layer so that the spin-polarized current can be detected by the other FM layer. In normal metals, such as copper [99] and aluminum [100], the spin-flip lengths λ_{sf} are 1000 and 650 nm at temperature 4.2 K, respectively, and 350 nm for both metals at 293 K. These metallic mesoscopic spin valves work very well, but lack tunablity. Semiconductors have a couple advantages, such as long λ_{sf} [101], carrier concentrations which can be tuned by chemical and electrical doping, and possible spin precession due to spin-orbit coupling [98]. However, the "conductivity mismatch" problem hinders the detection of the spin valve effect in FM-semiconductor-FM systems [102,103].

Carbon nanotubes are another possible candidate to transport spin-polarized current due to long mean free paths at room temperature and possibly very long spin-scattering lengths. MWNTs have been demonstrated to carry spin transport first [35,104,105], but SWNTs attract major interests for spin transport study lately [36,37,106-109] due to their one-dimensional electronic properties. In this chapter I would like to describe the work I have done with spin transport in SWNTs, and compare the results I have obtained with the results from other groups.

5.2 Device Fabrication

The device fabrication largely follows the procedures in Chapter 2 from section 2.1 to 2.3. Heavily n-doped Si chips with a SiO_2 layer of thickness t = 500 nm are used as device substrates. SWNTs are grown using a CVD. SEMs (Philips XL30 or Zeiss DSM 982 field-emission SEM (FESEM)) were used to locate the nanotubes, and electron-beam lithography followed by thermal evaporation of FM materials formed the contacts to a nanotube. The FM material we choose is permalloy (about 80% Ni, 20% Fe). It is known that permalloy possesses spin polarization P = 45% [110,111], which is higher than pure FM metals. Thicknesses of the permalloy thin-film contacts are about 30~50 nm. The permalloy electrodes are designed with some specific aspect ratios, which define the easy axes and tune the coercivities [112]. Several aspect ratios are tried: $1 \times 4\ \mu m^2$, $1 \times 8\ \mu m^2$; $0.5 \times 2\ \mu m^2$, $0.5 \times 4\ \mu m^2$; $0.4 \times 4\ \mu m^2$, $0.2 \times 12\ \mu m^2$; $0.3 \times 4\ \mu m^2$, $0.15 \times 12\ \mu m^2$; $0.3 \times 4\ \mu m^2$, $0.1 \times 12\ \mu m^2$; $0.5 \times 2\ \mu m^2$, $0.1 \times 14\ \mu m^2$; suggested by the literature [99,100,112]. Larger electrodes made of Cr/Au connect permalloy contacts to outside of the world, allowing us to perform electrical measurements to the devices. Figure 5-2 shows a nanotube two-probe magnetoresistance device with measurement setup (described in next section).

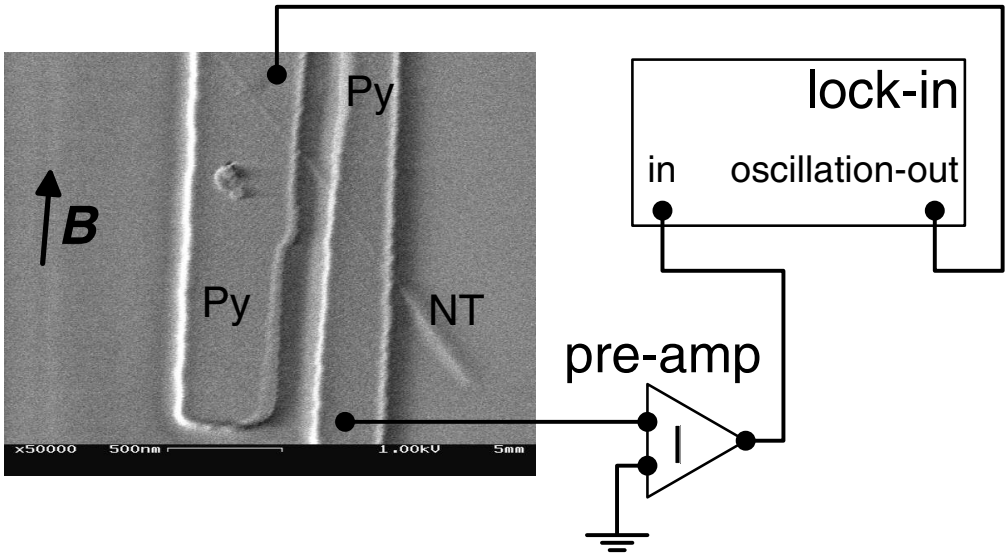

Figure 5-2. Nanotube MR device and two-probe AC conductance measurement setup. The permalloy electrode thickness is 50 nm, sizes are $0.4 \times 4\ \mu m^2$ and $0.2 \times 12\ \mu m^2$, and the electrode separation is 200 nm.

Devices were annealed at 350 ~ 400 ^oC under Ar and H_2 flow to lower the contact resistance before measurements.

After the devices are fabricated, it is advantageous to know how the magnetizations of FM contacts interact with applied *B*-field. Magnetic force microscopy (MFM) is designed to measure the local *B*-field on the surface [113,114]. Therefore, MFM is very good at visualizing the magnetization of the FM contacts because the magnetic tip of MFM interacts with *B*-field produced by FM contacts. MFM scanning while applying B-field was performed in the laboratory of Professor Romel Gomez with the aid of his student Seok-Hwan Chung [112].

Figure 5-3 shows the AFM and MFM images of the nanotube magnetoresistance devices. AFM and MFM images are taken simultaneously. Figure 5-3(a) is an AFM image. Five permalloy rectangular contact pairs (one big pair on the top left corners and four small pairs on the bottom right) and several alignment

markers can clearly be seen, while two nanotubes can barely be seen. Figure 5-3(b) to (f) are MFM images, where only permalloy pairs show up. Bright areas indicate the local *B*-field of the areas pointing to one of the normal directions to the surface, and dark areas indicate the local *B*-fields pointing to the opposite direction.

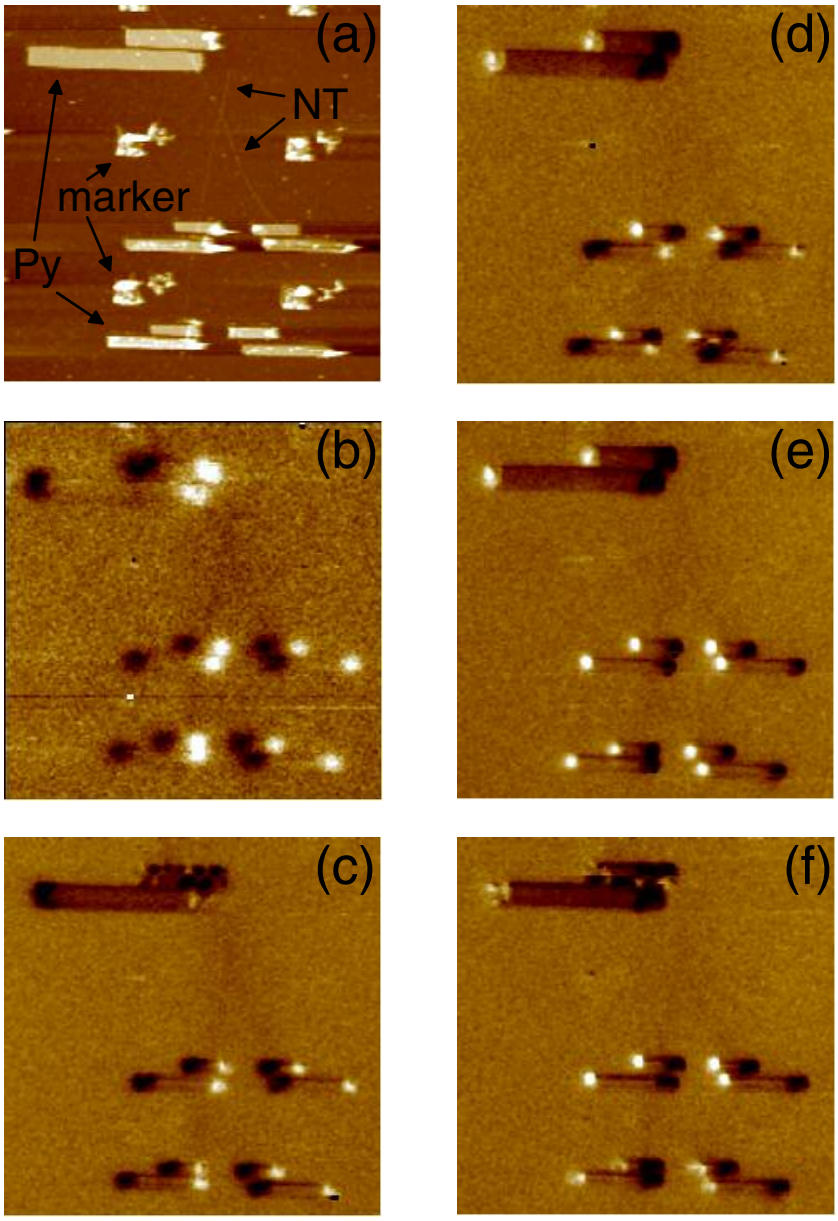

Figure 5-3. AFM and MFM images of FM electrodes. (a) shows an AFM image of devices. The thin lines are nanotubes. There are two sizes of FM electrode pairs. The bigger pair on

the top-left corner has 1×4 and 2×8 μm^2 electrodes, while the other four pairs have 0.5×2 and 0.5×4 μm^2. (b) shows a MFM image at zero B-field. The previous field direction before ramping back to zero is positive (pointing right). (c), (d) and (e) are MFM images taken at -18, -42, and -66 Gauss, respectively, while *B*-field is ramping toward negative direction. (f) shows a MFM image while *B*-field ramps back to zero from negative direction.

Figure 5-3(b) is taken at zero applied *B*-field. The previous applied *B*-field direction before ramping back to zero is positive (pointing right). All the magnetizations of the permalloy contacts remain in the previous applied *B*-field direction, which represents the ferromagnetism of the permalloy contacts. The devices are defined in the p-state. Also, all the permalloy contacts have single domain magnetization. After ramping applied *B*-field to -18 Gauss, Figure 5-3(c) is then taken. All the magnetizations of the contacts remain the same except the short electrodes of the big pair break into multi-domain. Figure 5-3(d) is taken at applied *B*-field equal to -42 Gauss. The magnetizations of both electrodes in the big pair point to the negative direction. The big pair is in the p-state. The small pairs are all in the ap-state; only the short electrodes change their magnetizations with applied *B*-field. Figure 5-3(e) is taken at applied *B*-field equal to -66 Gauss, which is enough to flip the magnetizations of all the contacts. The devices are all in the p-state again. Figure 5-3(f) is taken when applied *B*-field ramps back to zero from the negative direction.

MFM provides valuable information to design permalloy electrodes to obtain single domain contacts, which are desired for the MR study. From the observations of MFM images, several tips for designing permalloy contacts can be found. First, long and thin electrodes have single domains, and also have larger coercivities.

Second, the permalloy pairs with long and thin electrode are stable in either p-state or ap-state. Third, to have large applied *B*-field window for a device in the ap-state, the aspect ratios of two contacts in a pair need to be very different.

Although the overall contact magnetization of a long and thin contact looks like single domain, some very small localized magnetization domains are still possible according to the MFM images (for example, some short electrodes of small pairs in Figure 5-3(d) and (f)). Because nanotubes are nanoscale material, such local magnetization domains may cause ambiguities when making MR measurements.

5.3 Measurement Technique

MR experiments are carried out in ^{4}He or ^{3}He systems in order to have a *B*-field supply and stable low temperature environment. Figure 5-2 shows the set-up of a standard two-probe AC technique to measure differential conductance (or differential resistance) of the device. This setup is for measuring differential conductance at zero DC bias; with some voltage dividers in front, measuring differential conductance at non-zero DC bias is achievable.

In order to observe MR effects purely from spin injection-accumulation-detection in spin valve devices, a four-probe non-local measurement is necessary [99,115]. Non-local measurement technique allows separating from spin injection-accumulation-detection, other spin related effects, such as magnetocontact resistance, anisotropic magnetoresisitance, and Hall effect [99,115]. Figure 5-4 shows a nanotube four-probe spin valve device image and the four-probe non-local measurement scheme. For four-probe devices, two additional Cr/Au electrodes are added on the sides to contact nanotubes. An AC current is injected from the third to

the forth electrode while measuring the AC voltage between the first and the second electrodes. If the current injected is spin polarized and the spin scattering length in the non-FM material is longer than the channel length, a nonzero voltage should be expected and detected [99,100,115].

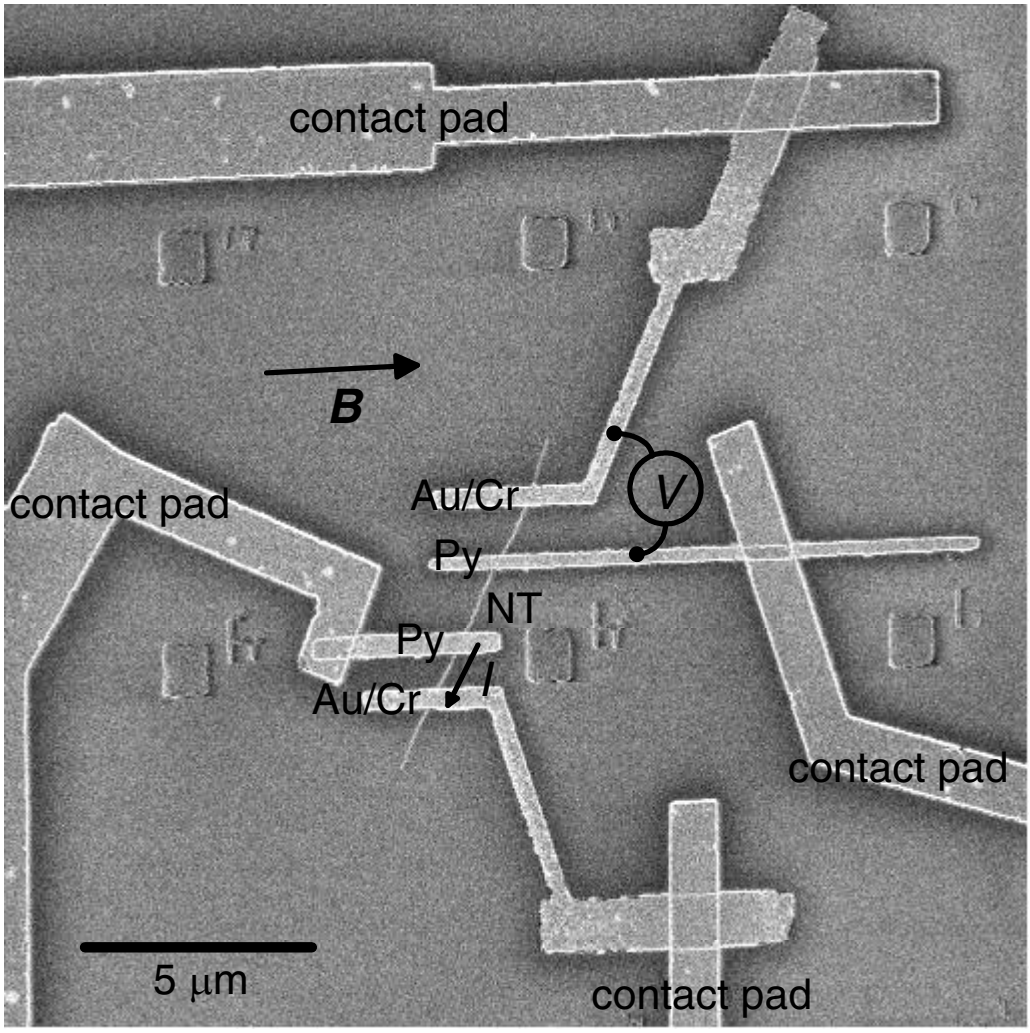

Figure 5-4. Nanotube four-probe spin valve device image and measurement setup.

5.4 Result and Discussion

The results of two-probe measurements are discussed first. The spin-valve nanotube devices do not show gate dependence at room temperature. The reason for that is the channel length L between two permalloy contacts (couple hundred of nm) is comparable to the thickness of gate dielectric and metal contact; the gate fields is hard to penetrate into the channels [116,117]. We thus can not distinguish whether the measured nanotubes are metallic or semiconducting. Figure 5-5 shows differential conductance (G) vs. applied B-field from a particular nanotube MR device with L = 200 nm. The data is taken at temperature T = 1.24 K, DC source-drain voltage V_{sd} = 0, gate voltage V_g = 0.3 V, AC excitation voltage V_{ac} = 0.1 mV, and applied B-field sweep rate is about 1.8 Gauss/s. The dashed vertical lines, which guide G changes due to the device switches between p-state and ap-state, are at ±300 and ±1000 Gauss applied B-field. The 300 and 1000 Gauss are the coervicities of short and long permalloy electrodes (0.4 × 4 μm^2, 0.2 × 12 μm^2), respectively. The coercivities of FM contacts and B-field window for ap-state are all larger than those in Figure 5-3 because the aspect ratios of permalloy contacts are larger.

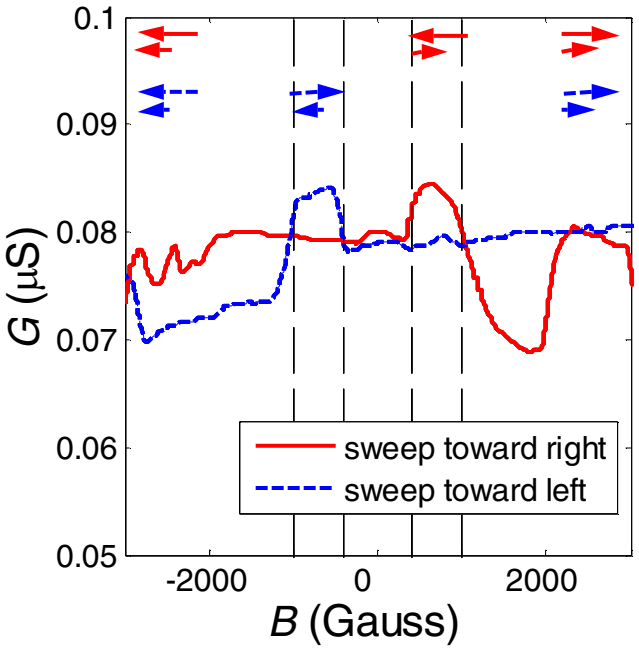

Figure 5-5. Conductance vs. *B*-field of a two-probe nanotube MR device at T = 1.24 K. Negative MR effect is demonstrated. The positive *B*-field is pointing right. The arrows indicate the FM contact magnetizations. The first row is for sweeping *B*-field from negative to positive; the second row is from positive to negative.

According to applied *B*-field and the ramping history, the device is either in p-state or ap-state. If the nanotube MR devices works similar to magnetic tunneling junction devices, TMR = 34% should be expected according to Equation 5-4 and P_1 = P_2 = 45% for permalloy. However, the device in Figure 5-5 has higher conductance (lower resistance) when it is in ap-state rather than in p-state; the device possesses a negative TMR of about -7 %. It is counterintuitive to have a device with a negative MR effect. The possible reasons or explanations are: (1) The local magnetic moments connected to the nanotube are not aligned with the net magnetization of the contact. (2) The electron spins precess in the nanotube. (3) Two permalloy contacts and the nanotube form a quantum dot where Kondo resonance occurs closer to the Fermi energy for the antiparallel magnetization orientation [118]. (4) Electron

tunneling through a SWNT quantum dot with asymmetric tunnel barriers is on resonance [109]. However I do not have further information to prove which one is more likely.

Figure 5-6 shows G vs. applied B-field in nine continual sweeps from another device. The contacts of this device have the same geometry of the previous described one. The data is taken at temperature T = 0.3 K, DC source-drain voltage V_{sd} = 0, gate voltage V_g = -0.47 V, AC excitation voltage V_{ac} = 0.01 mV, and applied B-field sweep rate is about 4.5 Gauss/s. The permalloy evaporation conditions are the same. The channel length L is also 200 nm. The coercivities of short and long permalloy electrodes are 300 and 500 Gauss, respectively. The long electrode has slightly smaller coercivity than that of the device in Figure 5-5. The average *TMR* is about +3.5%; indicating a positive MR effect which is easier to understand in terms of spin injection-transport-detection. Although this device has some other switching and MR effects, it has better consistency in this set of sweeps.

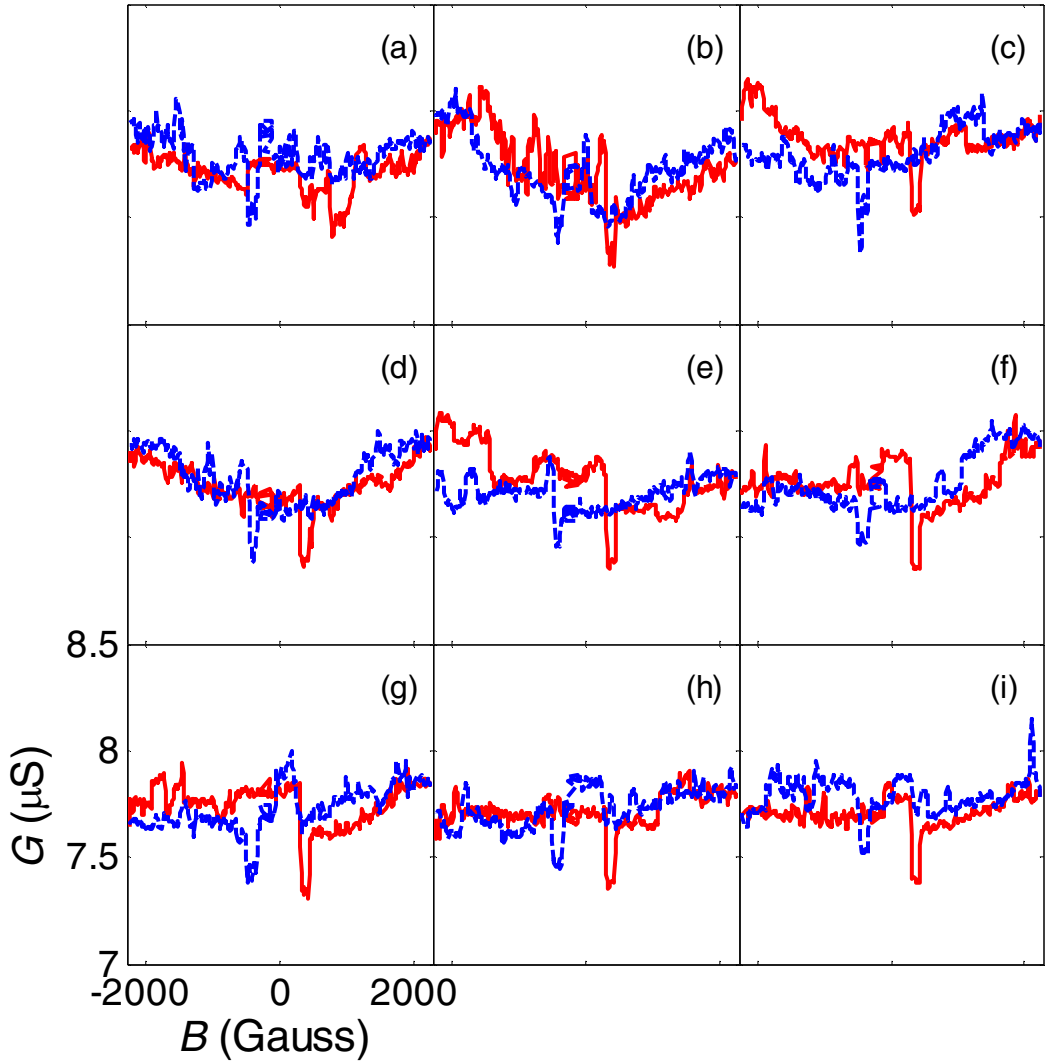

Figure 5-6. Conductance vs. *B*-field of a two-probe nanotube MR device with continuous nine *B*-field sweeps at $T = 0.3$ K. Positive MR effect is demonstrated.

Sometimes, one of the peaks or both peaks are missing. Figure 5-7 shows *G* vs. applied *B*-field in another three continual sweeps of the same device and the same settings in Figure 5-6 (except $V_g = 0$). In Figure 5-7(a) (the first sweep), the right sweep peak is missing, while in Figure 5-7(c) (the third sweep), the left sweep peak is missing. The reason is unclear; however the most possible explanation is somehow both FM contacts switch at the same time responding to the applied *B*-field. One

more thing to be noticed in this figure is *MR ratio* is ~ 17%, higher than the previous and closer to the expected 34% for the device without spin flipping predicted by the simple Julliere model.

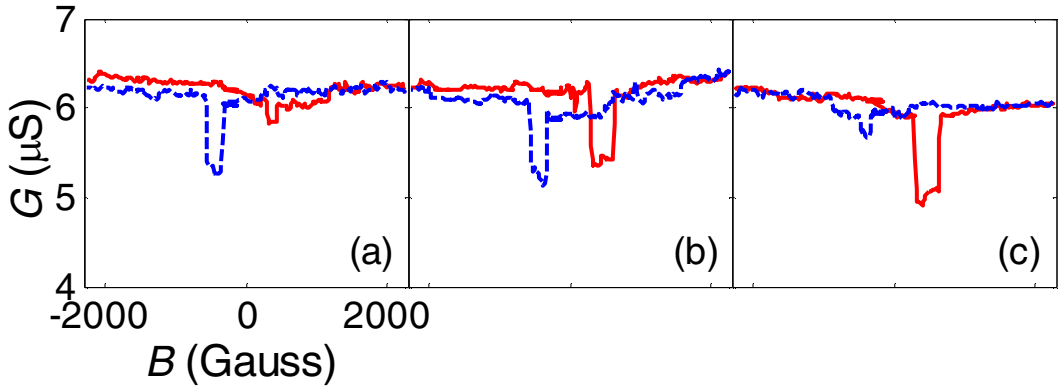

Figure 5-7. Conductance vs. *B*-field of a two-probe nanotube MR device with three different *B*-field sweeps at $T = 0.3$ K. (a) and (c) show one peak is missing; (b) shows none of both peaks is missing.

Figure 5-8 shows the hysteresis effect of the same MR device. The settings are the same as those in Figure 5-7. Only the short electrode switches its magnetization. Around zero bias, the device can be either in p-state or ap-state depending on the history of the applied *B*-field. This memory effect has possible device applications in memories and transistors.

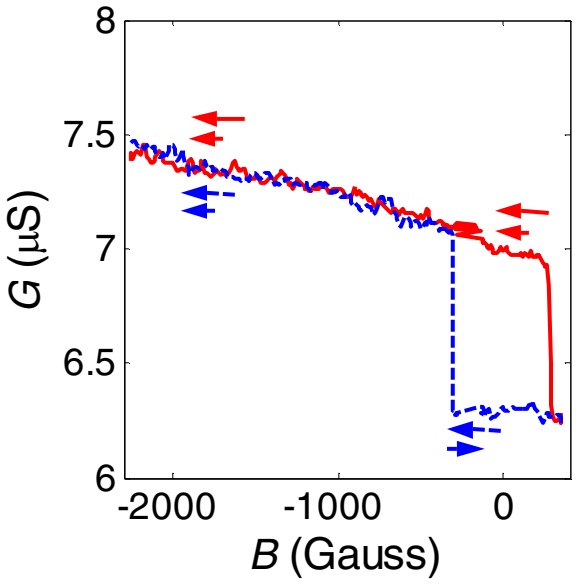

Figure 5-8. Conductance vs. *B*-field at $T = 0.3$ K demonstrating a memory effect. The arrows indicate the FM contact magnetizations.

Because both p-state and ap-state are stable, other settings may be changed to see how these two states behave. Figure 5-9(a) shows G vs. V_{sd} at both p-state and ap-state. The largest difference between both states is at zero V_{sd} (0.3 mV offset due to small the offset of electronics (DAC board)). Roughly above 1.3 mV V_{sd}, the difference is diminishing. Figure 5-9(b) shows the calculated *TMR* from Figure 5-9(a). The trend of decreasing *TMR* with increasing V_{sd} is clearly seen; however, the reasons for that are still unclear.

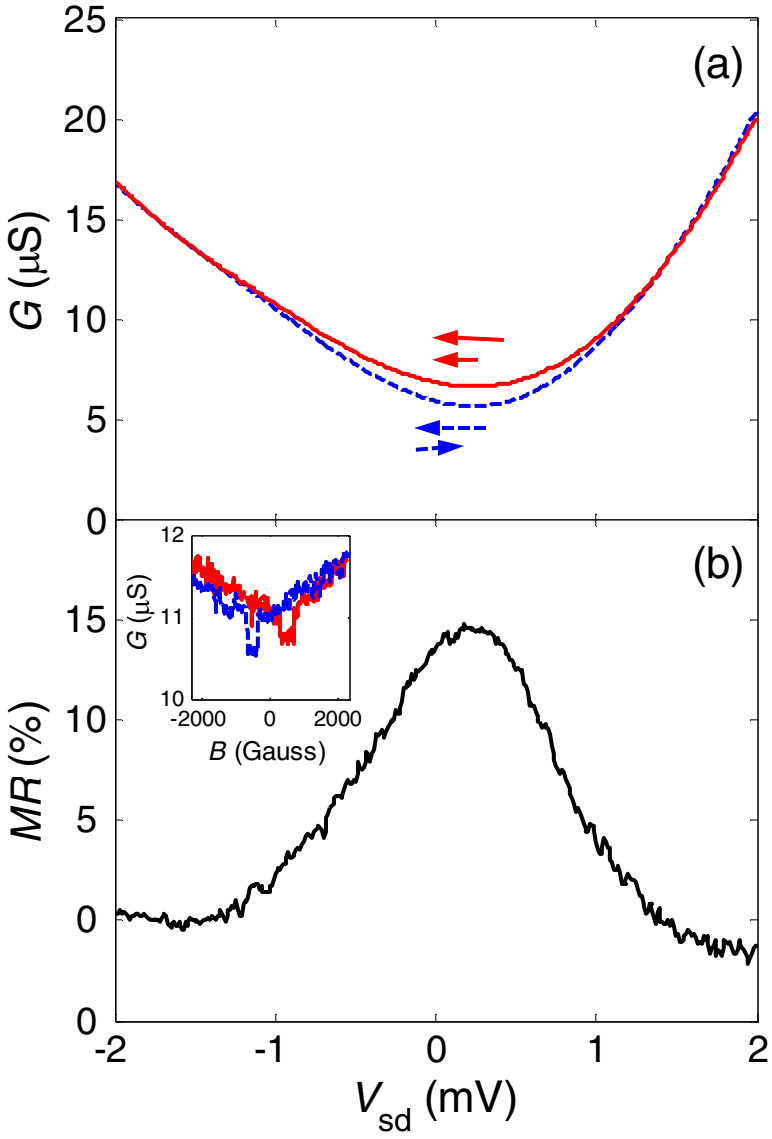

Figure 5-9. MR effect with respect to V_{sd} at T = 0.3 K. (a) shows conductance vs. V_{sd} while the device is at parallel state (solid line) or antiparellel state (dashed line) at zero B-field. (b) shows MR ratio vs. V_{sd} derived from (a). Inset shows conductance vs. B-field at V_{sd} = 1 mV.

When larger V_{sd} (larger 3 mV) is applied, some switching events happen (data not shown). The device transport behavior is very sensitive to all the settings, which makes the experiment very difficult.

In the previous two described devices, besides the major MR effect due to spin injection-transport-detection, there are also other magnetoresistance effects present, which are not fully identified. Sometimes the major MR effect can not be seen as well; this appears to be related to gate voltage V_g, temperature T, sweep rate of applied B-field. Even though all the factors are controlled, G vs. applied B-field at different sweeps are not consistent. Such inconsistency prevents us from doing more systematic study of MR effect in nanotube devices.

Unfortunately, since the number of working devices is very small; the spin-flip length l_s can not be extracted from the experiments. (Nevertheless, by assuming all the spin scattering events happen in the nanotube, the *TMR* should be

$$TMR = \frac{2P_1P_2e^{-L/l_s}}{1+P_1P_2e^{-L/l_s}}. \qquad \text{Equation 5-5}$$

Using TMR = 17% observed in one device (L = 200 nm and $P_1 = P_2$ = 45% for permalloy), the lower bound of l_s = 260 nm can be extracted.) Only two out of tens of devices show any MR effects; the reasons for this are also not clear. Possible explanations are the following. (1) Strong spin-flip scattering could be present at the nanotube-metal interface. (2) Contact to the nanotube could be made through an intermediate non-magnetic region (such as amorphous carbon, or a section of the nanotube) (3) The contacts of devices are mechanical unstable. Atomic motion in the contacts generates telegraph noise. (4) Local magnetization fluctuations may play an important role due to the intrinsic nanoscale of nanotubes.

Four-probe spin valve nanotube devices have been fabricated and measured with both conventional and non-local measurement geometries. The non-local measurement geometry is described in Figure 5-4, while the conventional

measurement geometry injects the current from outside electrodes and measures the voltages with the inside electrodes. The comparisons and advantages between these two measurement geometries for spin-related transport are described in detail in Reference [115]. However, I failed to observe MR effects in four-probe spin-valve nanotube devices. One of the possible problems is conductivity mismatch [102,103]; the conductivity of non-FM layer is much less than those of contacts. Rashba [119] has suggested that making tunnel barriers between FM and non-FM layers will solve this problem. Another possible problem is additional current paths in the non-local measurement geometry due to the fact that the nanotubes may be MWNTs [120].

During the time I performed my research on nanotube spin valves, other research groups have also worked on this topic and have published some results. Recently, ferromagnetic semiconductors have been used as FM materials to contact nanotubes to solve the conductivity mismatch problem [107], and MR effects are seen [107]. However, the sizes of the contacts are not controlled, which makes single domain magnetization of FM contacts at all applied *B*-field impossible and the switching events complex. Moreover, MR effects are even observed at devices with one FM contact and one non-FM metal contact. The results, therefore, are confusing.

The group of van Wees (who has pioneered all-metal four-probe spin-valve experiments [99,100,115,121]) has also studied nanotube four-probe spin-valve devices in a non-local geometry [36]. MR effects due to spin injection-accumulation-detection have been reported. The results are promising, but more work is needed to determine the spin scattering length in nanotubes.

The Alphenaar group in University of Louisville has developed a shadow evaporation technique to fabricate short nanotube MR devices (channel length on order of 10 nm) [37], achieving a high yield of working MR devices. However, single-domain magnetization switching is lacking among devices according to the device geometry and transport results.

Electric-field control of spin transport has been realized recently by tuning resonant tunneling through a SWNT quantum dot in FM-SWNT-FM devices [109]. The spin-dependent transmission probability T^{σ} for electrons with energy E and spin σ can be written as [109]

$$T^{\sigma} = \frac{\Gamma_1^{\sigma}\Gamma_2^{\sigma}}{(E - E_0^{\sigma})^2 + (\Gamma_1^{\sigma} + \Gamma_2^{\sigma})^2/4}, \qquad \text{Equation 5-6}$$

where $\Gamma_1^{\sigma} = \gamma_1(1 + \sigma P_1)$ ($\Gamma_2^{\sigma} = \gamma_2(1 + \sigma P_2)$) is the spin-dependent coupling to the first (second) ferromagnetic lead, γ_1 and γ_2 are the bare coupling and E_0^{σ} is the spin-dependent energy level of the quantum dot. If the couplings to the leads are asymmetric (for example, $\Gamma_1^{\sigma} << \Gamma_2^{\sigma}$), when the transmission is off resonance, that is when $|E - E_0^{\sigma}| >> \Gamma_1^{\sigma} + \Gamma_2^{\sigma}$, T^{σ} is small and proportional to $\Gamma_1^{\sigma}\Gamma_2^{\sigma}$, yielding the normal positive *TMR* of $2P^2/(1 - P^2)$ (assuming $P_1 = P_2 = P$) [109]. On the other hand, when the transmission is on resonance, that is when $|E - E_0^{\sigma}| << \Gamma_1^{\sigma} + \Gamma_2^{\sigma}$, T^{σ} is proportional to $\Gamma_1^{\sigma}/\Gamma_2^{\sigma}$, yielding an anomalous negative *TMR* of $-2P^2/(1+P^2)$ [109]. By applying gate voltages, which change E_0^{σ}, the magnitude and the sign of *TMR* can be tuned in a predictable way. Possibly this effect can explain my observation of negative *TMR*; however, my measurement of negative *TMR* is apparently not tunable by gate as discribed above, especially when many random telegraph noise signals are present (data not shown).

Recent results on nanotube MR devices will likely generate much attention again in basic research as well as applications.

Chapter 6

High-Bias Transport in Semiconducting SWNTs

6.1 Introduction to High-Bias Transport in Nanotubes

One of the most striking aspects of carbon nanotubes is that they can carry extremely large current densities, exceeding 10^9 A/cm^2 [45,48,122], orders of magnitude larger than those at which metal wires fail by electromigration [123]. In m-SWNTs, a saturation of 25 μA was observed at high drain biases in low contact resistance devices [45]. Yao *et al*. have first studied current saturation of 25 μA at high bias voltages in m-SWNTs and successfully explained the phenomenon in terms of scattering of electrons due to optical or zone-boundary phonon emission [45]; the phonon energy hf is about 160 meV. The mean free path of optical phonon emission backscattering l_{op} is ~ 10 nm. If the m-SWNT channel is much longer than l_{op}, such scattering processes then occur frequently and will establish a separation about 160 meV between the quasi-Fermi levels of left- and right-moving carriers (see Figure 6-1, duplicate from Ref. [45]). This inelastic phonon emission at energy hf = 160 meV explains the current limit of $(4e/h)(hf) \approx 25$ μA at high electric field [45,47,69], where $4e^2/h$ is the quantum conductance for the lowest two crossing subbands.

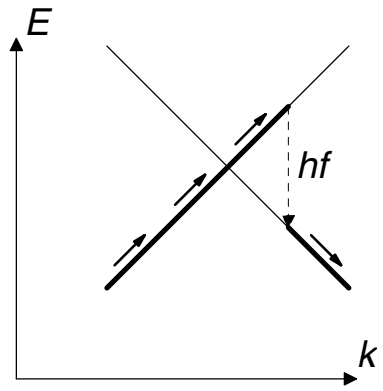

Figure 6-1. Scheme of phonon scattering in m-SWNTs. The solid lines represent the states occupied by carriers. The dashed arrow indicates the inelastic phonon emission.

The current-carrying capacity and reliability studies of MWNTs under current densities greater than 10^9 A/cm^2 show that no observable failure in the nanotube structure and no measurable change in the resistance up to 2 weeks [48]. Also in contrast to metal wires, MWNTs do not fail continuously due to electromigration; instead, they fail via a series of sharp current steps, which correspond to the breakdown of MWNT shells [122,124]. By using electrical breakdown of MWNTs, it was found that metallic and semiconducting shells carry similar saturation currents 20 ~ 25 μA [122,124]. Bourlon, *et al*. proposed a model of competition between electron-phonon scattering and Zener tunneling to further explain the geometrical dependence of saturation currents in metallic and semiconducting single shells in MWNTs [125].

Low contact resistance devices have been achieved with semiconducting SWNTs (s-SWNTs) by using palladium (high work function metal) to form ohmic contacts to the valence band of the s-SWNT [44]. Current saturation at 25 μA in ohmically-contact s-SWNT devices is not obvious in the data shown in the paper [44]; instead, the current seems to increase without limit (though this was not noted in

the paper). Therefore, there is no reason to assume that the limit in s-SWNTs is identical to that in m-SWNTs. This is reasonable, since the electronic band structure is different: the equivalent zero-momentum phonon emission process in semiconducting nanotubes involves relaxation of electrons across the band gap, which is order of hundreds of meV, usually greater than the energy of zone-boundary and optical phonons.

Following the thoughts above, I recognized that high-bias transport experiments and studies on single s-SWNTs are lacking. I performed a series of high-bias experiments on s-SWNTs, and these experiments and modeling of the transport at high bias form the second half of my dissertation.

Figure 6-2 shows the measured I_d vs. V_d up to ±10 V at different gate biases V_g for a s-SWNT-FET with d = 2.4 nm and L = 20 μm. Electrical measurements were performed by grounding the source electrode (V_s = 0) and applying V_d to the drain, and V_g to the gate, while measuring the drain current I_d. We note several striking features of the data. First, the data is highly symmetric under reversal of both V_d and V_g, indicating good electron-hole symmetry in s-SWNTs due to the fact that the energy-band structure of the conduction band and the valence band are identical near the charge-degeneracy point [126]. Second, the currents significantly exceed 25 μA with no obvious evidence of saturation, which stands in contrast to the currents observed in metallic SWNTs. In Chapter 7 and 8 I will further discuss why s-SWNTs can have higher currents than metallic SWNTs.

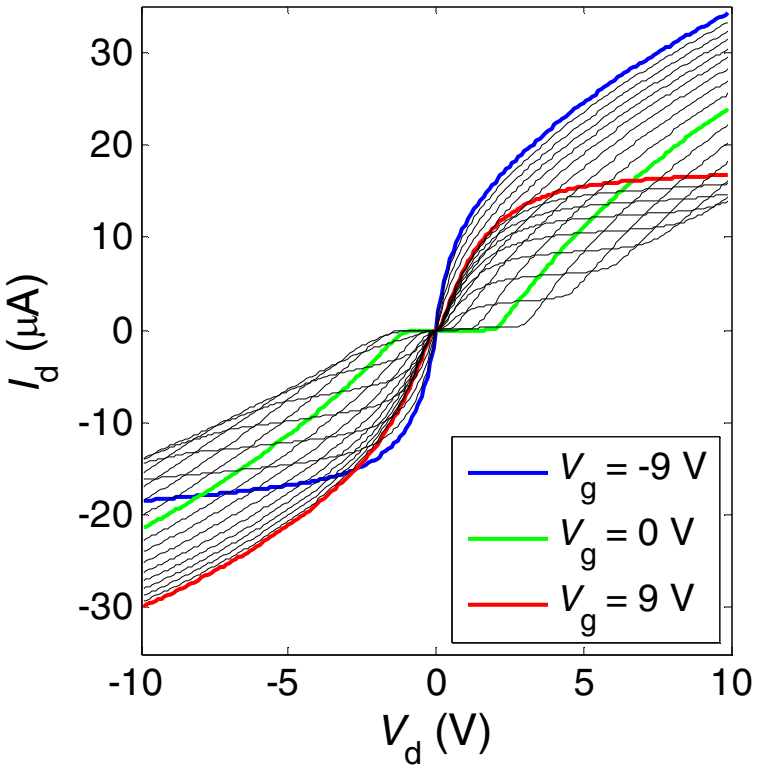

Figure 6-2. Semiconducting nanotube transistor. Drain current I_d as a function of drain voltage V_d at gate voltages V_g from -9 V to 9 V, in 1 V steps is measured. V_d is applied up to 10 V. Temperature is 4.2 K.

When V_g is greater (smaller) than the nanotube potential, electrons (holes) are expected to accumulate in the nanotube, and n-type (p-type) behavior is expected. Figure 6-3(a) (Figure 6-3(b)) show a Si-SiO_2-CNT capacitor accumulating electrons (holes) in the nanotube with applied biases $V_g > V_d$ & V_s ($V_g < V_d$ & V_s). At finite positive (negative) gate voltages, the curves of Figure 6-2 show typical n-type (p-type) transistor behavior, i.e. saturation of I_d at positive (negative) drain voltage. The saturation is followed by an increase in the current as V_d becomes greater than $2V_g$. We interpret this increase in I_d as the change from majority electron to majority hole current or vice versa. $V_d = 2V_g$ corresponds to the symmetric bias condition

[127,128], equivalent to holding $V_g = 0$ and applying equal and opposite voltages to source and drain; at this point electron and hole currents should be equal.

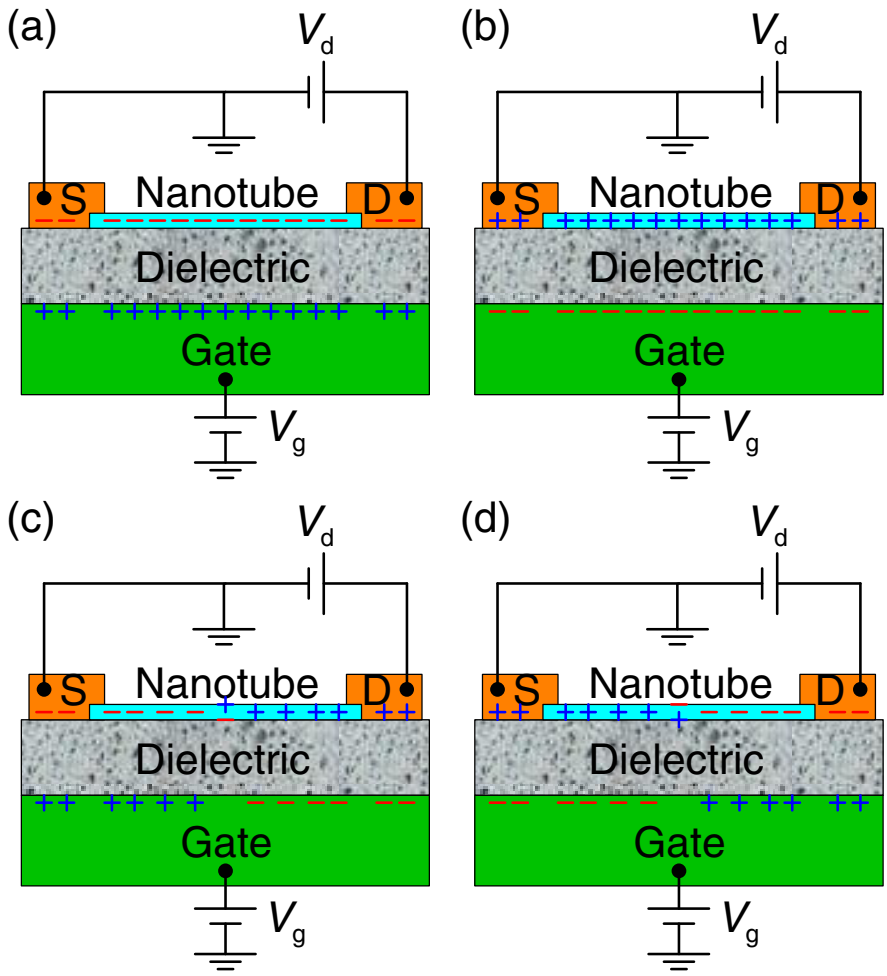

Figure 6-3. Scheme of a Si-SiO_2-CNT capacitor. (a) For the case of $V_g > V_d$ & V_s. (b) $V_g < V_d$ & V_s. (c) $V_d > V_g > V_s$. (d) $V_d < V_g < V_s$. $V_s = 0$ in all cases.

Figure 6-4 shows a color-scale plot of I_d as a function of V_d and V_g, which is another way to represent the same data in Figure 6-2. The colors indicate the amount of current. The two dashed lines represent $V_g = V_s$ and $V_g = V_d$, which mark the boundaries separating the unipolar bias regimes from the ambipolar bias regimes. In the unipolar bias regimes, where V_g is larger than both V_d and V_s for electrons to

accumulate, or V_g is smaller than both V_d and V_s for holes to accumulate, there are only majority carriers to take into account and minority carriers are few enough to be neglected. In the ambipolar bias regimes, where V_g is between V_d and V_s (see Figure 6-3(c) for $V_d > V_g > V_s$ and Figure 6-3(d) for $V_d < V_g < V_s$), both majority carriers and minority carriers play important roles in the nanotube channel.

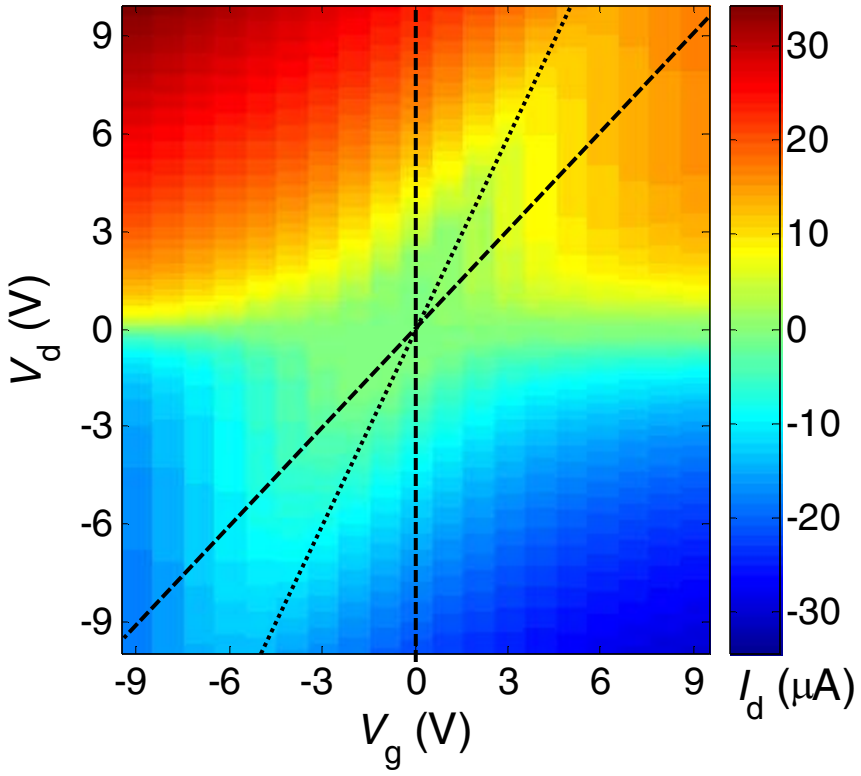

Figure 6-4. Color-scale plot of Id as a function of V_d and V_g at T = 4.2 K. The dotted line indicates $V_g = V_d/2$; the current minimum occurs along this line. The dashed lines are the boundaries between unipolar and ambipolar transport.

6.2 Unipolar Transport

Figure 6-5 shows an example of a s-SWNT band diagram in the unipolar (hole conduction) bias regime (see Figure 2-5(b) for the scheme of device geometry). This band diagram results from a calculation performed as described in Chapter 7; most

importantly, contact effects are ignored. The Fermi level of the drain contact is 5 eV higher than that of the source contact due to V_d = -5 V is applied. The gradient of the bands denotes the electric field strength. The potential energy rises from the source contact to the drain contact with the largest slope occurring near the drain contact. The blue dashed line is the quasi Fermi level of holes in the nanotube, showing only holes are built up in the whole nanotube. Further discussion of s-SWNTs in the unipolar bias regimes will be found in Chapter 7.

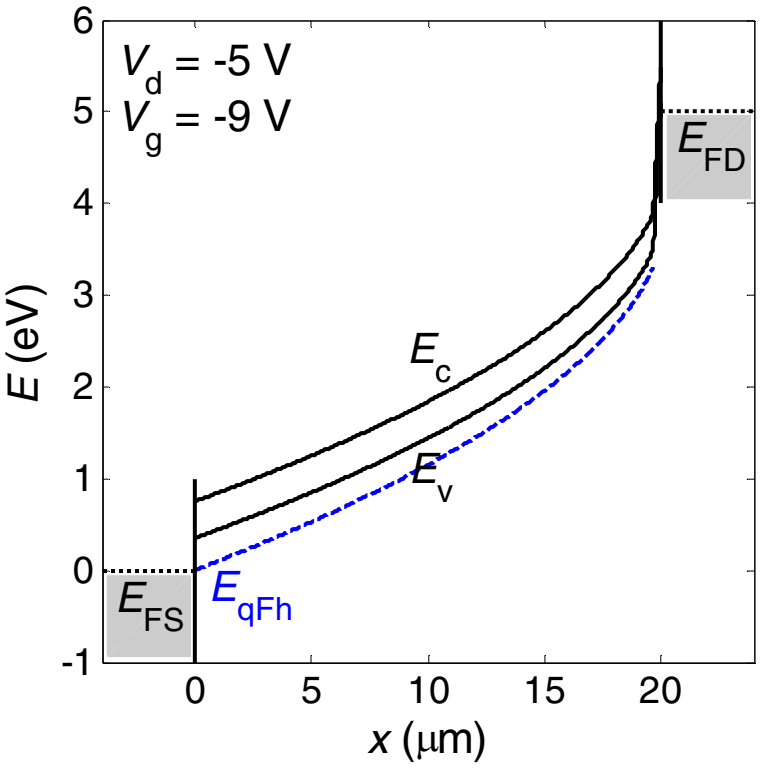

Figure 6-5. Scheme of a s-SWNT band diagram at a unipolar bias region (V_d = -5 V, V_g = -9 V). The left and right sides are Fermi levels of the source and drain contacts, respectively. The vertical lines indicate the metal-nanotube junctions. The middle part is the nanotube, whose conduction and valence band edges are shown by two black lines. The quasi Fermi level of holes is indicated by the blue dashed line.

6.3 Ambipolar Transport

Figure 6-6 shows an example of a s-SWNT band diagram in the ambipolar bias regime, calculated as described in Chapter 7. In Figure 6-6 the contact effects are ignored as in Figure 6-5. The potential energy rises from the source contact to the drain contact with the largest slope occurring in the middle of the nanotube channel. The blue and red dashed lines are the quasi Fermi levels of holes and electrons in the nanotube, respectively. Holes are accumulated in the nanotube near the source while electrons are accumulated near the drain. In the middle, both types of carriers are present. This example of V_d = -5 V and V_g = -2.5 V is actually a symmetric bias case since $V_d = 2V_g$. It is equivalent to $V_g = 0$ and $V_d = -V_s$ = -2.5 V. Therefore, the picture is symmetric in terms of the source and the drain. The symmetric bias cases are indicated by a dotted line in Figure 6-4, where the current is at a minimum with variation of the gate voltage.

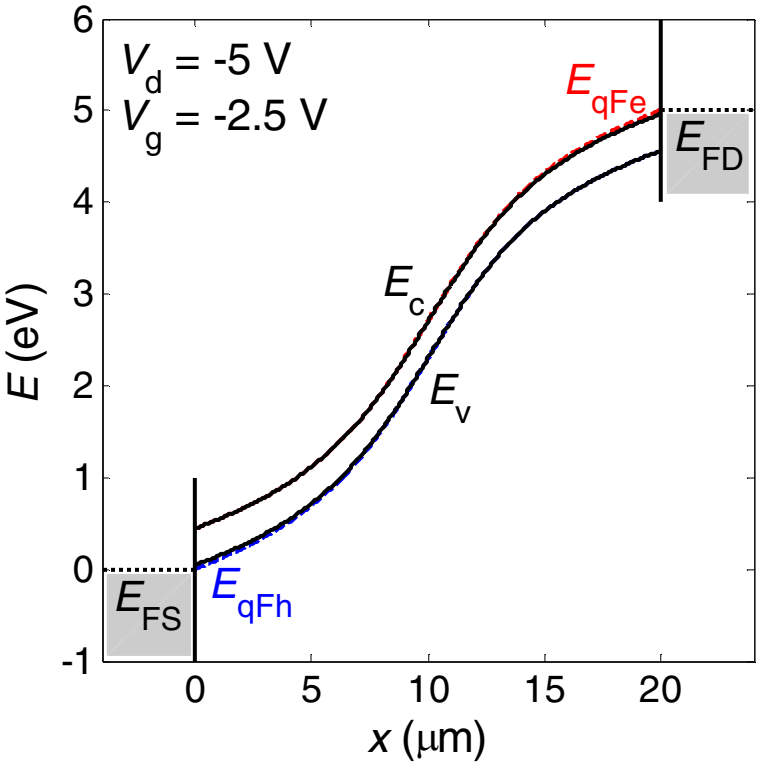

Figure 6-6. Scheme of a s-SWNT band diagram at an ambipolar bias region (V_d = -5 V, V_g = -2.5 V). The left and right sides are Fermi levels of the source and drain contacts, respectively. The vertical lines indicate the metal-nanotube junctions. The middle part is the nanotube, whose conduction and valence band edges are shown by two black lines. The quasi Fermi levels of electrons and holes are indicated by the red and blue dashed lines, respectively.

The ambipolar bias regime is a subject of much recent scientific and technological interest. In the ambipolar bias regime because electrons are injected from one contact into the s-SWNT and holes are injected from the other, electrons and holes meet in the channel (s-SWNT) and recombine rapidly due to strong Coulomb interaction between them. In part of the recombination, the energy will be relaxed by emitting light (photons). The light emitting process induced by applying electric bias in s-SWNTs is called electroluminescence, and was demonstrated by

IBM group [49,129]. Further discussions about s-SWNTs in the ambipolar bias regime will be in Chapter 9.

Chapter 7

High-Bias Transport of Semiconducting SWNTs in the Unipolar Regime

7.1 Phenomenological Carrier Velocities under Electric Field

The movement of charges is current. In a solid-state system, the velocity of an electron is often described by

$$\vec{v}(\vec{k}) = \frac{1}{\hbar}\frac{\partial E(\vec{k})}{\partial \vec{k}} = \frac{1}{\hbar}\nabla_{\vec{k}} E(\vec{k}) \qquad \text{Equation 7-1}$$

when the electron is occupied a state $\vec{k}$ with energy $E(\vec{k})$. However, there is no current in an equilibrium system due to the carriers moving in all directions, which produces zero net current. When there is a voltage difference between two ends of a conductor, a non-zero net current will flow due to unbalanced charge flows.

In a sample length L shorter than the momentum relaxation length l_e (mean free path) of electrons, the electrons transport is in the ballistic regime [41,130]. There the average electrons may traverse the device without scattering. On the other hand, when $L >> l_e$, the transport is in the classical or diffusive regime, where the resistance of the sample is proportional to L, i.e. Ohm's law is obeyed.

In classical transport, Ohm's law can be rewritten to an average carrier velocity v proportional the electric field F which the carriers experience (consider one dimensional case):

$$v = \mu F , \qquad \text{Equation 7-2}$$

where μ is a material-dependent constant called mobility. In general, approximating mobility as a constant is only valid for low electric fields. As F gets larger, μ is no longer a constant with respect to F, since more scattering mechanisms become available as the carriers gain more energy. In many materials the mobility follows a phenomenological equation,

$$\mu^{-1} = \mu_0^{-1} + \frac{|F|}{v_s}, \qquad \text{Equation 7-3}$$

where μ_0 is the zero-field mobility and v_s is the saturation velocity. Such behavior is called velocity saturation. Figure 7-1 shows different carrier velocity behaviors under the influence of F: The dashed line represents the constant mobility behavior, which shows the carrier velocity increasing linearly with F, while the solid line represents the saturation velocity behavior, which shows the carrier velocity saturates in the high F. (Here the values of μ_0 and v_s are taken from fits to this model for a particular nanotube device described later in this chapter.) Note that the dotted line shows the Fermi velocity of the carriers in a SWNT at high density, which should be the upper bound of the carrier velocity. The plot indicates that at modest experimentally accessible electric fields (comparable to those applied in Chapter 6, Figure 6-2) deviations from constant mobility are expected in SWNTs.

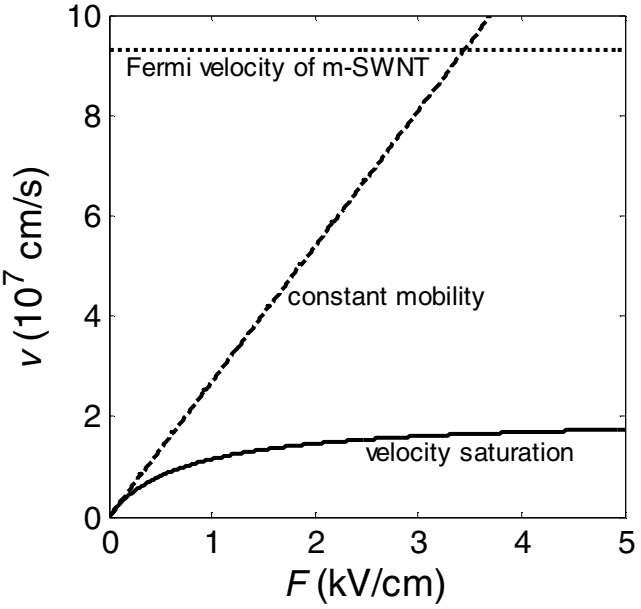

Figure 7-1. Different carrier velocity behaviors under the influence of F. The dashed and solid lines represent the constant mobility and the saturation velocity behaviors, respectively. The dotted line shows the Fermi velocity of the carriers. (The mobility of 2.7×10^4 cm^2/Vs is used for plotting constant mobility, $\mu_0 = 2.7 \times 10^4$ cm^2/Vs and $v_s = 2 \times 10^7$ cm/s for saturation velocity, and 9.3×10^7 cm/s for Fermi velocity of m-SWNT.)

In Chapter 6, we have briefly described applying high-bias to s-SWNTs. Such measurements help to know how the velocities of the carriers in s-SWNTs behave under the influence of high electric fields. In the unipolar bias regimes, the carrier velocities are simpler to analyze since there is only one type of carrier in the channel. Hence if we know the carrier density n in a s-SWNT channel from the gate capacitance and measure the current I under biases, along with (assuming that the carriers are electrons)

$$I = nev, \qquad \text{Equation 7-4}$$

where e is the electronic charge, we can easily estimate the carrier velocity. This estimation of the carrier velocity assumes that all the carriers move at this velocity,

and uses the charge-control model ($n \propto V_g$) to determine the carrier density. It is well known that this is a very crude approximation, and the velocity extracted in this way is always less than the peak value. The approximation is too simplistic for the following reasons. In a semiconductor transistor, the velocity and density of the carriers are strong functions of position in the channel. As a result, device modeling is necessary to understand the device behaviors under different biases and the carrier behaviors under the effect of the electric fields [46].

7.2 Experiment Results

Before doing the modeling, I would like to describe the experimental results of high-bias transport of s-SWNTs in the unipolar regime that the device modeling is going to compare. We have investigated several s-SWNT devices with similar transport behavior. Some devices showed only unipolar p-type behavior; we associate these devices with Ohmically-contacted nanotubes or large-bandgap nanotubes. Only the ambipolar devices (having both good hole and electron conductions), which we assume to have small Schottky barriers (SBs) to both valence and conduction bands, are discussed in this chapter, because our goal is to extract both hole and electron behaviors in s-SWNTs, particularly under high F. Under this condition, the SBs are very transparent and can be neglected in modeling.

The measured semiconducting nanotube diameters d range from 2 to 2.4 nm (with band gap about 0.35 ~ 0.42 eV), and the nanotube lengths between the contacts (channel length L) range from 10 to 20 μm. The measured nanotube diameters indicate they are SWNTs or small MWNTs. (We expect that in the case of a small MWNT with all semiconducting shells that the transport occurs primarily in the

outermost shell with the lowest bandgap.) Here we investigate high-bias transport up to bias voltages of 10 V, corresponding to average electric fields up to 5 ~ 10 kV/cm.

We focus on the transport data from one particular device, with d = 2.4 nm and L = 20 μm. Figure 7-2 shows the experimental I_d as a function of V_d in the unipolar regime (V_g is smaller than both V_d and V_s) with holes as majority carriers at V_g from -9 V to -1 V, in 1 V steps. This s-SWNT-FET device behaves as a normal p-type FET, with current saturating at negative V_d and increasing at positive V_d. The current significantly exceeds 25 μA at positive V_d as described in Chapter 6.

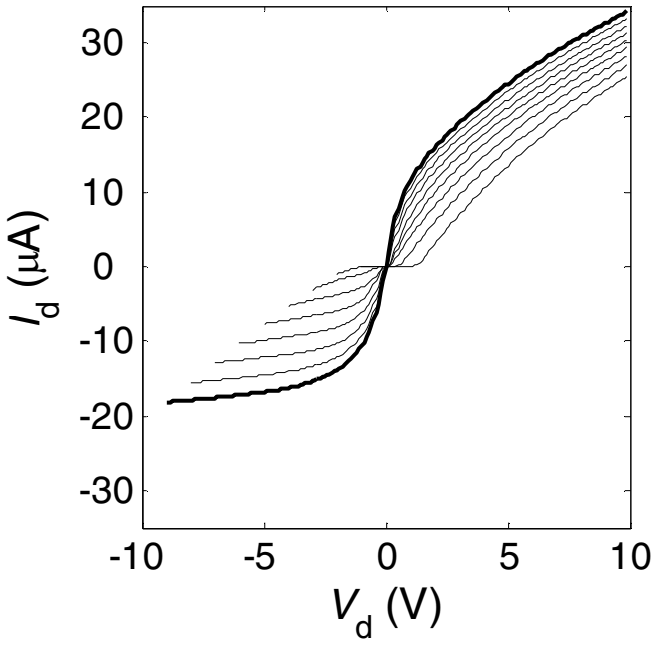

Figure 7-2. Experimental I_d as a function of V_d at V_g from -9 V to -1 V, in 1 V steps. The thick curve is for V_g = -9 V.

7.3 Device Modeling

The model device geometry is schemed in Figure 2-5(b), with L = 20 μm, d = 2.4 nm, and t = 500 nm, to match the geometry of the device shown in Figure 7-2. x

= 0 and $x = L$ locate at left (source) and right (drain) ends of the nanotube (defined by the nanotube-contact junction). Here we have used the electrostatic gate capacitance per length

$$c_{\mathrm{g,e}} \approx \frac{2\pi\varepsilon\varepsilon_0}{\ln(4t/d)} \approx 0.2\ \mathrm{pF/cm}, \qquad \text{Equation 7-5}$$

where ε_0 is the electric constant, $\varepsilon \approx 2.45$ the average dielectric constant of the oxide and vacuum.

First we examine the expected behavior for a perfectly ballistic (zero scattering) nanotube FET, in order to examine some of the qualitative behavior expected at high bias. We calculate the current using some assumptions and simplifications: (1) The nanotube is undoped (intrinsic semiconductor). (2) The electrode Fermi level is aligned with the middle of the nanotube gap. (3) The subbands are approximated by a hyperbolic band structure (as Equation 1-4 in Chapter 1):

$$E(k) - (-e)V_{\mathrm{NT}}(x) = \mp\sqrt{(\hbar v_{\mathrm{F,m}} k)^2 + (\nu\Delta)^2}, \qquad \text{Equation 7-6}$$

where the upper (lower) sign is for the valence (conduction) bands, $V_{\mathrm{NT}}(x)$ is the potential of the nanotube at position x, k is the wave vector, $v_{\mathrm{F,m}} = 9.35 \times 10^7$ cm/s is the Fermi velocity of metallic nanotubes, $\nu = 1$ for first subbands, $\nu = 2$ for second subbands, and Δ is half nanotube bandgap. (4) The device capacitance is dominated by capacitance to the gate since the channel length is fairly long compared with gate oxide thickness, and the charge density

$$q(x) = \pm n(x)e = c_{\mathrm{g,e}}(V_{\mathrm{NT}}(x) - V_{\mathrm{g}}) \qquad \text{Equation 7-7}$$

is determined locally, where

$$n(x) = 4\int dk(f(E(k_>) - \mu_s) + f(E(k_<) - \mu_d)) \qquad \text{Equation 7-8}$$

is the carrier density (the 4 from spin and subband degeneracies), $k_>$ ($k_<$) means k is in the range of $k > 0$ ($k < 0$), and μ_s (μ_d) is the chemical potential of source (drain) contact. (5) Zero temperature. (I believe that the temperature is not critical to the high-bias transport cases; the carriers should be very energetic.) (6) Contact resistance is neglected; i.e. the SBs at the contacts are transparent once the bias across the SBs exceeds one-half the band gap. The quasi-Fermi level of the right (left) moving carriers matches the Fermi level of the left (right) metal contact. The last two assumptions are reasonable for describing transport at biases greatly exceeding the SB height and the temperature. V_{NT} and n at the contacts are determined by satisfying the assumption (3), (4), (6) and bias conditions self-consistently. The current is then calculated by

$$I = \mp 4e\int dk(f(E(k_>) - \mu_s) + f(E(k_<) - \mu_d))v(k), \qquad \text{Equation 7-9}$$

where $v(k)$ is described in Equation 7-1 (in one dimension). Here, only the lowest conduction bands or highest valence bands are considered to contribute to the current conduction.

The result of the ballistic model for holes as majority carriers is plotted in Figure 7-3(b). At low drain bias, the conductance is $\frac{4e^2}{h}$ = 155 μS, which is the signature of a perfectly ballistic SWNT [130]. Interestingly, this quantized conductance persists only over a small range of bias and gate voltages. At high positive drain bias, the current increases more slowly, with near-constant slope

$\frac{c_{g,e}}{c_{g,e}+c_q}\frac{4e^2}{h} \approx 17$ μS, where $c_q = e^2D(E)$ is the quantum capacitance, with $D(E)$ the energy-dependent density of states. Except for Fermi energies very near the band edge [60] c_q is well approximated by the quantum capacitance of a metallic SWNT $c_{q,m} = 8e^2/hv_{F,m} \approx 3.31$ pF/cm. (In the ballistic case, only the right-moving branch of the conduction band is filled, and $c_q = c_{q,m}/2 \approx 1.65$ pF/cm.) The crossover from $G = \frac{4e^2}{h}$ to $G = \frac{c_{g,e}}{c_{g,e}+c_q}\frac{4e^2}{h}$ occurs once all the available holes in the valence band are moving toward the source at the Fermi velocity. At this point, further increase in the current can only come through increase in the hole density, which is limited by the voltage difference between gate and drain.

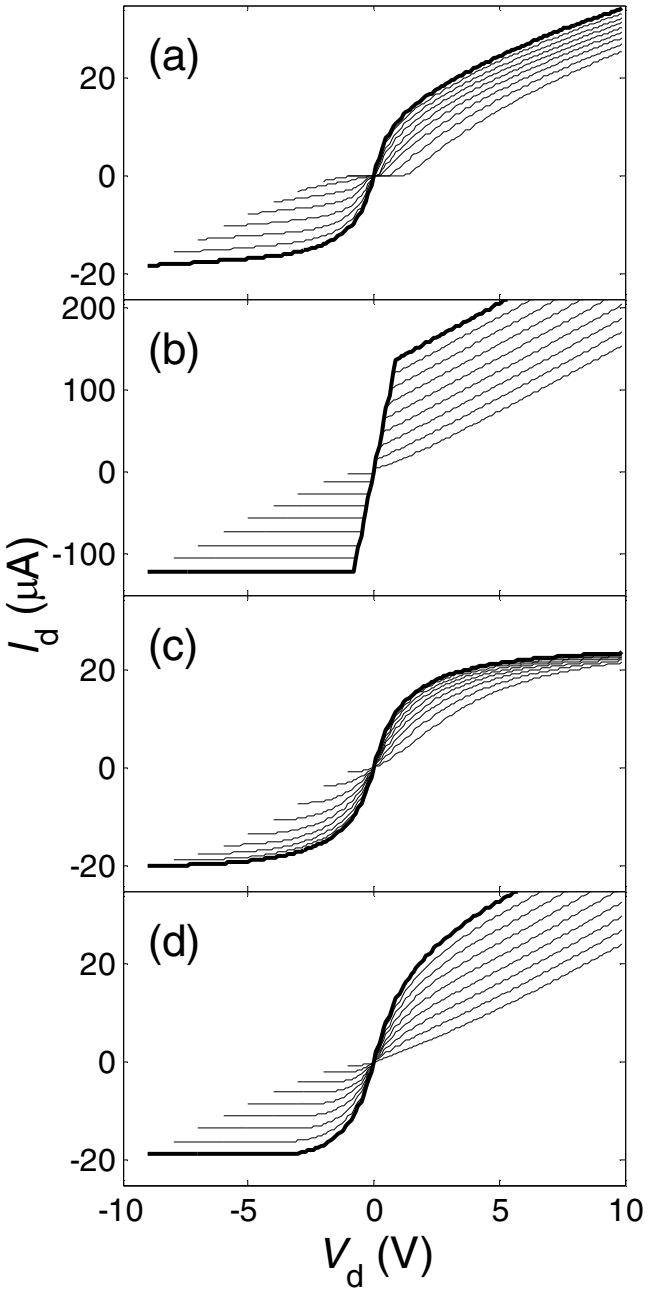

Figure 7-3. Comparison between experimental data and simulation for several models with holes as majority carriers. (a) Experimental I_d as a function of V_d at V_g from -9 V to -1 V, in 1 V steps. The thick curve is for V_g = -9 V. (b) Ballistic model (c) current saturation model, and (d) velocity saturation model are plotted for the same gate voltages as the experimental data. Note the different vertical scale for (b).

At negative high drain bias, the current saturates because no more holes are added by increasing negative drain bias, since now the amount of holes is controlled by the voltage difference between gate and source.

Figure 7-3 compares the experiment data (reproduced in Figure 7-3(a) from Figure 7-2) with the ballistic model (Figure 7-3(b)) as well as two other models discussed below. The ballistic model reproduces many of qualitative features of the experimental data in Figure 7-3(a): a high conductance region at low bias, saturation at negative bias, and current increasing roughly linearly at positive bias. Particularly the linear increase at positive bias is striking; in conventional metal-oxide-semiconductor FETs (MOSFETs) the current increases supra-linearly at positive bias. The linear increased is easily understood in terms of the nearly constant Fermi velocity in SWNTs at high E_F; further increase of the carrier energy does not increase the velocity (and the current).

Quantitative comparison between Figure 7-3(a) and Figure 7-3(b) shows that the current and conductance are significantly higher in the ballistic model than those in the experiment. This is reasonable: since the channel length is tens of microns, we do not expect ballistic transport.

We next examine two models for the field-dependent velocity in the nanotube. In the first, the current saturation model, we assume that the maximum difference in the left- and right-moving quasi-Fermi levels is set by optical phonon scattering at $hf \approx 160$ meV. The current is then limited to $4ef \approx 25$ μA as observed in metallic nanotubes [45], and as has been suggested for semiconducting nanotubes [44]. The empirical *I-V* relation

$$\frac{V}{I} = R_0 + \frac{|V|}{I_0}, \qquad \text{Equation 7-10}$$

where I_0 = 25 μA is the saturation current for metallic SWNT, was suggested in Ref. [45]. If we represent this relation in terms of mobility μ and F, we have:

$$\mu^{-1} = \mu_0^{-1} + ne\frac{|F|}{I_0}, \qquad \text{Equation 7-11}$$

where μ_0 is the zero-field mobility and n is the carrier density.

Again using the assumptions above with the average quasi-Fermi level of the carriers in the nanotube near the nanotube/metal junctions matching the Fermi level of the metal contacts, we calculate the current

$$I = q(x)\mu F(x), \qquad \text{Equation 7-12}$$

where $F(x) = -\nabla V_{\mathrm{NT}}(x)$ and $q(x) = c_{\mathrm{g,e}}(V_{\mathrm{NT}}(x) - V_{\mathrm{g}})$ are functions of position x. Note that the current I is constant throughout the whole channel (independent of x). The result of the current saturation model for hole conduction is shown in Figure 7-3(c), where the fitting parameters are I_0 = 25 μA and zero-field hole mobility μ_0 = 2.7×10^4 cm^2/Vs. Comparing the calculation (Figure 7-3(c)) with experiment (Figure 7-3(a)), disagreement is seen in several aspects. First, rather than saturating at 25 μA at high positive drain bias, the measured current increases with roughly constant slope. Second, the current at negative bias is larger than that in experiment. I_0 = 25 μA was chosen assuming only the first valence subbands participate in the conduction and the physics is similar to metallic SWNT; however, no choice of I_0 gives a good fit. Specifically, I_0 = 50 μA, which might correspond to two contributing subbands, is significantly worse.

The qualitative agreement of the ballistic model with the measured current suggests that the charge-controlled model of the nanotube transistor, namely $I_d \propto q$, is correct. However, the charges must not move with Fermi velocity, but somewhat slower. In conventional semiconductors, typically the electric-field-dependent carrier velocity is observed to saturate to a constant value at high electric field. Empirically, the carrier mobility often follows Equation 7-3, which means at low E-field regime, the carrier velocity v increases linearly with E-field with slope μ_0; at high E-field, v saturates at v_s. Perebeinos, *et al.* have calculated the electron-phonon interaction within a tight binding model and derived the μ-F relation for a single electron [131], and Equation 7-3 fits their result very well [131]. The calculation of current under the velocity-saturation model is the same as that in the ballistic model except $v = \mu F$, μ is described by Equation 7-3, and the pinch-off effect is included. Pinch-off happens because the carrier velocity is limited at v_s. To maintain constant current in nanotube, the channel needs finite amount of charge even when V_d approaches V_g. (The pinch-off effect will be discussed more in the next section.) We include the pinch-off effect in velocity saturation model as follows: when we calculate I_d vs. negative V_d, the magnitude of current eventually starts to decrease as V_d is beyond a threshold voltage $V_{d,th}$; i.e. the maximum of I_d, $I_{d,max}$, occurs at $V_{d,th}$. The current is fixed at $I_{d,max}$ when V_d is greater than $V_{d,th}$. The same procedure is applied to the source when V_d is positive.

The I-V curves of the velocity-saturation model for hole conduction are plotted in Figure 7-3(d), where the fitting parameters are hole saturation velocity $v_s = 2 \times 10^7$ cm/s and zero field hole mobility $\mu_0 = 2.7 \times 10^4$ cm^2/Vs. Simply speaking, μ_0

is determined by fitting the current at low drain bias; v_s is determined by fitting the current at high negative drain bias. The unipolar majority-electron bias regime (V_g larger than both V_d and V_s) is very similar to the majority-hole regime, indicating symmetric conduction and valence band structure. By a similar analysis, we find the electron saturation velocity is also ~ 2×10^7 cm/s. Directly comparing compared the results of modeling (ballistic, current saturation, and velocity saturation) with the experimental data in Figure 7-3, and we find the best agreement with the velocity-saturation model. Also, the reason the currents in s-SWNTs can be higher than 25 μA is that no matter how many the carriers are, all of them move with ~ 2×10^7 cm/s in high electric fields. This also indicates that higher-order subbands participate the carrier transport.

In order to compare the models more quantitatively, we plot in Figure 7-4 the saturation current I_{sat} at different V_g for the experimental data and the current-saturation and velocity-saturation models. Also included is a calculation carried out for a constant hole mobility of 5000 cm^2/Vs (the I_d-V_d curves are shown in Figure 7-5). Figure 7-4 shows that the experimental behavior fits the velocity-saturation model very well - the velocity-saturation model predicts linear I_{sat} vs. V_g, as seen in the data. The current-saturation model always produces sublinear I_{sat} vs. V_g, while the constant-mobility model has $I_{sat} \sim V_g^2$ similar to conventional long channel MOSFETs [92]. Note that it is probable that an even better fit in Figure 7-4 might have been obtained for slightly different fitting parameters; the calculations are time consuming, so this has not been done.

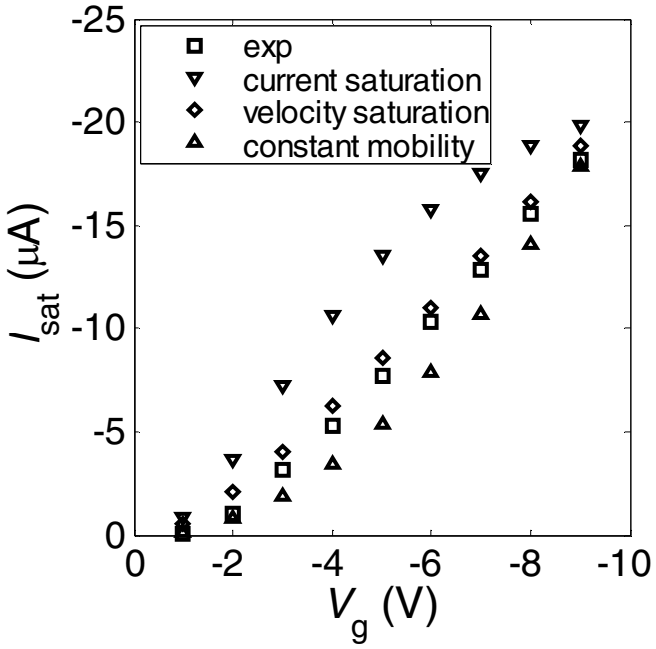

Figure 7-4. Saturation current I_{sat} at different V_g for experimental data and theoretical models discussed in text. I_{sat} is I_d at $V_d = V_g$.

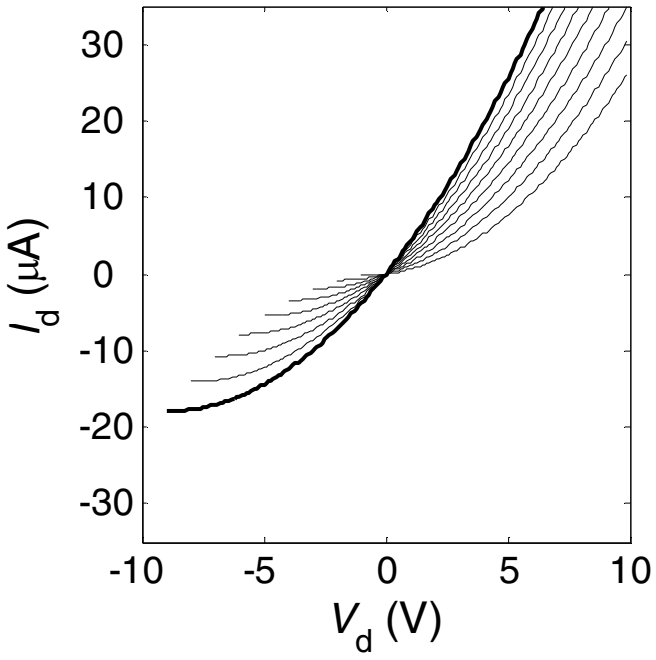

Figure 7-5. I_d as a function of V_d of constant-mobility model at V_g from -9 V to -1 V, in 1 V steps. The thick curve is for V_g = -9 V.

The saturation velocity is smaller than the peak carrier velocity of 4.5×10^7 cm/s calculated in Ref. [132] for a 2.4 nm diameter nanotube at an electric field of ~ 5 kV/cm, and 5×10^7 cm/s in Ref. [131] using a one-electron model, but is still more than twice as high as in silicon inversion layers [133]. The one-electron model is good for low carrier density cases. However, in the device operation regime, the carrier density is high (~ 10^9 cm^{-1}). The measured saturation velocity is lower than the calculated saturation velocity suggests increasing carrier density may reduce the saturation velocity. In Chapter 8, I will discuss how the saturation velocity should decrease with carrier density increase.

Though a simple model of velocity saturation describes the experimental data surprisingly well, some problems remain. First, contact effects are not considered, which causes poor agreement around $V_d = 0$ and $V_g = 0$. In Chapter 10, I will investigate the contact effects of s-SWNT-FETs. Second, the experimental current at high positive drain bias does not increase as fast as expected, indicating that v_s may decrease slightly with increasing charge density. The phenomenological Equation 7-3 fits the one electron case fairly well [131]. However, it is not at all clear whether their results extrapolated to many electrons would give current saturation or velocity saturation (since these are identical in a one-electron model). In Chapter 8, I will explore the carrier behavior in s-SWNTs under the considerations of electron-phonon interactions.

7.4 Carrier-Density and Potential Profiles in Velocity-Saturation Model

In the previous section I modeled a s-SWNT device and found the best agreement with the velocity-saturation model, with a saturation velocity v_s of 2×10^7 cm/s. Here I would like to discuss more details about the charge distribution and potential profile along the nanotube channel in the velocity-saturation model.

Plugging Equation 7-3 into Equation 7-2, the carrier velocity as function of F in the velocity-saturation model is obtained:

$$v = \mu_0 F \frac{v_s}{v_s + \mu_0 |F|} = v_s \frac{F}{\frac{v_s}{\mu_0} + |F|} . \qquad \text{Equation 7-13}$$

When $F >> v_s/\mu_0$, v approaches v_s; When $F << v_s/\mu_0$, $v \approx \mu_0 F$.

Figure 7-6 shows an example of the profiles of band structure, carrier density, and carrier velocity of a s-SWNT channel at V_d = -1 V, V_g = -9 V. The average electric field is about 0.05 V/μm = 0.5 kV/cm, which is smaller than v_s/μ_0 = 0.74 kV/cm. The overall channel has fairly uniform carrier density due to the potential difference from source to drain is small. The potential drop (F), and therefore the carrier velocity, are not varying much as well.

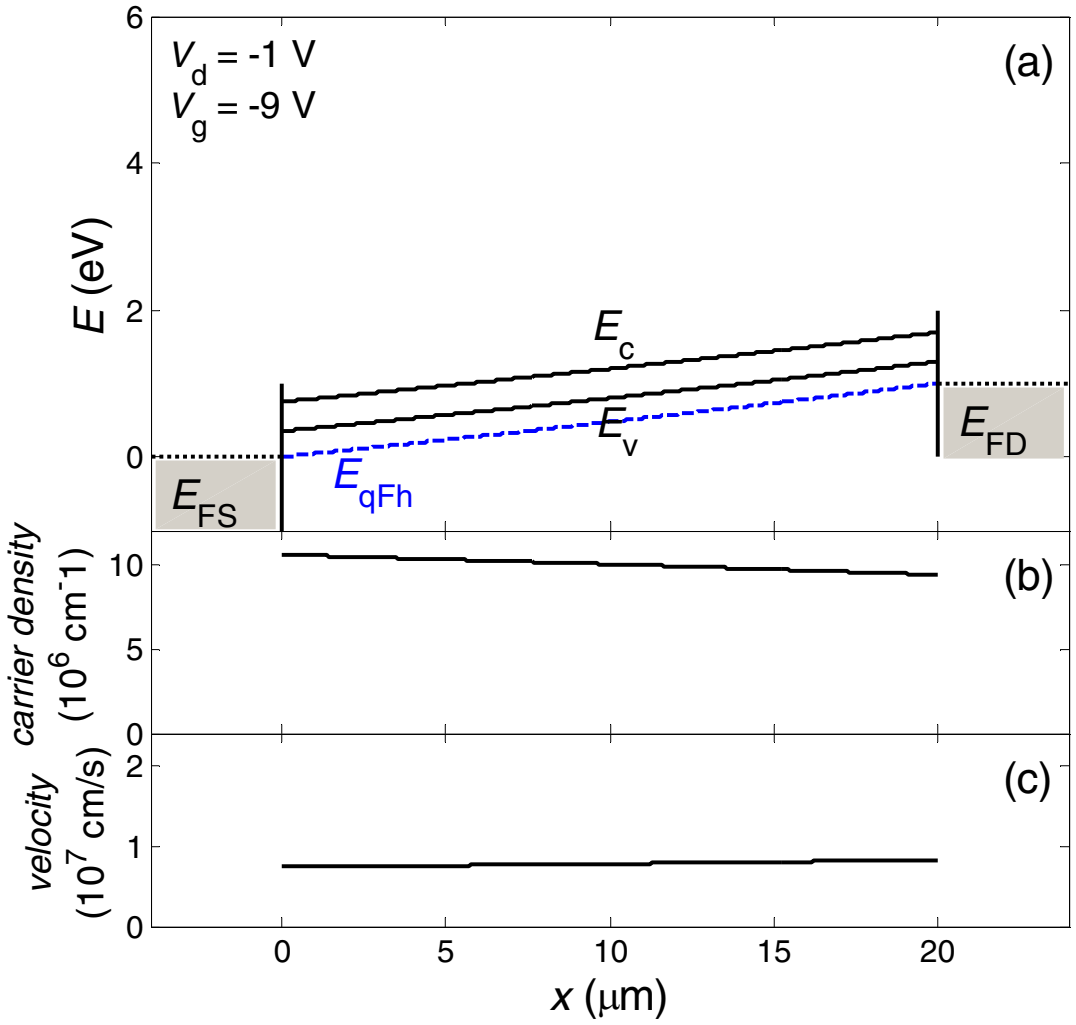

Figure 7-6. Profiles of (a) band structure, (b) carrier density, and (c) carrier velocity in a s-SWNT channel without pinch-off happening (V_d = -1 V, V_g = -9 V).

Figure 7-7 shows another example of the profiles at V_d = -5 V, V_g = -9 V. The overall potential gradient is higher than the previous example because the magnitude of applied V_d is larger. The average electric field is about 0.25 kV/cm, which is larger than v_s/μ_0. The carrier density and the carrier velocity show pronounced variation along the nanotube channel, by almost a factor of two. The trends of the carrier density and the carrier velocity are inverted because the current is constant through the whole channel. Near the drain contact the carrier density can not go lower

because the carrier velocity in the velocity-saturation model is limited at v_s no matter how we increase F; the carrier density is fixed and the potential is set correspondingly. That means the carriers in the nanotube near the drain contact are very away from equilibrium with the carriers in the drain contact; pinch-off happens. The carriers near the drain contact move with the speed close to saturation velocity v_s.

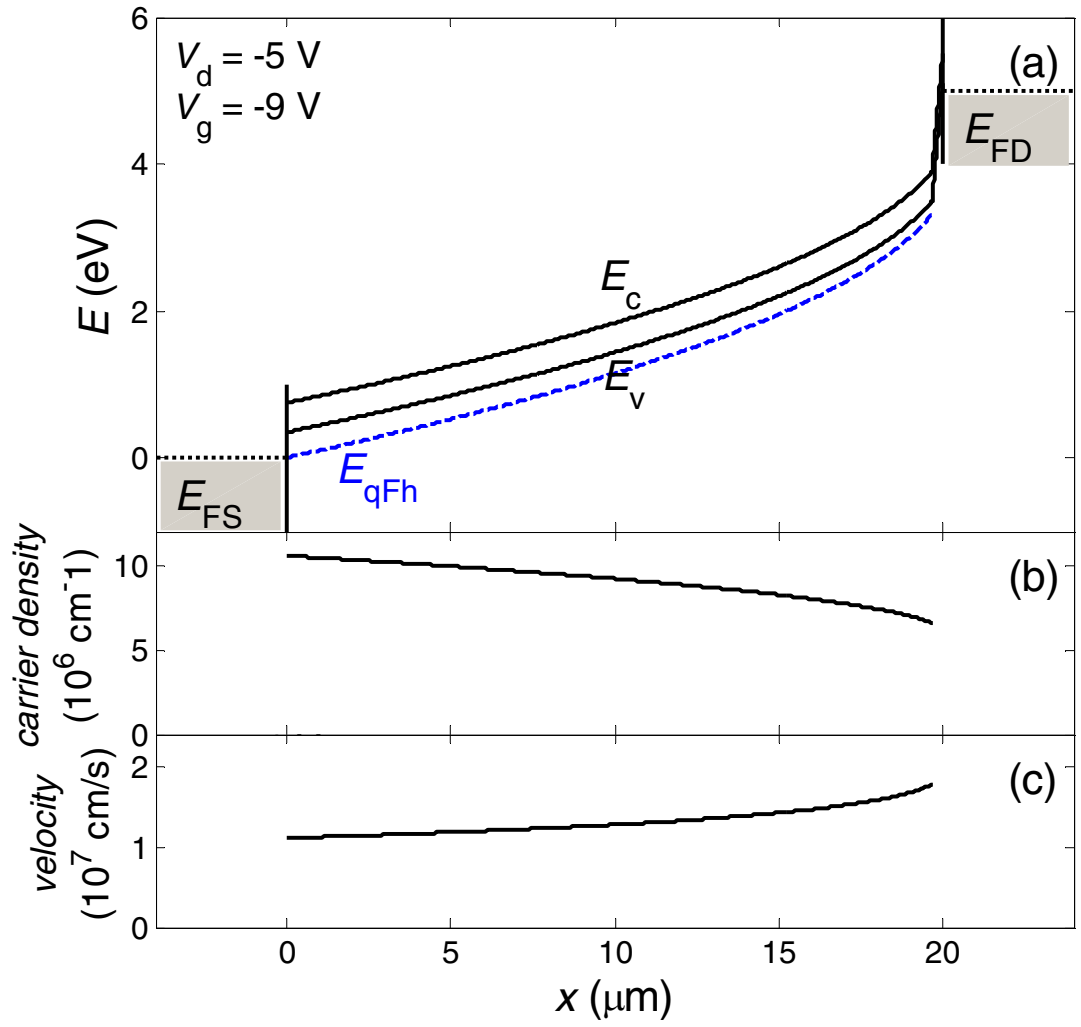

Figure 7-7. Profiles of (a) band structure, (b) carrier density, and (c) carrier velocity in a s-SWNT channel with pinch-off happening (V_d = -5 V, V_g = -9 V).

The discussions above are for hole conduction. Due to electron-hole symmetry of SWNTs, the electron conduction acts in the same manner.

Chapter 8

Electron-Phonon Interactions in Semiconducting SWNTs

8.1 Overviews of Electron-Phonon Interactions in SWNTs

When electrons travel in a crystal material, they usually suffer scatterings so that they lose their phase information, momentums or energies. There are several major scattering sources in solid state systems, such as defects, impurities, lattice vibrations (phonons). In CNTs, especially SWNTs, which are quasi-one-dimensional materials, scattering happens in a special manner. Only forward and backward scattering are available, which largely reduce the scattering probability and make CNTs very good charge conductors. Phase information of traveling electrons, which produces quantum phenomena, is usually lost easily in a very short range, and I will not discuss it here. It is known that CVD growth methods produce nanotubes largely free of defects and impurities [55,134]; in one study, high-quality CVD-grown SWNTs were confirmed to contain one defect per 4 μm on average [134]. Therefore, electron-phonon interactions causing relaxation of electron energies and/or momenta consume many researchers' efforts in order to understand electronic transport properties in CNTs.

Yao *et al*. have first studied current saturation of 25 μA at high bias voltages in m-SWNTs and successfully explained the phenomenon in terms of scattering of electrons due to optical or zone-boundary phonon emission [45]. The mean free path of nearly elastic acoustic phonon scattering l_{ac} is ~ 300 nm, and the mean free path of optical phonon emission backscattering l_{op} is ~ 10 nm from the data fitting. Dai's

group [47] and McEuen's group [69] have also confirmed Yao's conclusions experimentally. Both groups have performed length dependent measurements on m-SWNTs, and extracted the mean free paths at low and high energies (Dai: l_{ac} ~ 300 nm, l_{op} ~ 15 nm; McEuen: l_{ac} ~ 1600 nm, l_{op} ~ 10 nm). The current through short (< ~ 150 nm) m-SWNTs can be significant higher than 25 μA [47,69]. Transport through very short (~ 10 nm) m-SWNTs is free of significant phonon scattering and thus ballistic and quasiballistic at the low- and high-bias voltage limits, respectively [47].

Electron-phonon scattering in s-SWNTs has also been studied, at least theoretically. Pennington *et al*. have studied electron-phonon scattering in a single charge carrier picture, and found out the charge carrier drift velocity can be as high as 5×10^7 cm/s in s-SWNTs [132]. Negative differential mobility is even predicted at high electric fields [132]. Perebeinos *et al*. also used a single carrier picture in multiple subbands predicted velocity saturation behavior [131], as discussed in Chapter 7. However, it is not at all clear whether their results extrapolated to many electrons would give current saturation or velocity saturation (since these are identical in a one-electron model). The carrier density in s-SWNT-FETs usually changes according to gate capacitance and voltages. Therefore I would like to discuss the numerical study I have done on carrier velocities under the influences of phonon scatterings in s-SWNTs in different carrier density regimes.

8.2 Numerical Study of Carrier Velocities in s-SWNTs Concerning Electron-Phonon Scatterings in a Single Subband

In solid state systems, the nonequilibrium distribution function g is used to describe the dynamics of the charge carriers (both electrons and holes). In carbon

nanotubes which are one-dimensional materials, the number of electrons in the n-th subband at time t in a phase space volume dxdk at point (x, k) is $2g_{\mathrm{n}}(x, k, t)\mathrm{d}x\mathrm{d}k/2\pi$ [135], where two is from the spin degeneracy of electrons. In equilibrium, g is given by the Fermi distribution:

$$g_{\mathrm{n}}(x,k,t) = f(E_{\mathrm{n}}(k)) = \frac{1}{e^{(E_{\mathrm{n}}(k)-\mu)/k_{\mathrm{B}}T}+1}, \qquad \text{Equation 8-1}$$

where $E_{\mathrm{n}}(k)$ is the universal energy dispersion of the n-th subband, k_{B} is Boltzmann constant, T is the temperature. However, when an applied electric field is present, g deviates from Fermi distribution [135]. In this section, I simply consider the carriers in a single subband, so the subscript is dropped for simplicity.

The dynamics of g is governed by Boltzmann equation:

$$v(k)\frac{\partial g(x,k,t)}{\partial x}+\frac{eF}{\hbar}\frac{\partial g(x,k,t)}{\partial k}+\frac{\partial g(x,k,t)}{\partial t}=\left(\frac{\mathrm{d}g}{\mathrm{d}t}\right)_{\mathrm{collision}}, \qquad \text{Equation 8-2}$$

where the right side of the equation is the distribution change rate due to the collisions. In steady state, $\frac{\partial g(x,k,t)}{\partial t}=0$, and further assuming no carrier density variation along x so that $\frac{\partial g(x,k,t)}{\partial x}=0$, then

$$\frac{eF}{\hbar}\frac{\partial g(k)}{\partial k}=\left(\frac{\mathrm{d}g}{\mathrm{d}t}\right)_{\mathrm{collision}}. \qquad \text{Equation 8-3}$$

The collision term in Boltzmann equation can be simply described by relaxation lengths if there are multiple sources of scatterings:

$$\left(\frac{\mathrm{d}g}{\mathrm{d}t}\right)_{\mathrm{collision}}=\sum_{\mathrm{s},k'}\frac{v(k)}{l_{\mathrm{s}}}((1-g(k))g(k')-g(k)(1-g(k'))), \qquad \text{Equation 8-4}$$

where the first term in right side of Equation 8-4 denotes the carriers scattering in to state k from state k', while second term denotes the carriers scattering out from state k to state k', and s stands for different types of scatterings. Here I approximate the electron-phonon scattering into two categories: nearly elastic scattering mainly with low energy acoustic phonons and strongly inelastic scattering mainly with optical phonons or zone-boundary phonons; the scattering strengths are characterized by l_{ac} and l_{op}, respectively. Figure 8-1 shows approximate electron-phonon scatterings in a single band. The filled and empty circles indicate the states which are occupied and empty, respectively. The arrows indicate some possible scattering transitions. The arrow 1 indicates an elastic electron-phonon scattering, while the arrow 2 and 3 indicate inelastic electron-phonon scatterings. Because the optical phonon energies and zone-boundary phonon energies are all about 160 meV with small dispersion, the emission energy of phonons required by inelastic electron-phonon scatterings is simply set at 160 meV (phonon absorption is not considered because the population of phonons of 160 meV is very small at room temperature). The transitions 1 and 2 toward empty states are permitted; however, the transition 3 toward filled states is prohibited simply because of the exclusion principle.

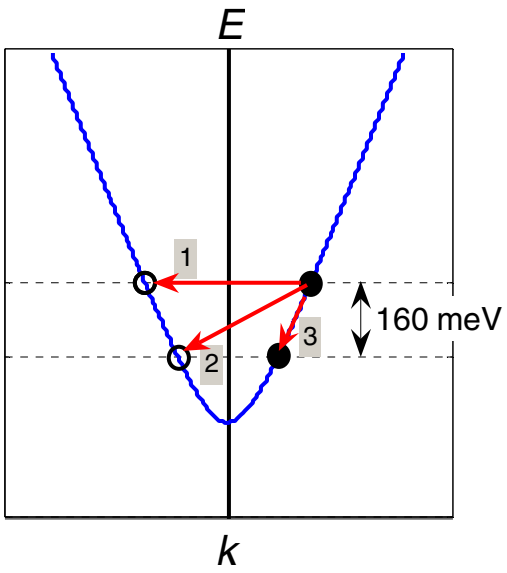

Figure 8-1. Approximate electron-phonon scatterings in a single band. The filled and empty circles indicate the states which are occupied and empty, respectively. The arrows indicate some possible scatterings. The scatterings toward empty states are permitted; however, the scatterings toward filled states are prohibited simply because exclusion principle.

By solving Equation 8-3, the nonequilibrium distribution function $g(k)$ corresponding to each F is obtained. Figure 8-2 shows $g(k)$ at three different F. Note that the dashed curve represents the Fermi distribution at T = 300 K, which is symmetric with respect to $k = 0$. Under F the distribution has higher weight in one k direction than in the opposite, which causes a nonzero average carrier velocity (drift velocity); therefore nonzero current. When F gets higher, the asymmetry gets more pronounced. $g(k)$ has a sharp decline at the point where the corresponding energy of the state is about 160 meV when F is high. This occurs because once carriers have the energies higher than 160 meV, they start to emit phonons and relax to lower energy states.

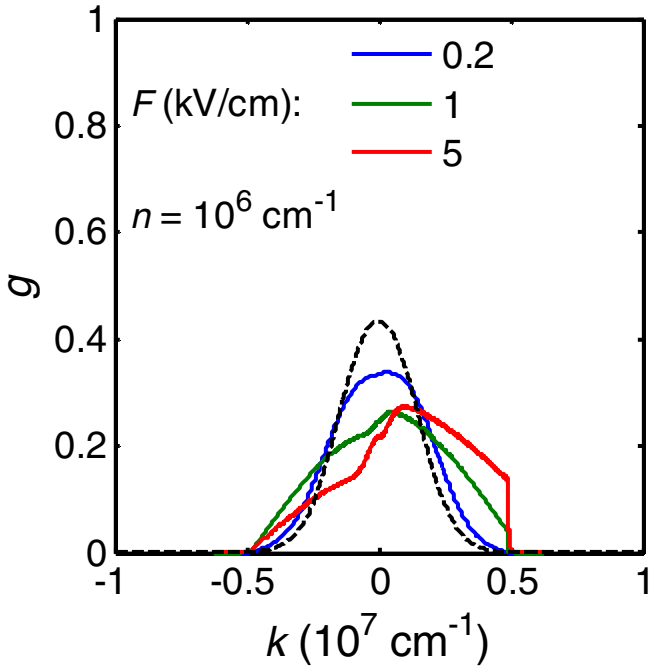

Figure 8-2. Nonequilibrium distribution function $g(k)$ under different F. The dashed curve represents the Fermi distribution at T = 300 K. The bandgap of the universal dispersion relation used in this calculation is 0.4 eV.

After obtaining $g(k)$ and then evaluating the average carrier velocity (drift velocity)

$$v = \frac{\sum_k g(k)v(k)}{\sum_k g(k)} \qquad \text{Equation 8-5}$$

at many different F, the v-F relationship can be determined.

First, motivated by experiments in m-SWNTs [45,47,69], we choose values for the numerical calculation of l_{ac} = 300 nm and l_{op} = 10 nm. Figure 8-3 shows average carrier velocity (drift velocity) v as a function of applied electric field F at different carrier density n with density increasing exponentially from 10^3 cm^{-1} to 10^7 cm^{-1} in $10^{0.5}$ cm^{-1} steps. Note that a carrier density of 10^3 cm^{-1} is identical to one carrier in a 10 μm nanotube. The curves with low carrier densities collapse to a

single curve line with velocity-saturation like behavior. Similar velocity-saturation behavior for a single carrier picture in multi-subbands was predicted by the group [131].

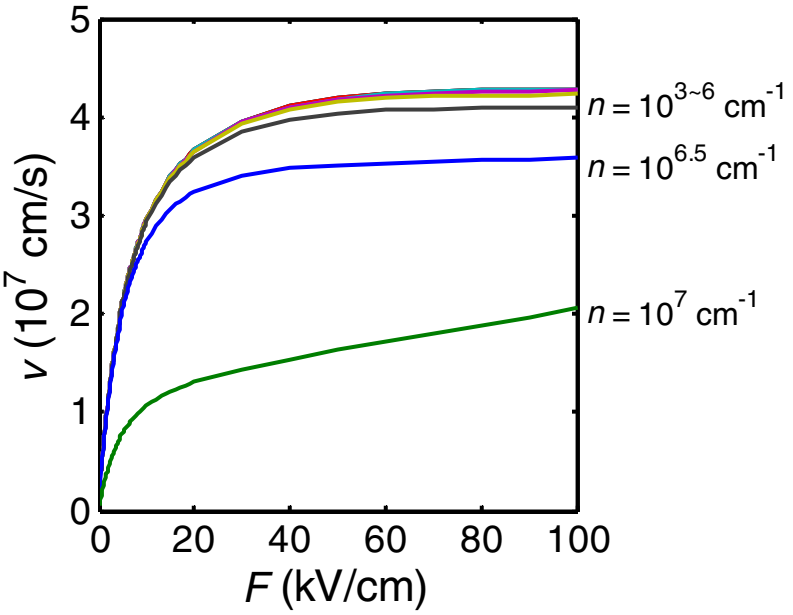

Figure 8-3. v vs. F at different carrier densities with density increasing exponentially from 10^3 cm^{-1} to 10^7 cm^{-1} in $10^{0.5}$ cm^{-1} steps. The curves with low carrier densities collapse to a single curve line with velocity-saturation like behavior. As the density greater than threshold density ~ 10^6 cm^{-1}, the velocity decreases with increasing the density. l_{ac} and l_{op} used for this calculation are 300 and 10 nm, respectively.

Figure 8-4 compares the numerical results to the phenomenological equation of velocity saturation, Equation 7-3, which is also suggested in [131]. The blue star points in Figure 8-4 represent the same numerical calculation data of the curve for n = 10^6 cm^{-1} in Figure 8-3. The red dashed curve is the fit using Equation 7-3. They agree with each other fairly well with the fitting parameters $\mu_0 = 8.2 \times 10^3$ cm^2/Vs and $v_s = 4.5 \times 10^7$ cm/s, obtained by least-squares fitting. Here we see the velocity-

saturation behavior is preserved in the numerical calculations even at finite carrier densities. However, as the density increases beyond a threshold density ~ 10^6 cm^{-1}, the velocity decreases with increasing density.

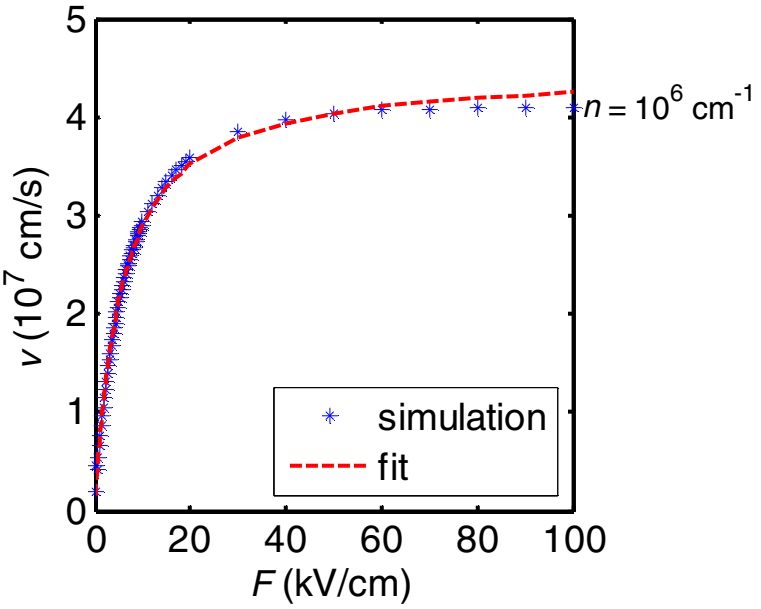

Figure 8-4. Fitting the calculation result of v vs. F by phenomenological equation of velocity saturation.

Figure 8-5 shows v as a function of F at different carrier densities with density increasing linearly from 10^6 cm^{-1} to 10^7 cm^{-1} in 10^6 cm^{-1} steps. The scattering lengths used here are the same as those in Figure 8-3. Although the velocity still seems to saturate at high F, the saturation velocity decreases monotonically with increasing density.

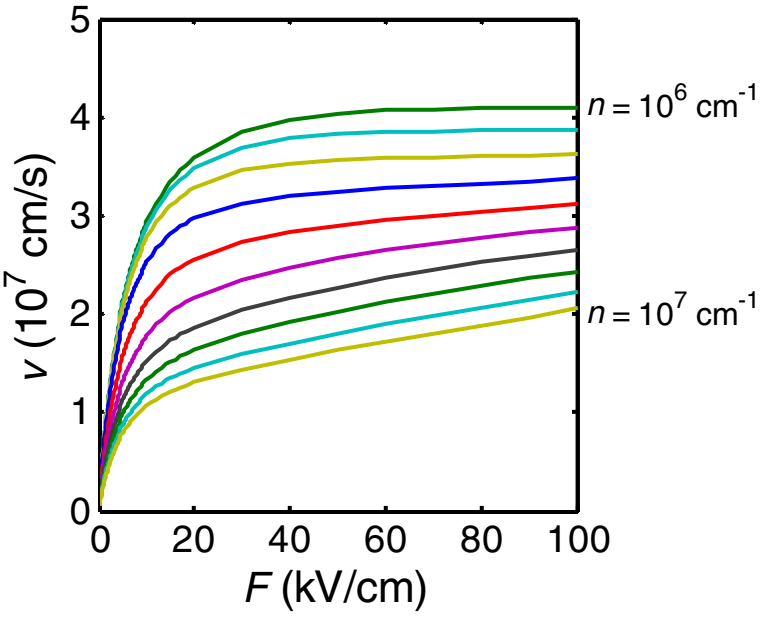

Figure 8-5. v vs. F at different carrier densities with density increasing linearly from 10^6 cm^{-1} to 10^7 cm^{-1} in 10^6 cm^{-1} steps. At high electric fields the velocity decreases with increasing the density. l_{ac} and l_{op} used for this calculation are 300 and 10 nm, respectively.

The blue star points in Figure 8-6 shows v at F = 100 kV/cm as a function of carrier density n (a) in logarithmic scale from the data in Figure 8-3, and (b) in linear scale from the data in Figure 8-5. The trend of the saturation velocity with respect to the carrier density is easily noticed. As discussed previously, the saturation velocity does not vary with the carrier density at low carrier densities, but falls nearly linearly at high carrier densities. If Equation 7-4 and current saturation were obeyed, we would expect the saturation velocity to be inversely proportional to carrier density. This is a reasonable expectation when considering only a single valence and conduction subband (excluding inter-subband scattering) and very strong optical phonon scattering; here one might expect the current to saturate 25 μA at high electric fields, once the difference between quasi-Fermi levels for left- and right-moving

carriers is 160 meV. The red dashed lines in Figure 8-6 indicate the *v*-*n* relation corresponding to a current of 25 μA. That the calculated (blue star) points are higher than the red dashed lines at high carrier densities and electric fields implies the current is higher than 25 μA. Therefore, in our model, it is possible that the current can exceed 25 μA in s-SWNTs even though phonon emissions are strong and inter-subband scattering is neglected.

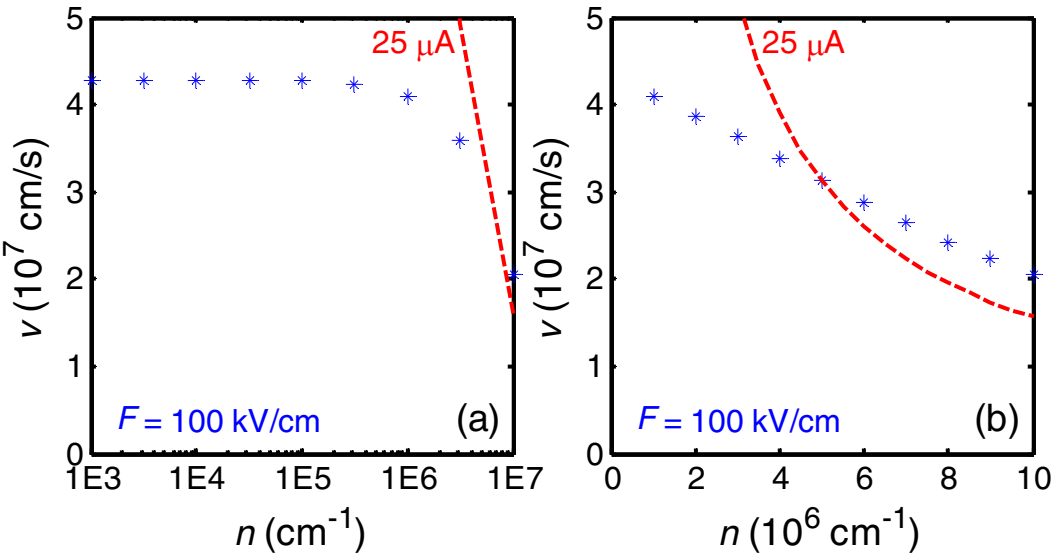

Figure 8-6. *v* at *F* = 100 kV/cm as a function of carrier density *n* (a) in logarithmic scale and (b) in linear scale. The red dashed lines indicate the *v*-*n* relation corresponding to a current of 25 μA.

Now I would like to explore the effects of varying l_{ac} and l_{op} in the relations of *v*-*F*. Figure 8-7 shows *v* as a function of *F* similar to Figure 8-3, but with scattering lengths l_{ac} = 150 nm and l_{op} = 10 nm. The general qualitative behaviors of velocity saturation in Figure 8-7 and Figure 8-3 are the same. The quantitative difference is that the low field mobility is smaller when l_{ac} is shorter. l_{ac} affects low *F* transport

more because elastic scatterings do not need high carrier energies to activate. When l_{op} is varied (see Figure 8-8 with scattering lengths l_{ac} = 300 nm and l_{op} = 5 nm), the qualitative behavior (velocity saturation) is in general not changed as well; however, at high F the saturation velocity increases and the saturation behavior become better when l_{op} gets shorter. l_{op} affects high F transport more because inelastic phonon emissions only happen when carriers have high energies. Also, at high F the saturation velocity *increases* when l_{op} gets shorter because once carriers have energy to emit phonons, they emit right away and relax to low energy states, which have small velocity; in the other words, there are very few carriers at states with velocities in the opposite direction of average carrier velocity. The fitting parameters $\mu_0 = 8.2 \times 10^3$ cm^2/Vs and $v_s = 4.5 \times 10^7$ cm/s in Figure 8-4 are a little off from $\mu_0 = 2.7 \times 10^4$ cm^2/Vs and $v_s = 2 \times 10^7$ cm/s of experimental results. The variance of μ_0 suggests that l_{ac} is longer than 300 nm in the experimental sample discussed in Chapters 6 and 7. This is not surprising; low-field mobility is expected to a strong function of diameter [132,136], and also likely varies depending on processing conditions. The discrepancy of v_s I believe is mostly due to the fact that the carrier density is 10^6 cm^{-1} in Figure 8-4, but order of 10^7 cm^{-1} in the experiments described in Chapter 7, hence the carrier-density-dependence of the velocity should be taken into account to better understand the data.

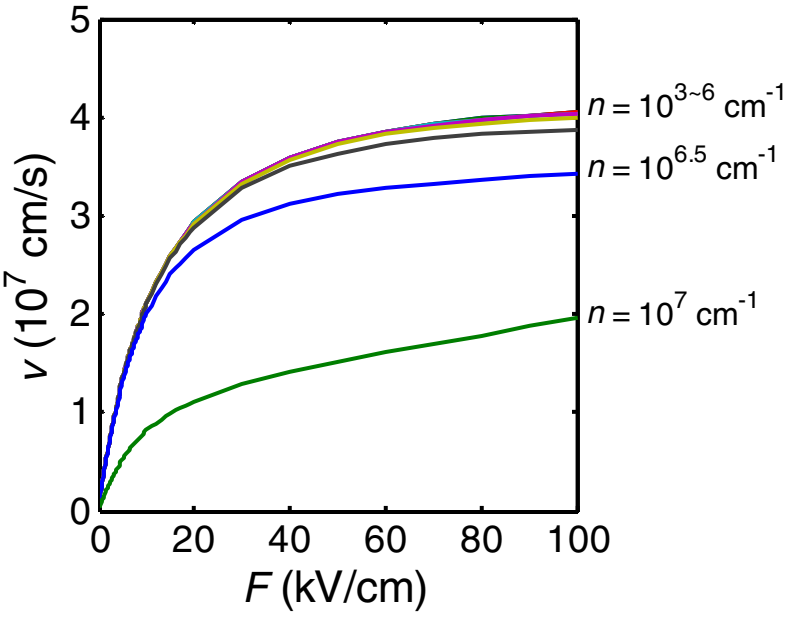

Figure 8-7. v vs. F at different carrier densities with density increasing exponentially from 10^3 cm^{-1} to 10^7 cm^{-1} in $10^{0.5}$ cm^{-1} steps. l_{ac} andl_{op} used for this calculation are 150 and 10 nm, respectively.

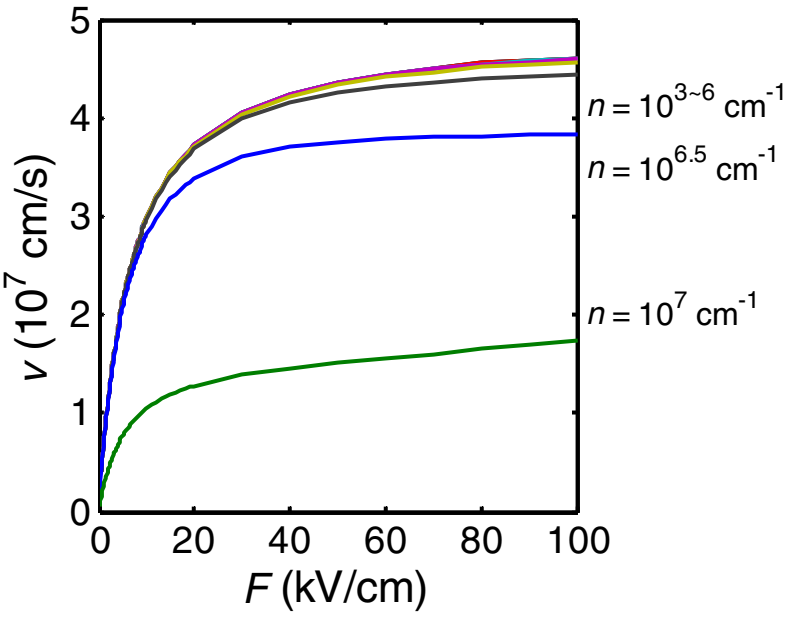

Figure 8-8. v vs. F at different carrier densities with density increasing exponentially from 10^3 cm^{-1} to 10^7 cm^{-1} in $10^{0.5}$ cm^{-1} steps. l_{ac} and l_{op} used for this calculation are 300 and 5 nm, respectively.

I have considered expanding my numerical study to the multi-subband case. However, while I was working on this subject, IBM group published their results on it [137]. They have calculated the mobility in s-SWNTs as a function of carrier density and electric field, for different tube diameters and temperatures. They have found that at a critical density, n_c about 3.5 to 5.0 $\times$ 10^6 cm^{-1}, the average carrier velocity saturates at about one-third of the Fermi velocity of graphene. Below n_c, the velocity reaches a maximum and then experiences negative differential mobility with increasing field. Above n_c, the velocity increases with field strength with no apparent saturation, which is also seen in my numerical calculation for the lowest conduction band or highest valence band transport. It is interesting that my simple model produces many features of the more detailed calculations of [137]; this indicates that I have indeed captured the essential physics of scattering in s-SWNTs in my model.

Theorists have predicted negative differential conductance or negative differential mobility in s-SWNTs at high-bias transport [131,132], which is not shown in my numerical study. One of the reasons is that for simplicity of my study the electronic dispersion relation is approximated by universal dispersion relation [18], where the carrier velocity is asymptotically approach to the Fermi velocity of graphene as energy increases (see Equation 1-4). However, the real electronic band structures flattens at very high energies. Figure 8-9 show the comparison between the universal dispersion relation and a more accurate dispersion relation derived by tight

binding calculation and zone folding method for (7, 0) s-SWNT. We see that the universal dispersion relation is a very good approximation to the tight binding calculation, but yet there is still some small discrepancy between them. The universal dispersion relation has non-negative curvature; the dispersion relation derived by tight binding calculation and zone folding method shows negative curvature. Therefore, as more and more carriers have very high energies, the average velocity decreases, causing negative differential conductance or negative differential mobility. Another possible reason is that my calculation restricts at single subband, no band edges of higher subbands are available; however they are available in multi-subband calculation.

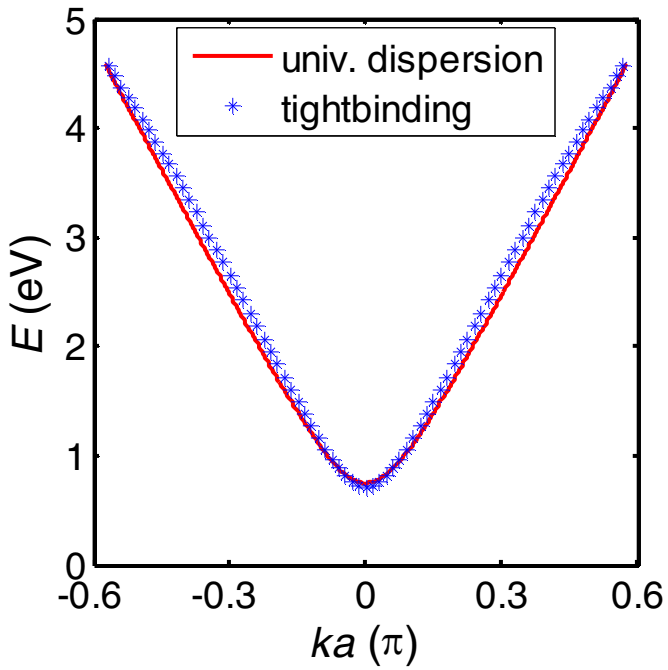

Figure 8-9. Comparison between the universal dispersion relation and the dispersion relation derived by tightbinding calculation and zone folding method for (7, 0) SWNT.

Recently Pop *et al*. [138] have experimentally observed negative differential conductance in freely suspended SWNTs (both m-SWNTs and s-SWNTs) but not in those lying on substrates. But here the reason is not simply because of the negative curvature of the bands, but rather because of significant self-heating effects including electron scattering by hot nonequilibrium optical phonons [138,139]; there is no thermoconductivity through the substrates in freely suspended SWNT devices. Lazzeri *et al*. [139] predict an effective temperature for optical phonons of thousands of Kelvins. Hot phonon scatterings thus can reveal more about high bias transport in SWNTs.

Chapter 9

High-Bias Transport of Semiconducting SWNTs in the Ambipolar Regime

9.1 Introduction and Experimental Results

Semiconducting SWNTs have almost identical conduction and valence bands near the Fermi level as described in Chapter 1. It is possible to inject electrons and holes from the contacts into the s-SWNT at same time if the applied bias to the s-SWNT is larger than the bandgap of the s-SWNT [46,49,128]. Electrons are injected from one contact into the s-SWNT and holes are injected from the other [46,49,128]. When electrons and holes meet in the channel, they recombine rapidly due to strong Coulomb interaction between them [92,135,140]. Part of the energy they carry will be relaxed during the recombination. It is possible to emit light (photons) because the s-SWNT bandgap is direct, and the momentum of a photon is small, which conserves the momentum in the process. The process is usually referred as "light recombination". IBM research group have demonstrated optical emission in infrared range induced electrically from s-SWNT devices [49,127,129]. Sometimes recombination relaxes energy in other ways, such as phonons. It is called as "dark recombination". The efficiency of the radiative recombination has been found to be quite low; about 10^{-6} to 10^{-7} photons per electron-hole pairs [141] for the devices with substrates. More recently, it was found that the partially suspended nanotubes exhibit

an increase of 2 to 3 orders of magnitude from the nanotubes with substrates [142], resulting the efficiency about 10^{-3} to 10^{-4}.

Sometimes the recombination involves three charged particles, two electrons plus one hole or one electron plus two holes; the electron-hole pair annihilates and gives its energy to the additional particle. Such a process is called Auger recombination. Although the probability for three particles to meet is smaller than for two particle processes, Auger recombination is still sometimes favorable because the energy and the momentum are conserved easily.

Above discussions are all based on an independent charge picture, where charges do not interact with each other. However, one electron and one hole in s-SWNTs have been predicted to bind together to form an exciton due to Coulomb interaction [143-147], which lower the total electronic energy of the system. When excitons are involved in the recombination, two particles participate in Auger recombination: one excition plus one free charge, or two excitons. The exciton energy is large (order of 100 meV in s-SWNTs) due to nanotube's 1D nature, which severely modulate the light emission spectrum away from the energy gap [148,149]. The evidence of exciton existence in s-SWNTs is found in femtosecond transient absorbtion optical spectroscopy measurements [150] and suggested in fluorescence spectroscopy experiments [148,151].

In Chapter 6, I have briefly described that we are able to inject both electrons and holes into a s-SWNT when applying $V_d < V_g < V_s$ (for injecting electrons from drain and holes from source) or $V_d > V_g > V_s$ (for injecting electrons from source and holes from drain). In this chapter I would like to provide another evidence of

electron-hole recombination indeed happens in s-SWNTs by transport measurement and device modeling.

Figure 9-1(a) shows I_d as a function of V_g at V_d = -1 V from the device whose unipolar data are described in Chapter 7. This device behaves as an ambipolar semiconductor although p-type (hole) conduction is slightly better than n-type (electron) conduction. Because of the ambipolar behavior, we assume the presence of SBs at the electrodes for electrons and holes, but a smaller SB for holes. The maximum transconductances g_m for holes and electrons are ~ 2.5 and 2.0 μA/V, respectively, which correspond to field-effect mobilities [28] $\mu_{FE} \approx 2.5 \times 10^4$ and 2.0 $\times$ 10^4 cm^2/Vs (here we have used the electrostatic gate capacitance per length $c_{g,e} \approx 2\pi\varepsilon\varepsilon_0 / \ln(4t/d) \approx 0.2$ pF/cm where ε_0 is the electric constant, $\varepsilon \approx 2.45$ the average dielectric constant of the oxide and vacuum). (The field effect mobility μ_{FE} is slightly smaller than the zero-field mobility $\mu_0 = 2.7 \times 10^4$ cm^2/Vs determined using the data in the range -0.1 V < V_d < 0.1 V discussed in Chapter 7, due to finite V_d = -1 V used here.) The on-state conductances $G \approx$ 13 and 7 μS for hole and electron indicate mean-free-paths $l = LG/2G_0$ of at least 1.6 and 0.9 μm. These values are comparable to the highest measured values for SWNTs [28] though contact resistance due to SBs may play a significant role in this case. In fact, large V_d and large voltage difference between gate and the contacts are needed such that the SBs are thinning enough to be transparent for charges to tunnel through. Figure 9-1(b) shows I_d as a function of V_g at V_d = 20 mV, illustrating p-conduction is much better than n-conduction at relatively low drain biases due to the high and thick SBs for n-conduction. The maximum hole transconductance is ~ 0.1 μA/V, which corresponds

to $\mu_{FE} \approx 5 \times 10^4$ cm^2/Vs. The on-state $G \approx 20$ μS indicates a mean-free-path l at least 2.5 μm. (μ_{FE} and G derived from Figure 9-1(b) is larger because V_d is smaller and the temperature is lower; presumably fewer scatterings happen in this measurement.)

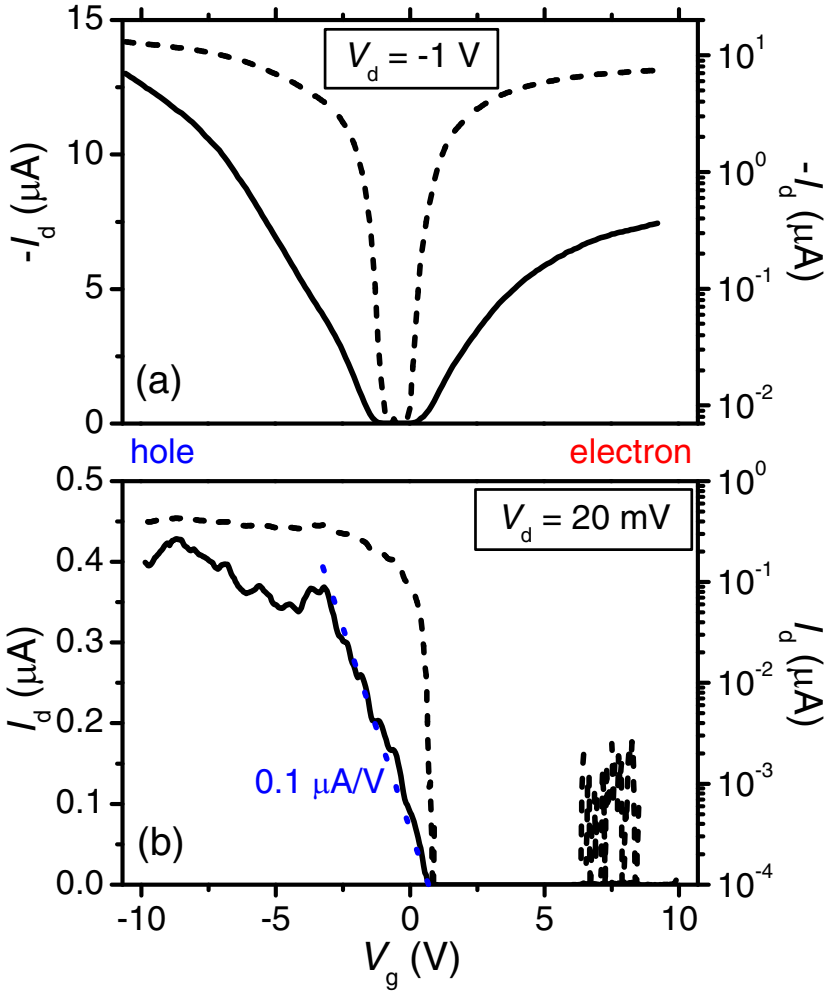

Figure 9-1. Drain current I_d as a function of gate voltage V_g (a) at drain voltage V_d = -1 V and temperature T = 4.2 K, and (b) at V_d = 20 mV and T = 1.5 K. The solid and dashed lines correspond to linear (left) and logarithmic (right) scales, respectively. The dotted line in (b) corresponds to a transconductance of 0.1 mA/V.

Figure 9-2(a) shows I_d vs. V_g at different V_d. Here, as usual, the gate voltage is measured relative to the grounded source electrode. Figure 9-2(b) shows the same data plotted with the gate voltage measured relative to the drain electrode. In each case we subtract from V_g the value V_{off} = 0.7 V in order to make Figure 9-2(a) and Figure 9-2(b) appear symmetric under reversal of the horizontal axis. They are symmetric because the source and the drain contacts are identical; they are called source or drain contact only according to where the ground and the bias are applied respectively. We interpret V_{off} as the gate voltage at which the center of the nanotube is charge-neutral; it is non-zero due to the work function difference of the nanotube with respect to the Si substrate and metal electrodes, and likely also includes contributions from charges in the dielectric [29] and/or doping of the nanotube by adsorbates [8]. We define $V_g' \equiv V_g - V_{off}$. In Figure 9-2, the currents in the ambipolar region are shown by solid lines, while the currents in the unipolar regions are shown by dashed lines. As noted in Chapter 6, the minimum current appears at $V_g' = V_d/2$, which is clearly seen in Figure 9-2. Also, the curves with high V_d collapse into a curve at negative $V_g' - V_s$ in Figure 9-2(a) and at positive $V_g' - V_d$ in Figure 9-2(b) because the current saturation due to pinch-off effect in unipolar range described in Chapter 7 and strong electron-hole recombination, which will be described next.

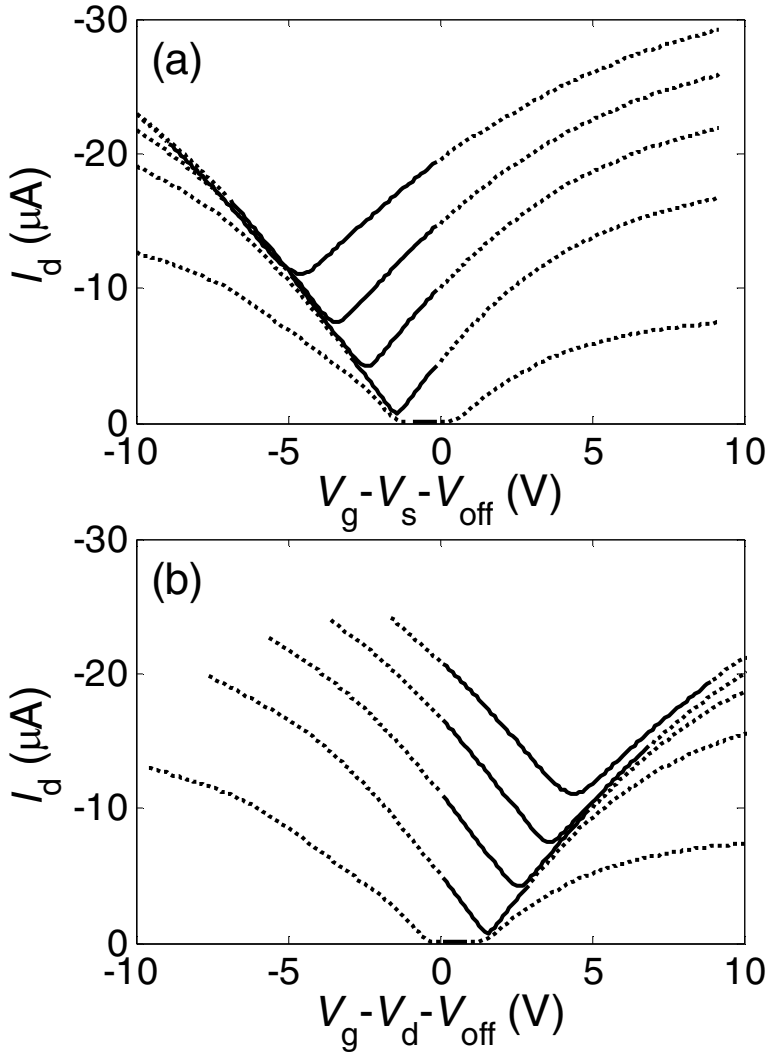

Figure 9-2. Drain current I_d as a function of gate voltage V_g at drain voltages V_d from -1 V to -9 V, in -2 V steps. Temperature is 4.2 K. The gate voltage in (a) is measured relative to the grounded source electrode, while (b) shows the same data plotted with the gate voltage measured relative to the drain electrode. In each case we subtract from V_g the value $V_{off} = 0.7$ V. The currents in ambipolar regions are shown by solid lines, while the currents in ambipolar regions are shown by dashed lines.

It is notable that the gap in conduction between unipolar electron conduction and unipolar hole conduction at low bias (e.g. $V_d = -1$ V in Figure 9-2) is significantly larger than the bandgap (~ 350 meV for this sample). I assume that this is due to the SB contacts, which do not conduct until a finite bias is applied across them. I model

this with a parameter V_c; the contacts are opaque for biases less than V_c , and once the bias across the contact exceeds V_c, the contacts are considered to be transparent. When both $|V_g' - V_d|$ and $|V_g' - V_s|$ are smaller than the threshold voltage V_c to overcome the SB, both hole current I_h (the left branches) and electron current I_e (the right branches) are in the off state or in the subthreshold region (remember $V_s = 0$ all the time). When $V_g' - V_d$ (or $V_g' - V_s$) is smaller than $-V_c$ the hole current starts to flow in the linear region, and likewise for the electron current when $V_g' - V_s > V_c$ (or $V_g' - V_d > V_c$). Once $|V_d| > 2V_c$, there is no longer a conduction gap because at least one of the hole current (I_h) and electron current (I_e) is in the linear region, but a conduction dip with minimum at $V_g' = V_d/2$ instead, where $I_h = I_e$. (From Figure 9-2, V_c is estimated about 1.3 V.) The data suggests that the total current through the device $I_d \neq I_h + I_e$ but rather $I_d = \max(I_h, I_e)$ indicating nearly complete recombination of electrons and holes. This is consistent with recent reports [127,141,152] demonstrating that holes and electrons efficiently recombine in the nanotube radiatively or irradiatively. Photoexcited carrier lifetimes in nanotubes attributed to interband carrier recombination are reported [152] to be 5 ~ 20 ps, much shorter than the carrier transit time in our device of ~ 100 ps, which is the channel length L divided by the carrier saturation velocity.

The discussion above helps us to understand the device behaviors in ambipolar regions only very qualitatively. A more dedicated device modeling like that described in Chapter 7 is needed to have a more complete understanding of the devices operated in ambipolar regions.

9.2 Device Modeling

The modeling device geometry is described in Chapter 7, with L = 20 μm, d = 2.4 nm, and t = 500 nm, to match the geometry of the device whose transfer characteristics are shown in Figure 9-1 and Figure 9-2. Also as customary, V_d and V_g are applied to the drain and the gate, respectively, and the source is grounded ($V_s = 0$). The contact effects are entirely neglected in the modeling; we assume that at large V_d and large voltage difference between gate and the contacts the SBs are thinned enough to be transparent for charges to tunnel through easily. The contact effects will be further addressed in Chapter 10.

Considering there are both electrons and holes existing in the channel, the charge density (charge per unit length) contributed by electrons and holes are

$$q_e(x) = -en_e(x) \text{ and}$$

$$q_h(x) = en_h(x) \qquad \text{Equation 9-1}$$

respectively, where $n_e(x)$ and $n_h(x)$ are the electron and hole carrier densities, respectively. (Note that electrons have negative charges.) The total charge density

$$q(x) = q_e(x) + q_h(x) = c_{g,e}(V_{NT}(x) - V_g). \qquad \text{Equation 9-2}$$

The electron and hole flow rates are

$$J_e(x) = n_e(x)\mu(-F(x)) \text{ and}$$

$$J_h(x) = n_h(x)\mu F(x), \qquad \text{Equation 9-3}$$

where $F(x) = -\nabla V_{NT}(x)$. (Note that electrons move opposite to the direction of $F(x)$.) Here I use the result from velocity-saturation model illustrated in Chapter 7 and 8 to the carrier velocity under the influence of $F(x)$:

$$\mu(x) = \frac{\mu_0 v_s}{v_s + \mu_0 \left| F(x) \right|} \qquad \text{Equation 9-4}$$

(the same as Equation 7-3 and Equation 7-13). The total current is also contributed by electron and hole currents

$$I = I_{\mathrm{e}}(x) + I_{\mathrm{h}}(x)\,, \qquad \text{Equation 9-5}$$

where

$$I_{\mathrm{e}}(x) = -eJ_{\mathrm{e}}(x) = en_{\mathrm{e}}(x)\mu F(x) \text{ and}$$

$$I_{\mathrm{h}}(x) = eJ_{\mathrm{h}}(x) = en_{\mathrm{h}}(x)\mu F(x)\,. \qquad \text{Equation 9-6}$$

(In our device definition, the current I_{d} flowing from drain to source is measured, which is toward the negative direction in our device modeling; therefore $I_{\mathrm{d}} = -I$.)

In the absence of recombination, carrier continuity in steady state gives

$$\frac{\partial J_{\mathrm{e}}(x)}{\partial x} = \frac{\partial J_{\mathrm{h}}(x)}{\partial x} = 0\,. \qquad \text{Equation 9-7}$$

However, if electron-hole recombination is considered, then

$$\frac{\partial J_{\mathrm{e}}(x)}{\partial x} = \left(\frac{\mathrm{d}n_{\mathrm{e}}}{\mathrm{d}t}\right)_{\text{recombination}} \text{ and}$$

$$\frac{\partial J_{\mathrm{h}}(x)}{\partial x} = \left(\frac{\mathrm{d}n_{\mathrm{h}}}{\mathrm{d}t}\right)_{\text{recombination}} \qquad \text{Equation 9-8}$$

where $\left(\frac{\mathrm{d}n_{\mathrm{e}}}{\mathrm{d}t}\right)_{\text{recombination}}$ and $\left(\frac{\mathrm{d}n_{\mathrm{h}}}{\mathrm{d}t}\right)_{\text{recombination}}$ are the electron and hole density change rates due to recombination, respectively. If the independent charge picture is applied and a single recombination process involves one electron and one hole, then electron and hole density change rates equal the recombination rate:

$$\left(\frac{\mathrm{d}n_{\mathrm{e}}}{\mathrm{d}t}\right)_{\text{recombination}} = \left(\frac{\mathrm{d}n_{\mathrm{h}}}{\mathrm{d}t}\right)_{\text{recombination}} = -k(n_{\mathrm{e}}(x)n_{\mathrm{h}}(x) - {n_{\mathrm{i}}}^2), \qquad \text{Equation 9-9}$$

where k is the recombination constant, and n_{i} is the intrinsic carrier density which only depends on temperature. The carrier density change rates due to recombination are negative because the carriers disappear when they recombine.

Putting all these things together with the average quasi-Fermi level of the carriers in the nanotube near the nanotube/metal junctions matching the Fermi level of the metal contacts, the current are evaluated in ambipolar bias conditions. Figure 9-3(b) shows the calculated currents in different ambipolar bias conditions with parameters $v_{\mathrm{s}} = 2 \times 10^7$ cm/s, $\mu_0 = 2.7 \times 10^4$ cm^2/Vs, $k = 5 \times 10^6$ cm^2/s and $n_{\mathrm{i}} = 10^4$ cm^{-1}. The calculated currents in Figure 9-3(b) reproduce many features of measured results in Figure 9-2: (1) as we expected from the discussion and the measured result in previous section, there is a current minimum for each V_{d} at the symmetric bias ($V_{\mathrm{g}} = V_{\mathrm{d}}/2$); (2) the current increases roughly linearly after away from the symmetric bias; (3) the displacement between each curve is nearly the same. (1) results from electron-hole recombination, while (2) and (3) result from the charge carriers having velocity-saturation behavior.

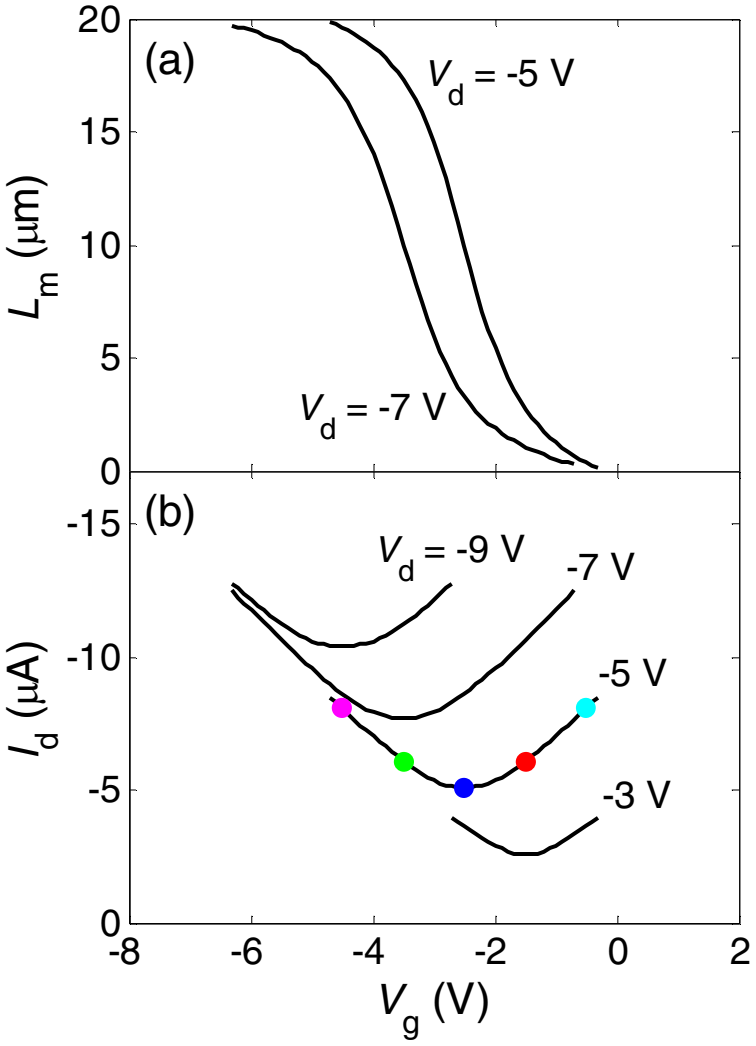

Figure 9-3. Calculated (a) position of the strong recombination and (b) current as a function of V_g.

Figure 9-4 shows the calculated (a) potential profiles, (b) recombination rate profiles, and (c) electron current and hole current profiles of a s-SWNT device along channel position x, which give more details to understand the device (the parameters are all the same as those used in Figure 9-3). Note that the colors of the curves in Figure 9-4 correspond to the biases at the points with the same color dots in Figure 9-3(b). We first look at the blue curves, which show the device is under a symmetric

bias situation (V_d = -5 V, V_g = -2.5 V). The first expression is that all blue curves are symmetric about x = 10 μm, the middle of the channel, as anticipated. At the middle of the channel, several phenomena are observed: (1) $V_{NT} = V_g$; (2) the largest potential gradient; (3) the largest recombination rate; (4) $I_e = I_h$. This is because the majority and minority carriers swap roles here, and thus the multiplication of the electron and hole densities in Equation 9-9 is the largest. Thus we observe that under a symmetric bias situation, at the middle of the channel (1) the electric field is the largest; (2) the carriers move the fastest.

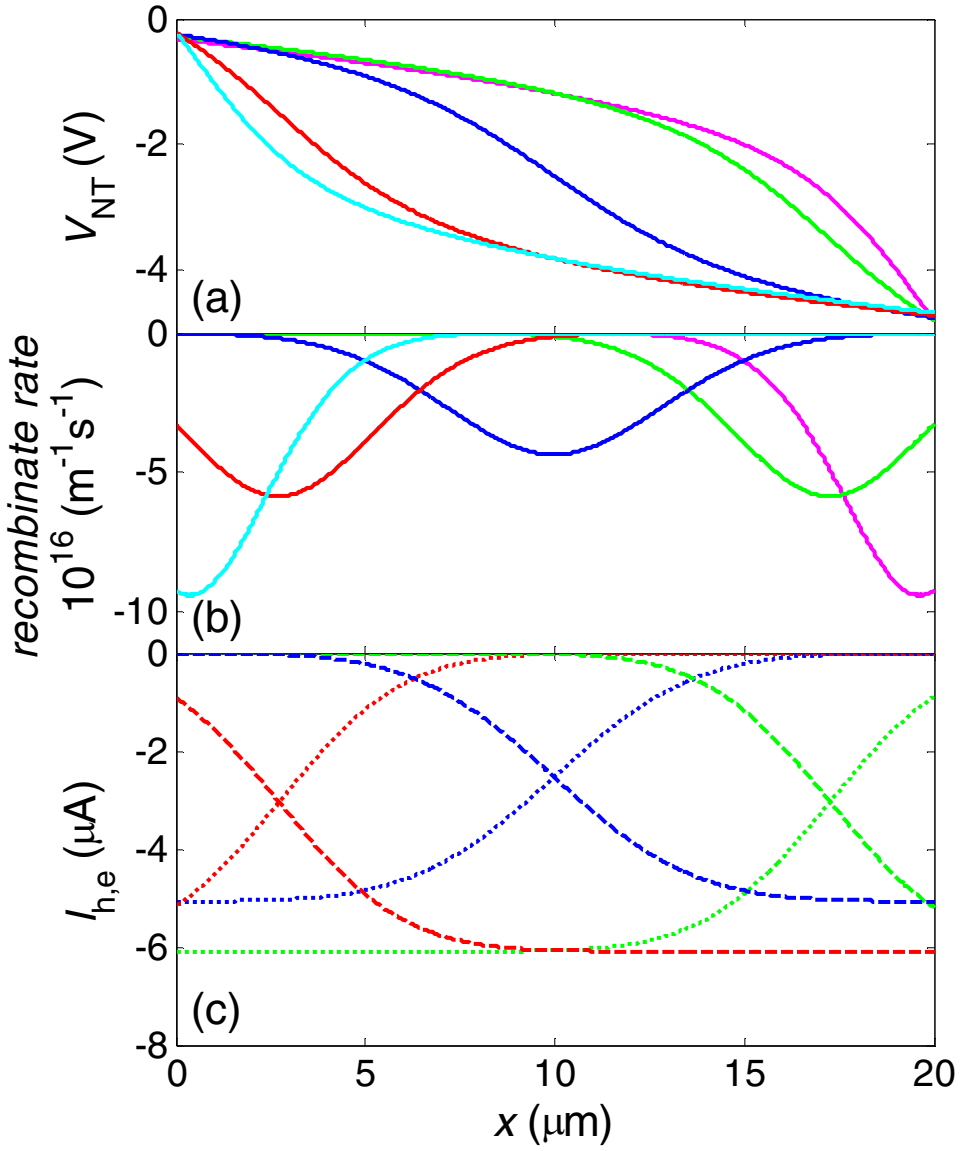

Figure 9-4. Profiles of a s-SWNT device along channel position x. (a) Potential. (b) Recombination rate. (c) Electron current and hole current. V_d = -5 V are all the case. Different colors indicate different gate bias (cyan, red, blue, green, and magenta indicate V_g = -0.5 V, -1.5 V, -2.5 V, -3.5 V, and -4.5 V, respectively). In (c), the dashed and dotted lines represent electron and hole currents, respectively. Note that the blue lines shows a symmetric bias case ($V_g = V_d/2$).

When V_g is tuned, the position of the symmetric axis shifts. The red (V_d = -5 V, V_g = -1.5 V) curves in Figure 9-4 indicate V_g is tuned toward V_s, and thus the

symmetric axis shifts toward source contact. Similar results are shown in the cyan curves, while reverse results are shown in the green and magenta curves, where V_g is tuned toward V_d and the symmetric axis shifts towards the drain. Figure 9-3(a) shows how fast the position of the symmetric axis (L_m) shifts as a function of V_g. It moves relatively fast around the symmetric V_g bias, and slows down away from the symmetric V_g bias. Figure 9-3 matches the electroluminescence experiments in Ref [153], in which the position of localized light emission from a s-SWNT was measured, very well. Also, the recombination range expected from Figure 9-4(b) is about several μm, which is the same order of the electroluminescence light spot due to electron-hole recombination [49].

Calculated band diagrams of a s-SWNT device are plotted in Figure 9-5 to summarize the results from the modeling. Figure 9-5(a) shows a band diagram with a symmetric bias (V_d = -5 V, V_g = -2.5 V) while Figure 9-5(b) shows a band diagram away from the symmetric bias (V_d = -5 V, V_g = -1.5 V). The arrows are symbols of electron-hole recombination, and in the regions marked by dashed ellipses strong recombination happens.

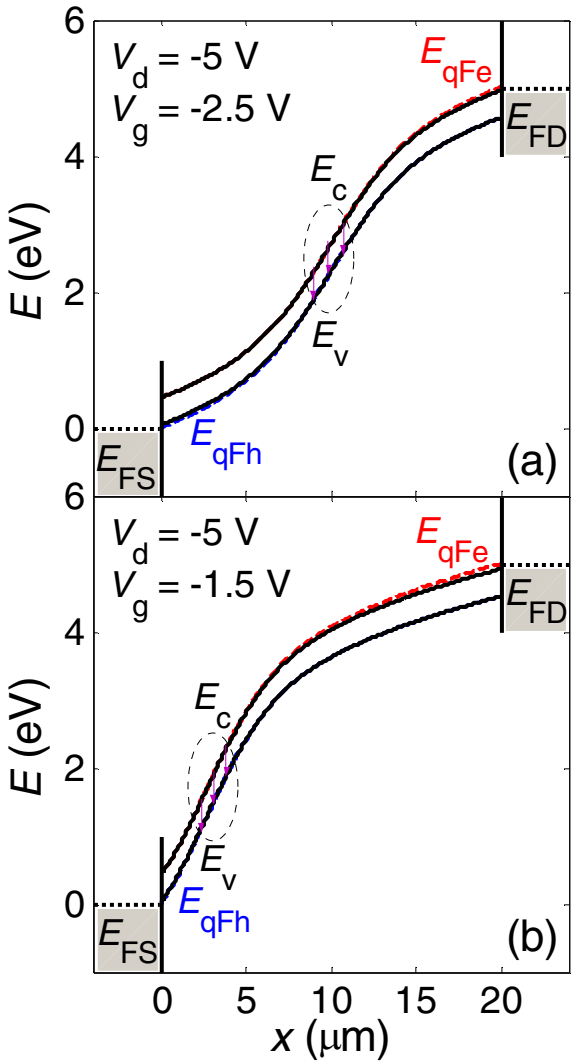

Figure 9-5. Calculated band diagrams of a s-SWNT device at (a) V_d = -5 V, V_g = -2.5 V (symmetric bias) and (b) V_d = -5 V, V_g = -1.5 V. The arrows are symbols of electron-hole recombination, and in the regions marked by ellipses strong recombination happens.

I have also tried the modeling with three-independent-charge Auger recombination, whose recombination rate is proportional to

$$n_e^2(x)n_h(x) + n_e(x)n_h^2(x) = (n_e(x) + n_h(x))n_e(x)n_h(x). \qquad \text{Equation 9-10}$$

The results of the modeling are similar to those of two-independent-charge recombination. The main reason for that is $n_e(x)$ + $n_h(x)$ varies only very slightly

through the whole nanotube since the current is identical and the carrier velocity is always close to saturation velocity at large electric fields through the whole nanotube.

While I was doing the device modeling in ambipolar regimes, there were two other groups executing the same device modeling [153,154]. IBM used an infinite recombination rate, which makes the electric field infinite and produces other unphysical results at the position where $V_{NT} = V_g$. [153]. And although Guo *et al.* properly considered the recombination rate, the carrier velocity is described by a constant mobility [154], which is non-realistic at high bias regimes. Therefore, my modeling results should be more realistic than theirs.

9.3 Using EFM to Detect Electron-Hole Recombination in s-SWNTs

From the modeling of the previous section, we have found that potential slopes are larger at strong electron-hole recombination regions and that the region of largest slope shifts when V_g is altered. This indicates that electron-hole recombination can be studied indirectly by measuring the potential profile in the nanotube. One tool for this is EFM, which I have discussed already in Chapter 3. In this section I would like to show an example of how I attempted to measure the local potential of a s-SWNT device in the ambipolar regime using EFM.

Figure 9-6(a) shows an AFM image of a s-SWNT with two metal contacts. The nanotube is not visible in the height scale because the diameter is ~ 4 nm but the contact height is ~ 100 nm. Because its diameter is large, this nanotube should have a small band gap; the expected energy gap for a 4 nm s-SWNT is 210 meV. Figure 9-7 shows the transfer characteristic of this s-SWNT device. The current is somewhat larger than the current of the device in Figure 9-2. EFM is performed on this device

with different biases. Figure 9-6(b) shows an exemplary EFM image at V_{top} = -0.2 V, V_{bottom} = -2.2 V, V_g = -0.2 V and $V_{ac,tip}$ = 0.2 V. It is clearly seen that the EFM signal is increasing from the top to the bottom, which indicated that the potential is varying along the nanotube. Note that the biases in Figure 9-6(b) are equivalent to holding V_{top} = 0 and applying V_{bottom} = -2 V and V_g = 0. In the measurement I held V_g = -0.2 V and varied V_{top} and V_{bottom} at the same amount in order to minimize the voltage difference between the tip and the substrate; however, they are equivalent to holding V_{bottom} = -2 V and V_g = 0 and varying V_g.

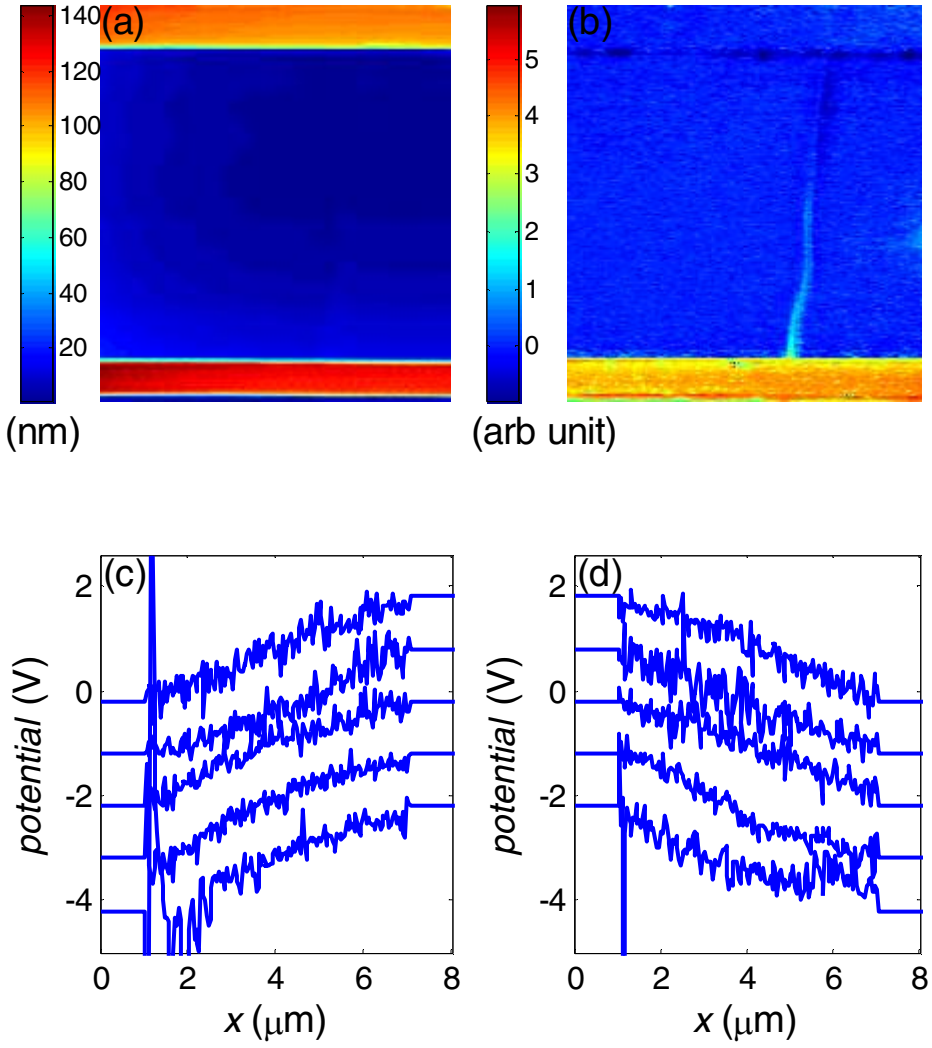

Figure 9-6. Potential profiles deducted from AC-tip-EFM images of a s-SWNT device. (a) An AFM image of a s-SWNT with two metal contacts. The scan range is $5.3 \times 8.1\ \mu m^2$. (b) An exemplary EFM image at V_{top} = -0.2 V, V_{bottom} = -2.2 V, V_g = -0.2 V. (c),(d) The potential profiles along the nanotube for different V_{top} and V_{bottom}. V_{top} and V_{bottom} of each curve are shown as flat potentials in the contact regions ($x < 0$ for the top contact and $x > 7\ \mu m$ for the bottom contact). Note that V_g = -0.2 V and $V_{ac,tip}$ = 0.2 V are hold constant.

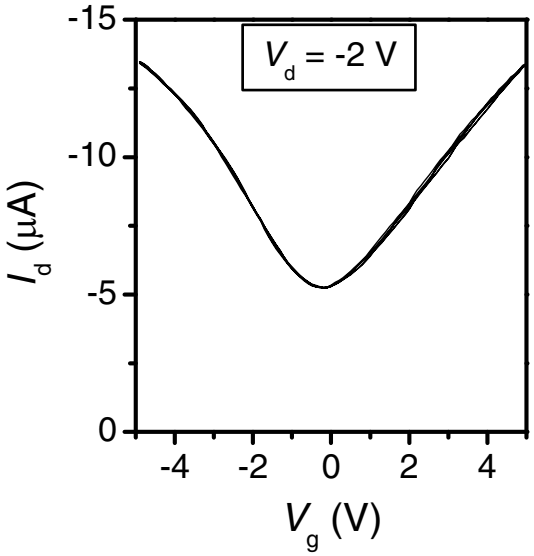

Figure 9-7. Transfer characteristic of a s-SWNT device with small band gap. The measurement was done at room temperature in vacuum (base pressure $P_b = 3.8 \times 10^{-7}$ torr).

Figure 9-6(c) and Figure 9-6(d) shows the potential profiles along the nanotube drawn from AC-tip-EFM images for different V_{top} and V_{bottom} and fixed V_g = -0.2 V. V_{top} and V_{bottom} of each curve are shown as flat potentials in the contact regions ($x < 0$ for the top contact and $x > 7\ \mu m$ for the bottom contact). The curves correspond to V_g moving from -2 V to 2 V in 1 V steps and sustaining V_{top} = -2 V and V_{bottom} = 0 (Figure 9-6(c)), or V_{top} = 0 and V_{bottom} = -2 V (Figure 9-6(d)). The potentials vary monotonically as expected, and the potential drops at the contacts are

not dominant; the nanotube is resistive. However, the large variation in potential gradient expected (see Figure 9-5) is not observed. There is no clear trend of potential variation shifts when regulating V_g. Several rounds on this device and other devices were tested, but I still failed to observe the effects shown in Figure 9-5. The most likely explanation is simply that the nanotube is not much longer than the recombination length, so the spatial variation of slope changes cannot be seen.

9.4 Indirect Proof of Electron-Hole Recombination in s-SWNTs by SGM

From the discussions in Chapter 3, we know a conducting AFM tip can serve as a local voltage variation probe, and the study of the transport responses of devices to the probe is called SGM. In this section I will discuss application of this technique to s-SWNT devices in the ambipolar transport regime to indirectly study electron-hole recombination.

Figure 9-8 shows a transfer characteristic of a s-SWNT device with d = 2.7 nm, and L ~ 6 μm. The inset shows the AFM image of the device. Again the nanotube is not visible because of the height scale. Therefore, a dashed line is used to highlight where the nanotube is. The device shows fairly symmetric electron and hole behaviors. The blue and red lines are a guide to the eye to indicate the qualitative behavior of the electron and hole currents. The double-side arrow roughly shows the V_g range where both electron and hole currents are significant. SGM of this device is operated in this range.

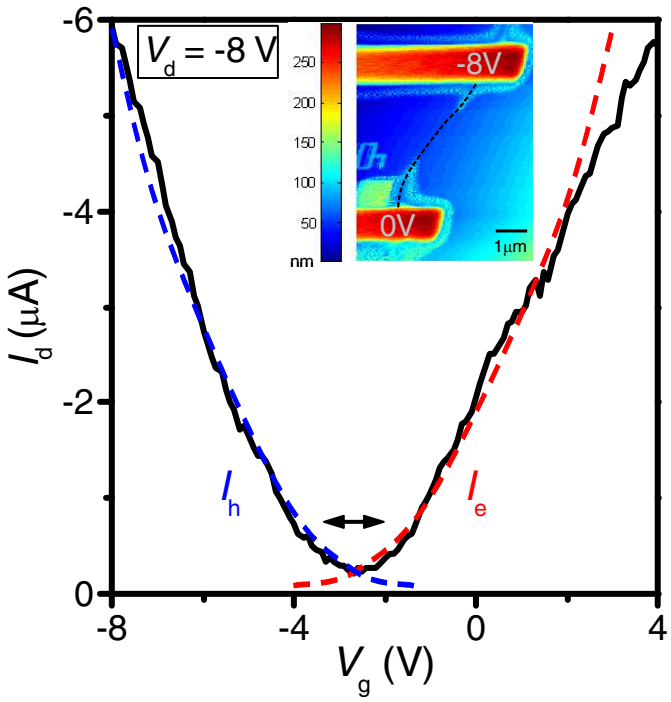

Figure 9-8. Transfer characteristic of a s-SWNT device. The measurement was done at room temperature in vacuum (base pressure $P_b = 6.5 \times 10^{-7}$ torr). The blue and red lines help to guide the sight of the electron and hole currents. The double-side arrow shows the V_g range to operate SGM. The inset shows the AFM image of the device. The dashed line in the inset highlights where the nanotube is.

Figure 9-9 shows DC-SGM images with device transport schemes. The color scale is the device DC current. Bright spots in the images mean the current of the device is boosted when the tips above such positions. V_{tip} = -4 V, V_{top} = -8 V and V_{bottom} = 0 are fixed for all images. V_g from (a) to (g) is varied around the symmetric bias from -4.5 V to -3.3V in 0.2 V steps.

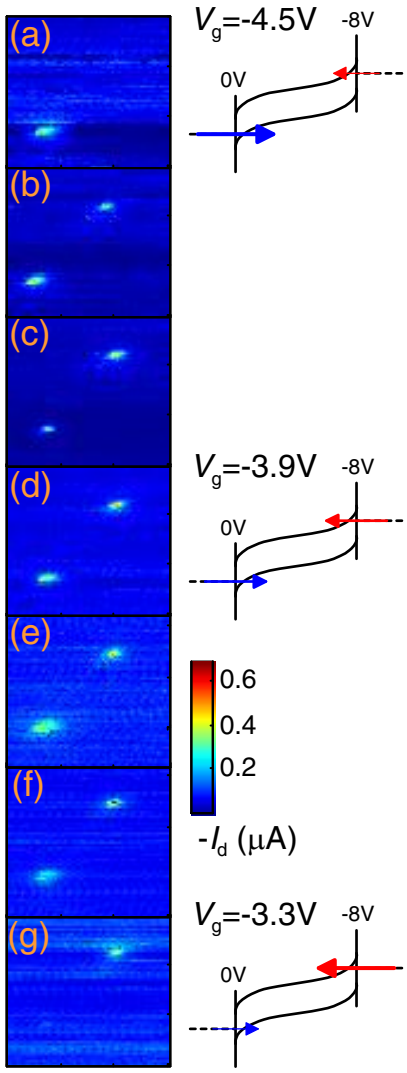

Figure 9-9. DC-SGM images with device transport schemes. The color scale is the device DC current. V_{tip} = -4 V, V_{top} = -8 V and V_{bottom} = 0 are fixed for all images. V_g from (a) to (g) is varied from -4.5 V to -3.3V in 0.2 V steps. The device transport schemes are corresponding to the images on the left.

Figure 9-9(d) represented the symmetric bias situation (V_g = -3.9 V). There are two bright spots above the nanotube near the top and the bottom contacts. The phenomenon is easy to understand in terms of electrons and holes simultaneously injected to the nanotube; electrons are injected from the top contact, while holes from the bottom. When the tip is close to the nanotube near the top contact, the tip voltage

V_{tip} = -4 V is positive with respect to the top contact voltage V_{top} = -8 V, and thus the tip enhances the electron current from the top contact $I_{e,top}$, probably by thinning the SB at the top contact. Similarly, the tip voltage V_{tip} = -4 V is negative with respect to the bottom contact voltage V_{bottom} = 0 V, and the tip enhances the hole current from the bottom $I_{h,bottom}$ when the tip is close to the nanotube near the bottom contact. Because of the high recombination of electrons and holes, the total current through the device $I_d \approx \max(I_{e,top}, I_{h,bottom})$. In the case, $I_{e,top}$ and $I_{h,bottom}$ have similar magnitudes (see the sketch next to Figure 9-9(d)), so raising either of them will enhance the total current. Hence the tip always enhances conductance of the device whenever the tip is above the nanotube near the contacts. Analogous circumstances happen when V_g is not very far away from the symmetric situation (see Figure 9-9(b), (c), (f), and (g)).

However, when V_g is far away from the symmetric situation, things start to change. In Figure 9-9(a) only one bright spot appears on the nanotube near the bottom contact when $V_g \sim$ -4.5 V. The reason for that is $I_{h,bottom} >> I_{e,top}$ due to the potential difference between the gate and the nanotube near the bottom contact is much larger than that between the gate and the nanotube near the top contact (see the sketch next to Figure 9-9(a)). Since $I_d \approx \max(I_{e,top}, I_{h,bottom})$, when $I_{h,bottom}$ is enhanced by the tip, I_d increases and a bright spot appears on the nanotube near the bottom contact, but when $I_{e,top}$ is enhanced by the tip, I_d stays the same as $I_{h,bottom}$ so no clear feature appears on the nanotube near the top contact. The same arguments can be applied to the case in Figure 9-9(g).

From the arguments in this section, several of our assumptions about s-SWNTs can be confirmed by this SGM study: (1) Both electrons and holes can be injected into s-SWNTs simultaneously around symmetric biases. (2) The total current is determined by the currents (charges) near the contacts. (3) Variation of nanotube potentials near the contacts affects the currents (charges) near the contacts. (4) Nearly perfect electron-hole recombination happens, at least for devices of this length ($L \sim 6$ μm).

Chapter 10

Contacts to Semiconducting SWNTs

10.1 Overview

Semiconducting SWNTs have advantageous materials properties for FET applications: intrinsic nanoscale dimensions (i.e. "ultra-thin body") [155], high mobility [28], and high carrier velocity [46]. These advantages come from the bulk properties of s-SWNTs. However, as in normal semiconductors, the contacts are always an issue to be considered. In general, Schottky barriers (SBs) are formed between metal electrodes and a s-SWNT. In contrast to conventional planar bulk semiconductor junctions, the depletion width for nanotubes varies exponentially with inverse doping [156]. In addition, ineffective screening of the long-range Coulomb interaction in 1D nanotube contacts makes a very long-range (logarithmic) tail in the charge distribution [116,156]. These effects in s-SWNTs have been suggested to open new possibilities for device design [156].

As-fabricated s-SWNT in an FET geometry (SWNT-FETs) are typically found to be p-type [16,17], and doping was originally assumed to be the cause. Tans *et al*. [16] argued that SWNT-FETs were p-type due to doping by the electrodes (i.e. negative SB), while the IBM group [17] argued that the positive threshold indicated a uniform p-doping of the nanotube itself, such as by adsorbed oxygen [8]. However, until now in the literature the only evidence for doping in nanotube devices is the positive threshold voltage.

Later the group of Avouris *et al*. posited that p- vs. n-type behavior was determined entirely by the SWNT/electrode interface [157,158], and explicitly rejected doping. They also argued that the effect of oxygen is to reduce the SB height of the SWNT/electrode interface [159,160]. Avouris *et al*. modeled the (short-channel) s-SWNT-FET as a ballistic Schottky barrier FET (SB-SWNT-FET), in which the conductance is modulated by the gate field through narrowing of the SBs through which electrons tunnel [157]. SB-SWNT-FETs thus display unusual vertical scaling [161], large subthreshold swings [28,158], and ambipolar behavior [46,128,162]. (Subthreshold swing S is defined as $(d\log I_d/dV_g)^{-1}$ for a FET in the exponential turn-on regime. SB-SWNT-FETs have an exponential turn-on (due to the narrowing of the SBs) that occurs when the Fermi level lies within the band. This is referred to as "subthreshold" behavior, but is not subthreshold because in the SB device there are already holes present in this region.) Even though they rely on tunneling, high on-currents may be realized in SB-SWNT-FETs with thin gate dielectrics, due to the nanoscale diameter of s-SWNTs and their small effective mass. More recently negative SB height "ohmic" contacts to nanotubes have been established through the use of other metals (e.g. Pd) [44], and provide another route to high on-currents, and additionally provide near-ideal subthreshold swings.

It appears that in the literature there is no uniform agreement of nanotube p-type behaviors in air: whether nanotubes are p-doped or p-type behaviors were only determined by the SB heights at the SWNT/electrode interfaces. Also, whether doping is a major factor in device performance is far from settled. In this chapter, we will resolve the uncertainty of nanotube p-type behaviors in air by showing that the

observed p-type behavior cannot be explained by contact work function, but is instead to be due to doping of the nanotube. Moreover, we will show that, in addition to SB-SWNT-FETs with thin dielectrics, and negative SB contacts (e.g. Pd), doping provides a third route to obtain high on-currents in a SWNT-FET. Modest doping of the SWNT narrows the SBs and provides a high-conductance tunnel contact from electrode to SWNT. This tunnel contact is "ohmic": in the on-state its conductance does not depend strongly on temperature or gate or drain voltages [70], though in the off-state it provides poor subthreshold swings [155].

10.2 Electrical Heating

SWNTs were grown using a CVD process and device fabrication is the same as that described in Chapter 2. Electrical measurements were performed by grounding the source electrode ($V_s = 0$) and applying V_d to the drain, and V_g to the gate, while measuring the drain current I_d in a ^{4}He cryostat or in ambient. High electrical bias (up to ±50 V) is applied to s-SWNT devices in vacuum, causing electrical heating due to high power dissipation (> 1 mW) in the devices. The measured nanotube diameters d range from 1.6 to 4.2 nm, with most around 2 nm.

Figure 10-1 shows V_d up to ±50 V was applied to a s-SWNT (d = 2.2 nm and L = 9 μm) device at $V_g = 0$. The device conducts well originally at low bias (sweep 1). After applying large V_d (sweep 1), the conductivity is lower when V_d is ramped down (sweep 2) compared with sweep 1. A low-conductance gap of width ~ 10 V is seen in the low-bias region when V_d returns to small values (sweep 3). This gap at low bias due to the application of high V_d is irreversible while the device remains in vacuum; the original conductance at zero gate voltage can not be recovered by

application of V_g or V_d; it is different from the previously-observed hysteresis [29] in SWNT-FETs due to charge trapping in the gate dielectric. The original conductance at zero gate voltage is completely recovered when the device is exposed to atmospheric gas (not shown). The device can be cycled between these two states (which we will refer to as "high-conductance state" and "low-conductance state") repeatedly by applying high V_d or exposing it to air. Applying large V_d to m-SWNT devices does not change the I_d-V_d characteristic (see the inset of Figure 10-1).

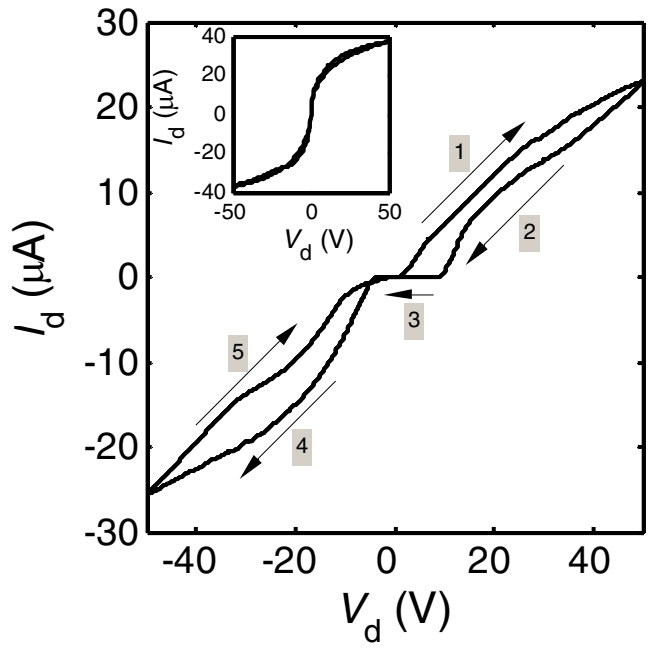

Figure 10-1. Drain current I_d vs. drain voltage V_d for SWNT devices. Main panel shows I_d vs. V_d for a semiconducting SWNT with V_d up to 50 V at $V_g = 0$ and $T = 1.4$ K. The arrows and numbers indicate sweep directions and sequence of sweeps of V_d. Inset is I_d vs. V_d for the same V_d range for a m-SWNT device ($d = 2.0$ nm and $L = 9$ μm) at $T = 5$ K. (In this case a gate voltage $V_g = V_d/2$ was applied during the sweep of V_d.)

10.3 Intrinsic s-SWNTs Behaviors with SBs

Figure 10-2 depicts transfer curves of the same s-SWNT device at different temperatures T in the high-conductance state (Figure 10-2(a)) and in the low-conductance state (Figure 10-2(b)). In both cases $V_d = 0.1$ V. Note that for all data in this chapter the drain voltage is low (0.1-0.25 V), much lower than the biases studied in Chapters 6-9; here the contact barriers may play a significant role. The device shows ambipolar behavior in both states [46,128] (data of higher positive V_g in the high-conductance state is not shown), but in the low-conductance state the ambipolar behavior is very symmetric; at all temperatures the hole and electron on-currents are the same order of magnitude, and the subthreshold swings S are similar. (Note that majority-carrier currents are studied in all cases; minority carrier current and recombination current do not play a role, due to the low drain field. The devices are "ambipolar" only in the sense that at positive gate voltage we measure majority-electron current, and at negative gate voltage we measure majority-hole current.) Around $V_g = 0$ (-3 V < V_g < 3 V) in the low-conductance state, S values for holes and electrons are very large (on order 10 V/decade), and the current decreases very quickly with temperature.

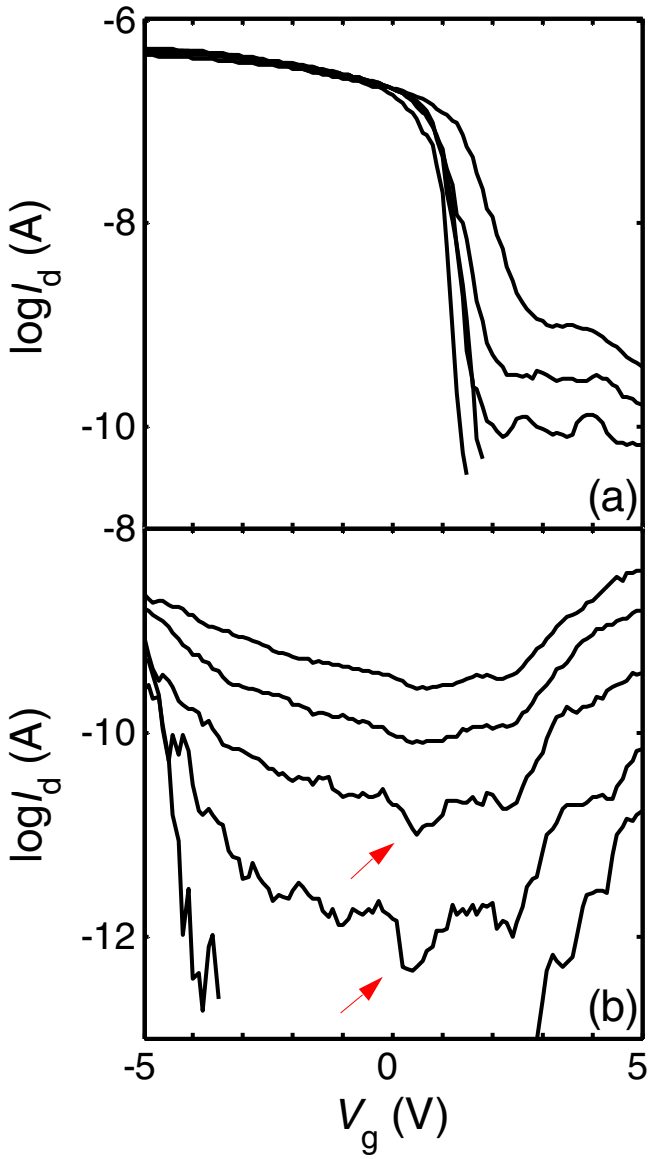

Figure 10-2. Transfer characteristics of a s-SWNT device. (a) High-conductance state. (b) Low-conductance state. The five curves in both (a) and (b) are at T = 300, 250, 200, 150 and 100 K from top to bottom, respectively, and V_d = 0.1 V. The arrows in (b) point to the V_g range where the Fermi level in the nanotube lies in the band gap.

We first examine the temperature dependence of the conductance in the low-conductance state in the region near $V_g = 0$. Figure 10-3 shows the data from Figure 10-2(b) at several V_g values on an Arrhenius plot. An effective activation energy E_a can then be extracted. Figure 10-4 shows E_a as a function of V_g extracted from Figure

10-3; over a large range (-3 V < V_g < 3 V) E_a has a fairly constant value of ~150 meV, and is similar for electrons (V_g > 0) and holes (V_g < 0). The estimated energy gap for this nanotube of diameter d = 2.2 nm is E_g = 380 meV [39]. (Here the overlap integral we use is 2.89 eV [39], a more precise value from Roman spectroscopy.) We interpret E_a as the SB height [163], which is similar for electrons and holes, indicating midgap alignment of the metal Fermi level.

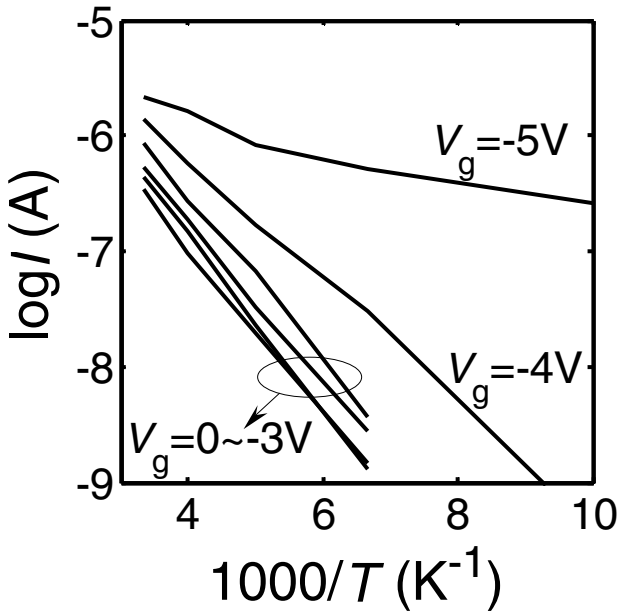

Figure 10-3. Arrhenius plot of the current at various gate voltages in the low-conductance state: the six curves represent V_g values ranging from -5 V to 0 V, in steps of 1 V.

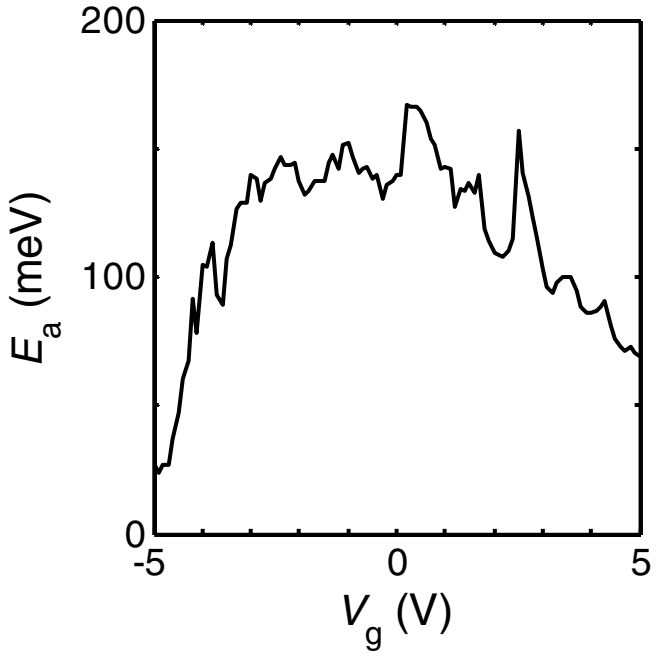

Figure 10-4. Activation energy E_a vs. gate voltage V_g in the low-conductance state.

Due to the competition between tunneling and thermionic emission, the measured activation energy is less than the SB height, but approaches the true SB height in the limit of an intrinsic SWNT with thick gate dielectric at small V_g [163], as in our case here. At higher carrier density (due to doping or large V_g) the barrier is thinned, enhancing the tunneling contribution and lowering the measured activation energy compared to the true SB height. A thorough treatment of tunneling vs. thermionic emission in SWNT/electrode junctions is given in [163]. Here we verify for the first time the prediction of Ref. [163] that the activation energy indeed gives the expected SB height in the intrinsic SWNT at low V_g. The only previous reports in the literature which extract an activation energy for SWNT-FETs on thick dielectric use a large positive or negative gate voltage to put the device in the on-state [162,164]; in these cases the activation energy are smaller than the SB height due to

tunneling. This effect is also seen in our work at large gate voltages; see Figure 10-4, in which the activation energy is already lower than ~ 25 meV at V_g = -5 V.

The current shows a dip (arrows in Figure 10-2(b)) near $V_g = 0$ with a width of ~ 0.4 V. In order to interpret this feature, we must discuss the gate coupling, i.e. the shift in Fermi level with gate voltage. The gate coupling is given by

$$\frac{dE_F}{d(eV_g)} = \frac{C_g}{C_g + C_q}\frac{C_g}{C_g + C_s + C_d} \qquad \text{Equation 10-1}$$

where C_s ,C_d, and C_g are the electrostatic capacitances of the nanotube to the gate, source, and drain, and C_q is the quantum capacitance of the nanotube, equal to $e^2D(E)$ where $D(E)$ is the density of states. In the bandgap, in the absence of charge traps, the quantum capacitance is zero, and the first term is unity. The second term approaches unity for our long-channel devices. Therefore, the gate coupling is expected to be near unity when the Fermi level lies in the bandgap. We then interpret ~ 0.4 V width of the dip in current as the Fermi level crossing the gap of the nanotube. The width is close to the expected value of the gap E_g = 380 meV, and in that region the activation energy is ~ 170 meV (see Figure 10-4), approximately $E_g/2$. The dip occurs near $V_g = 0$ indicating the s-SWNT is nearly intrinsic. Outside of this region the effective SB height is expected to be lowered by thermally-assisted tunneling [163]. We conclude that the low-conductance state corresponds to an intrinsic s-SWNT with symmetric SBs for electrons and holes.

10.4 Cause of p-Type Behavior of s-SWNTs in Air

We now turn to the high-conductance state produced by exposure to air. As seen in Figure 10-5, the device has higher on-conductance in the p-type region

compared to the low-conductance state, while on-conductance in the n-type region is nearly unchanged. The subthreshold swing in the p-type region is smaller than in the low-conductance state, but still much larger than the $k_B T \ln 10/e \approx 60$ mV/decade (k_B is Boltzmann's constant, and e is the electronic charge) expected for an ideal MOSFET at room temperature [92]. The off-conductance (minimum conductance) is nearly identical to that in low-conductance state. We explore two possible explanations for the hole conduction enhancement observed upon air exposure: the metal electrode work function is increased, or the nanotube is doped.

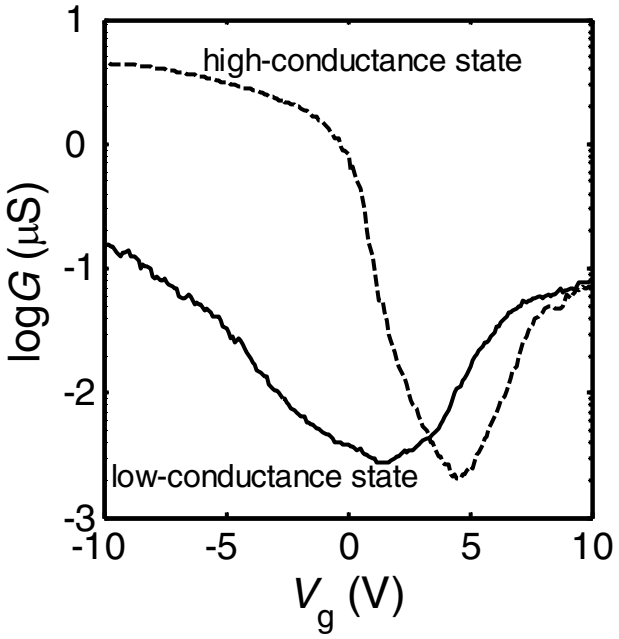

Figure 10-5. Conductance vs. V_g at T = 300 K. The dashed and solid lines are taken in the high-conductance state and the low-conductance state, respectively.

Increase in metal work function should result in the following effects. First, n-type conduction should be suppressed because of increasing SB height for electrons [157]. Careful calculations by Heinze *et al*. [157] show that the electron conductance

is indeed strongly modified by the band lineup (see Figure 10-6 (courtesy Fig. 1(b) in Ref [157]) – note that here the barrier to electrons is being made smaller and that to holes is increasing, but the situation would be identical for increasing barrier to electrons since electron-hole symmetry is assumed). This is not surprising. The s-SWNT channel is an intrinsic semiconductor with near-perfect electron-hole symmetry; the conductance of the SWNT channel itself should be nearly identical for electrons and holes. When the Fermi level lies in the conduction band, the conductance of the channel is dominated by the large SBs at the source and drain. Increasing the size of these barriers (making the work function more negative) exponentially reduces the conductance. In contrast, Figure 10-5 shows that n-type conductance is nearly identical in the high- and low-conductance states. Second, the off-conductance (minimum conductance) should decrease exponentially as the barrier for electrons increases, which is also not seen in Figure 10-5. The observation of very similar off-conductance in the high-conductance and low-conductance states indicates similar SB heights. Therefore, we rule out metal contact work function change as the explanation for the high-conductance state.

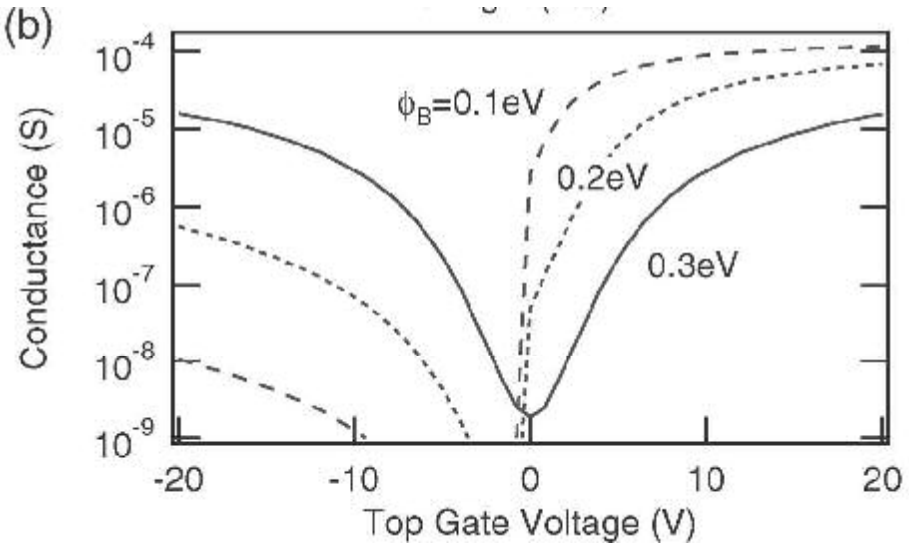

Figure 10-6. Corresponding conductance versus gate voltage at room temperature, for different SBs. The SB height for electrons is indicated for each curve. (Device geometry: 50 nm metal contacts on the left and right; a ground plane 120 nm and a top gate 100 nm away from the nanotube. Courtesy Fig. 1(b) in S. Heinze et al., *Physical Review Letters* **89**, 106801 (2002))

In contrast, p-type chemical doping of s-SWNTs upon air exposure can explain our experimental results. Chemical doping not only increases free carriers in nanotubes, but also changes the SB thickness by varying the depletion width W_p [156]. The depletion width for nanotubes varies exponentially with the inverse of the doping density D_p [156]:

$$W_p \approx \frac{d}{2}\exp\left(\frac{2\varepsilon\varepsilon_0 E_g}{e^2 dND_p}\right), \qquad \text{Equation 10-2}$$

where ε_0 is the electric constant, $\varepsilon \approx 2.45$ the average dielectric constant of the oxide and vacuum, and $N \approx 38$ nm^{-2} is carbons atoms per unit surface area. In Figure 10-2(a), the gate voltage needed to remove all the carriers is ~ 1.6 V. Assuming a gate capacitance per length $c_g \approx 0.20$ pF/cm in our device geometry [28,46], we

estimate the doping level D_p is about 2.0×10^6 cm^{-1} $\approx 7.6 \times 10^{-4}$ holes/carbon. Then $W_p \approx 5.5$ nm, which is at least one order of magnitude smaller than the SB thickness controlled by electrostatic gating in our device geometry [116,157]. The thin SB due to a thin depletion width and the unchanged SB heights for both valence and conduction bands easily explain why the on-current is enhanced in p-type conduction, while off-current is not changed in the high-conductance state compared with the low-conductance state. Note that in the high-conductance state, the temperature dependence of the conductance at negative V_g is small or negligible (see Figure 10-2(a)), and the measured activation energy is much smaller than in the low-conductance state. (Figure 10-7 shows E_a in the high-conductance state as a function of V_g extracted from Figure 10-2(a)) This arises not because of a reduction in SB height for holes (which would necessitate an increase in SB height for electrons), but rather due to tunneling dominating thermionic emission as the SB is thinned by hole-doping. Therefore, the activation energy underestimates the SB height when doping is present.

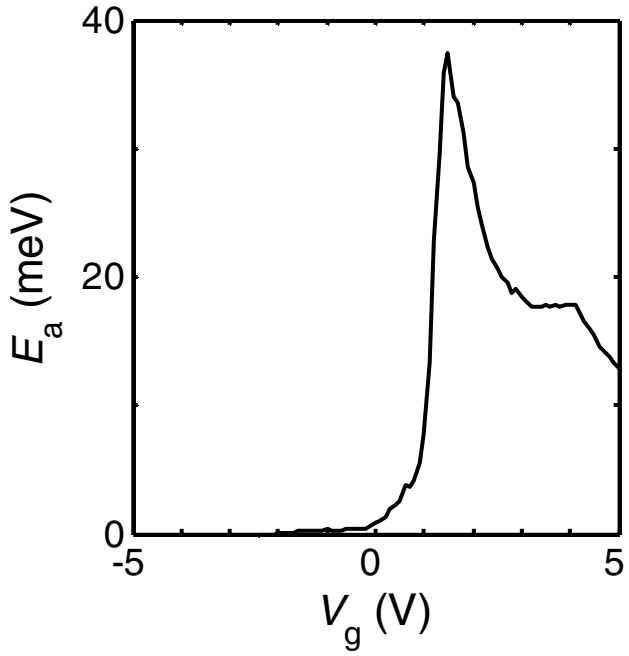

Figure 10-7. Activation energy E_a vs. gate voltage V_g in the high-conductance state.

The exact nature of the chemical doping remains unclear. The obvious possibility is that oxygen adsorbs on the s-SWNTs, accepting electrons. Oxygen is known to affect the thermopower and resistivity of bulk SWNT samples [8]. Jhi *et al.* [165] predicted that adsorbed O_2 donated 0.1 hole per adsorbed molecule to the SWNT. However, a recent paper [166] exploring s-SWNTs with one section suspended across a trench found that the s-SWNT section bound on the SiO_2 substrate is p-type doped (with a similar doping magnitude observed here), and the suspended s-SWNT is undoped; this raises the possibility that SWNT doping arises from an interaction with the SiO_2 substrate. For solution-processed SWNTs on Au electrodes, annealing produced n-type FETs, and exposure to O_2 restored p-type operation, interpreted there as due to changes in metal work function [159]. However, the origin of n-type behavior in the annealed FETs remains unclear, so a complete picture is

lacking. More controlled study to clarify the origins and the effects of chemical doping, and its dependence on device processing and ambient conditions is required.

In conclusion, we have shown that dissipating high power in a SWNT-FET can reveal its intrinsic undoped behavior. In ambient environment, s-SWNTs on SiO_2 substrates are doped, and such chemical doping offers a new route to high on-currents in SB-SWNT-FETs. It is notable that the effects demonstrated here also form the basis of an electronically-programmable FET: application of a high electrical current is sufficient to reduce the on-current by two orders of magnitude and effectively remove a particular FET from a circuit.

Chapter 11

Future Directions

Unfortunately I was not able to obtain understandable or conclusive results on spin valve measurements in nanotube-based devices during my graduate study; the spin valve effect I see is not consistent. However, I believe that the experiments should be successful if more reliable devices could be constructed by making good tunneling barriers between nanotube and ferromagnetic leads. This would allow systematic study and understanding of spin transport in nanotubes.

My expectation is that high bias transport is insensitive to temperature since it is far from equilibrium. Measuring the temperature effect to prove this prediction would be useful. From the Boltzmann equation calculation we know the carrier density in nanotubes plays an important role to determine the carrier velocity. Extending the nanotube device modeling of Chapter 7 to include the results from Chapter 8 (saturation velocity depending on carrier density) would be a logical next step, which I unfortunately was unable to finish during my Ph.D. The comparison of high bias experiments in metallic nanotubes, small bandgap and large bandgap semiconducting nanotubes will be interesting, too, to investigate the dependence of the current-carrying capacity on bandgap (and subband spacing) as well as on carrier density. Because the band structures of different kinds of nanotubes at high energy are similar, current-carrying capacity at high gate voltages (high carrier densities) should be very similar.

I will also try to expand my simple Boltzmann equation calculation to m-SWNTs, and compare that to the experimental results. It will be nice to consider first a two-subband calculation, including interband scattering transitions because the second subband is reachable in the gate field that researchers typically apply. Recent experiments on single layer graphite (graphene) and few-layer graphite [167-175] open the possibility of studying transport at high bias in these new all-carbon nanostructures. They are structurally similar to nanotubes, but two dimensional materials. Expanding the Boltzmann equation calculation to anticipate what happens in truly two dimensional systems will be very interesting. In addition, if the experimental results can come out at the same time, that should be a remarkable work.

There remains a mystery in the ambipolar transport at high bias in s-SWNTs: the current dips in the I-V_g characteristic curves are sharper than what is calculated considering electron-hole recombination (Chapter 9). EFM in this bias region can provide the potential distribution along the nanotube, and may give us a hint. I attempted to accomplish EFM on devices in the ambipolar regime, but the results were inconclusive; longer devices will likely greatly improve the results. Also, high bias EFM in the unipolar region will also tell us about the details of the pinch-off effect in nanotubes, which currently relies on assumptions in my device modeling.

Appendix A Deriving Electrostatic Potential from EFM Signal

A.1 Processes of Deriving Electrostatic Potential from EFM Signal

Figure A-1(a) shows an AFM image; (b), (d), (f), (h) show a series of EFM images; (c), (e), (g), (i) show the corresponding EFM signals vs. the position along the vertical direction. The technique for this series of EFM images is AC-tip-EFM, as described in Chapter 3. The device is biased at $V_d = 0$, $V_s = 0$ in (b), (c); $V_d = 0$, $V_s = -1$ V in (d), (e); $V_d = -1$ V, $V_s = 0$ in (f), (g); $V_d = -1$ V, $V_s = -1$ V in (h), (i). The goal is to get electrostatic potential profile of a nanotube while the device is biased at $V_d = 0$, $V_s = -1$ V or $V_d = -1$ V, $V_s = 0$. The images taken at $V_d = 0$, $V_s = 0$ and $V_d = -1$ V, $V_s = -1$ V are for reference.

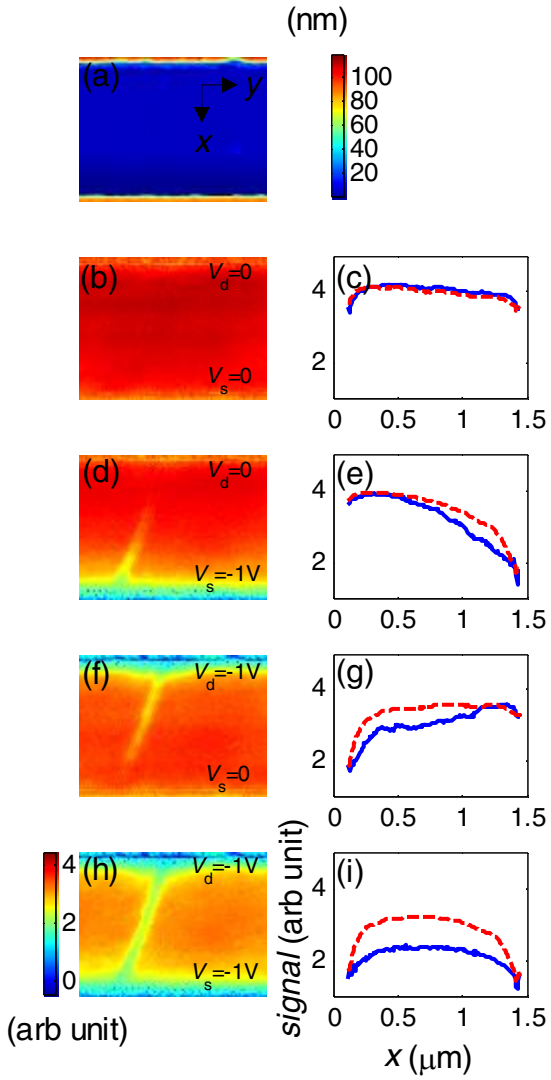

Figure A-1. EFM images, AFM corresponding image, and signal profiles from EFM images. The scan sizes for all images are 1.5 × 1.5 μm^2. (a) AFM image. The nanotube is barely seen between electrodes. (b), (d), (f), (h) EFM images. The top and bottom electrode biases (V_d and V_s) for all images are labeled. The gate bias V_g equals 0.4 V. The amplitude and frequency of AC tip bias $V_{ac,tip}(\omega)$ equals 0.2 V and 13 kHz, respectively. (c), (e), (g), (i) corresponding signal profiles. The blue solid and red dashed lines represent the signal profiles on the nanotube and bare substrate (SiO_2), respectively.

The nanotube only can be barely seen in AFM image, but it seen clearly in EFM images. The position of nanotube can be determined from both AFM and EFM

images. The EFM signals on the nanotube can be traced. The blue solid lines in Figure A-1(c), (e), (g), (i) are the signal profiles on the nanotube. The red dashed lines are the signal profiles on the substrate. Presumably the EFM signals on the nanotube come from both the nanotube potentials and the substrate potentials. The remaining signal after subtracting the blue solid curves from the red dashed curves indicate the signals from the nanotube potentials only.

Figure A-2 shows the EFM signals from the nanotube only. When the device is biased at $V_d = V_s = 0$, the whole nanotube should have the same potential 0 since the nanotube is conducting. Similarly, the whole nanotube have potential -1 V when $V_d = V_s = -1$ V. The top and bottom blue dashed curves in Figure A-2 therefore mean the EFM signals form the nanotube when the nanotube whole potentials are 0 and –1 V, respectively. Also as expected, the signals of the device biased at $V_d = 0$, $V_s = -1$ V and $V_d = -1$ V, $V_s = 0$ are between the signals at $V_d = V_s = 0$ and $V_d = V_s = -1$ V because the nanotube potentials supposedly are between 0 and -1 V when $V_d = 0$, $V_s = -1$ V or $V_d = -1$ V, $V_s = 0$.

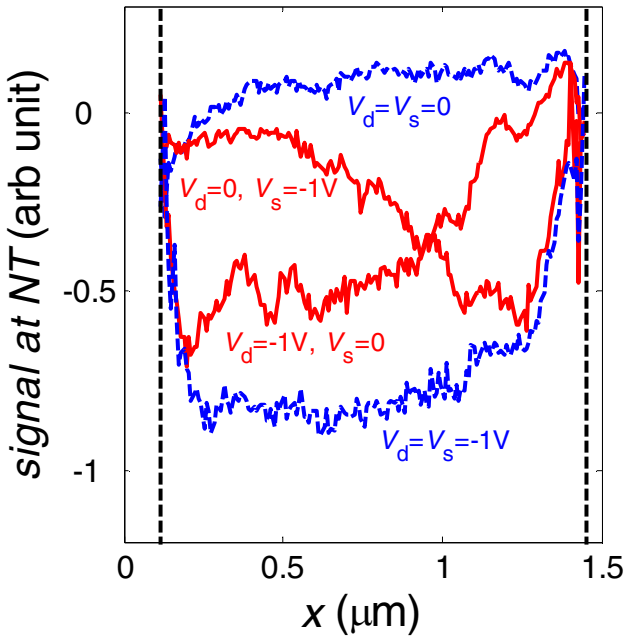

Figure A-2. EFM signals on the nanotube after the subtraction from the background signal (the signal on the bare substrate). The black dashed lines indicate the edges of the electrodes.

If we assume the EFM signal difference and the potential difference is linear (we will check the linearity in the next section), that means,

$$V_1 - V_2 \propto A(V_1) - A(V_2), \qquad \text{Equation A-1}$$

where $A(V)$ is the EFM signal with the nanotube potential V, then we can derive the potential of nanotube at any position when $V_d = 0$, $V_s = -1$ V or $V_d = -1$ V, $V_s = 0$ by

$$\frac{V-(-1)}{0-(-1)} = \frac{A(V)-A(-1)}{A(0)-A(-1)}. \qquad \text{Equation A-2}$$

Figure A-3 shows the result of linear interpolation. At different bias conditions, the potentials and, therefore, the resistance distribution are very different. This is why EFM provides unique transport information. As we observe, the derived potentials near the contacts show greater uncertainty. In other words, when the nanotube gets closer to the contacts, the potentials there are harder to extract. This is

because the device geometry near the contacts changes dramatically; the contacts are much taller than the rest of device. Also, the signals from the contacts are very strong. It is harder to eliminate large signals from the contacts to get small signals from the nanotube properly.

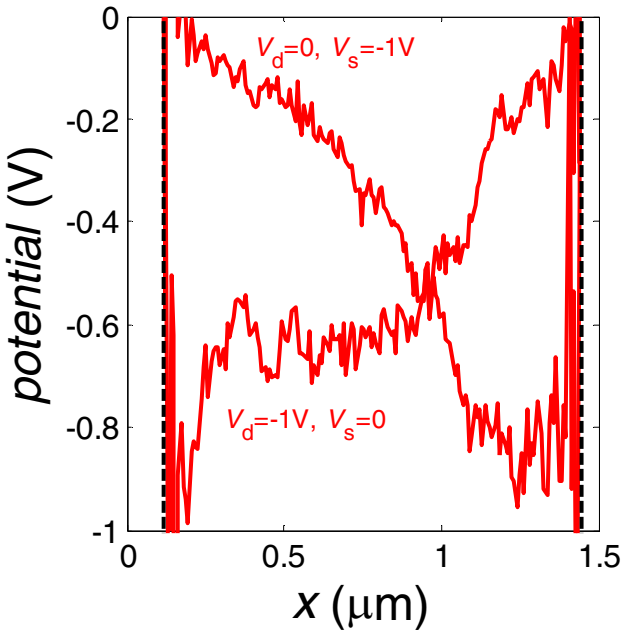

Figure A-3. The converted potential profiles on the nanotube.

A.2 Linearity

Here we would like to check whether the assumption "linearity", or basically Equation A-1, is a proper idea. Figure A-4 shows the EFM signals from nanotube only, as Figure A-2. Each curve is at $V_d = V_s$ from -1 V to 0 in 0.2 V steps. If Equation A-1 is true, each curve in Figure A-4 should be equally spaced to the adjacent curves. The curves look more or less equally spaced in the middle, but not near the contacts. Also, when the biases increase, the nonlinearity effect will get larger. Few possible reasons make the analysis near the contacts worse. Besides the

reasons mentioned in the previous section, there might be some data processing errors which come from the uncertainty of nanotube positions near the contacts. Even though the linearity test fails near the contacts, the derived potentials away from the contact are still reliable. Sometimes we can extrapolate the potential profiles of nanotubes toward the contacts, and estimate the contact resistances accordingly.

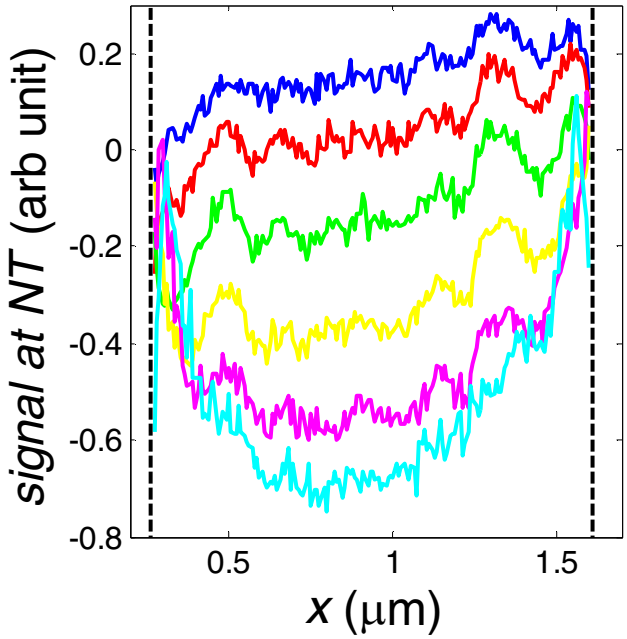

Figure A-4. EFM signals on the nanotube after the subtraction from the background signal. V_g = 0.5 V and $V_{ac,tip}(\omega)$ = 0.2 V are for all curves. Each curve is at $V_d = V_s$ from -1 V to 0 in 0.2 V steps.

Appendix B

Matlab Codes

B.1 General Notes

This code is not fully developed, and I am not very professional in code writing. So the codes might not be very easy to understand. The texts or sentences which start by "%" or "%%" are short explanations of the codes; they do not belong to the code itself.

B.2 Code for Device Modeling

%% analytically calculate the hole current of the device at different bias conditions when the carriers experience velocity saturation at high electric field

%% calculate nanotube potential at the contacts when the quasi-Fermi levels of nanotube bands are in equilibrium with the Fermi levels of the contacts

```
% constants; MKS unit
vFm=9.35e5;
h=6.626e-34;
qe=-1.6e-19;

% ground chosen and geometry factors and parameters
Vs=0;
```

```
Cg=0.2e-10;
del=0.2*1.6e-19;

for k=1:199;
   for l=1:19;
      Vd(k,l)=(-k+100)*0.1;
      Vg(k,l)=l-10;
      dE0d=abs(qe*1);
      dE0s=abs(qe*1);
      if qe*(Vd(k,l)-Vg(k,l))>del
         E0dguess=qe*Vd(k,l)-del;
         while dE0d>abs(qe*1e-6)
            if (qe*Vd(k,l)-E0dguess-del)>0
               nde(k,l)=2*4/h/vFm*(abs((qe*Vd(k,l)-E0dguess)^2-del^2))^0.5;
            else
               nde(k,l)=0;
            end
            E0d(k,l)=qe*(qe*nde(k,l)/Cg+Vg(k,l));
            dE0d=abs(E0d(k,l)-E0dguess);
            E0dguess=E0dguess+1e-3*(E0d(k,l)-E0dguess);
         end
      end
      if (qe*(Vd(k,l)-Vg(k,l))>=0)&(qe*(Vd(k,l)-Vg(k,l))<=del)
```

```
    E0d(k,l)=qe*Vg(k,l);
    nde(k,l)=0;
end
if qe*(Vg(k,l)-Vd(k,l))>del
    E0dguess=qe*Vd(k,l)+del;
    while dE0d>abs(qe*1e-6)
        if (E0dguess-qe*Vd(k,l)-del)>0
            ndh(k,l)=2*4/h/vFm*(abs((qe*Vd(k,l)-E0dguess)^2-del^2))^0.5;
        else
            ndh(k,l)=0;
        end
        E0d(k,l)=qe*(-qe*ndh(k,l)/Cg+Vg(k,l));
        dE0d=abs(E0d(k,l)-E0dguess);
        E0dguess=E0dguess+1e-3*(E0d(k,l)-E0dguess);
    end
end
if (qe*(Vg(k,l)-Vd(k,l))>=0)&(qe*(Vg(k,l)-Vd(k,l))<=del)
    E0d(k,l)=qe*Vg(k,l);
    ndh(k,l)=0;
end
if qe*(Vs-Vg(k,l))>del
    E0sguess=qe*Vs-del;
    while dE0s>abs(qe*1e-6)
```

```
        if (qe*Vs-E0sguess-del)>0
            nse(k,l)=2*4/h/vFm*(abs((qe*Vs-E0sguess)^2-del^2))^0.5;
        else
            nse(k,l)=0;
        end
        E0s(k,l)=qe*(qe*nse(k,l)/Cg+Vg(k,l));
        dE0s=abs(E0s(k,l)-E0sguess);
        E0sguess=E0sguess+1e-3*(E0s(k,l)-E0sguess);
    end
end
if (qe*(Vs-Vg(k,l))>=0)&(qe*(Vs-Vg(k,l))<=del)
    E0s(k,l)=qe*Vg(k,l);
    nse(k,l)=0;
end
if qe*(Vg(k,l)-Vs)>del
    E0sguess=qe*Vs+del;
    while dE0s>abs(qe*1e-6)
        if (E0sguess-qe*Vs-del)>0
            nsh(k,l)=2*4/h/vFm*(abs((qe*Vs-E0sguess)^2-del^2))^0.5;
        else
            nsh(k,l)=0;
        end
        E0s(k,l)=qe*(-qe*nsh(k,l)/Cg+Vg(k,l));
```

```
            dE0s=abs(E0s(k,l)-E0sguess);
            E0sguess=E0sguess+1e-3*(E0s(k,l)-E0sguess);
          end
        end
        if (qe*(Vg(k,l)-Vs)>=0)&(qe*(Vg(k,l)-Vs)<=del)
          E0s(k,l)=qe*Vg(k,l);
          nsh(k,l)=0;
        end
      end
    end
    phid=E0d/qe; % phid is nanotube potential at drain
    phis=E0s/qe; % phis is nanotube potential at source

    %% Calculate the hole current analytically when carrier experience velocity saturation.

    % geometry factors and parameters
    Cg=0.2e-10;
    L=20e-6;
    % undetermined parameters
    mu0=2.7;
    vs=2e5;
```

```
for k=1:199;
   for l=1:19;
      if (Vd(k,l)>0)&(Vg(k,l)<0)
         if phis(k,l)>(1/mu0*(L*vs+phid(k,l)*mu0-...
               (L^2*vs^2+2*L*vs*mu0*(phid(k,l)-Vg(k,l)))^0.5))     %     when
pinch off happens at source
            I(k,l)=1/(L/mu0+(phid(k,l)-phis(k,l))/vs)*Cg*...
               (1/2*(phid(k,l)^2-phis(k,l)^2)-...
               Vg(k,l)*(phid(k,l)-phis(k,l)));
         else % when pinch off does not happen
            I(k,l)=-Cg*vs*((L*vs)^1.5+2*(L*vs)^0.5*mu0*(phid(k,l)-Vg(k,l))-
...
               L*vs*(L*vs+2*mu0*(phid(k,l)-Vg(k,l)))^0.5-...
               mu0*(phid(k,l)-Vg(k,l))*(L*vs+2*mu0*(phid(k,l)-
Vg(k,l)))^0.5)/...
               (mu0*(L*vs+2*mu0*(phid(k,l)-Vg(k,l)))^0.5);
         end
      elseif (Vd(k,l)<0)&(Vg(k,l)<=Vd(k,l))
         if phid(k,l)>(1/mu0*(L*vs+phis(k,l)*mu0-...
               (L^2*vs^2+2*L*vs*mu0*(phis(k,l)-Vg(k,l)))^0.5))     %     when
pinch off happens at drain
            I(k,l)=1/(L/mu0-(phid(k,l)-phis(k,l))/vs)*Cg*...
               (1/2*(phid(k,l)^2-phis(k,l)^2)-...
```

```
                    Vg(k,l)*(phid(k,l)-phis(k,l)));
                else % when pinch off does not happen
                    I(k,l)=Cg*vs*((L*vs)^1.5+2*(L*vs)^0.5*mu0*(phis(k,l)-Vg(k,l))-...
                    L*vs*(L*vs+2*mu0*(phis(k,l)-Vg(k,l)))^0.5-...
                    mu0*(phis(k,l)-Vg(k,l))*(L*vs+2*mu0*(phis(k,l)-
Vg(k,l)))^0.5)/...
                    (mu0*(L*vs+2*mu0*(phis(k,l)-Vg(k,l)))^0.5);
                end
            end
        end
    end
```

%% numerically calculate the hole current of the device at different bias conditions when the carriers experience velocity saturation at high electric field

```
%% calculate potential at the contacts
function [phi0,phiL,Vd,Vg]=potentialcalculate_atcontacts;

%% constants
vFm=9.35e5;
h=6.626e-34;
qe=-1.6e-19;
```

```
%% ground chosen and geometry factors and parameters
Vs=0;
Cg=0.2e-10;
del=0.2*1.6e-19;

for k=1:199;
   for l=1:199;
      Vd(k,l)=(-k+100)*0.1; % Vd from 9.9 to -9.9 V
      Vg(k,l)=(l-200)*0.1; % Vg from -19.9 to -0.1 V
      dE0d=abs(qe*1);
      dE0s=abs(qe*1);
      if qe*(Vd(k,l)-Vg(k,l))>del
         E0dguess=qe*Vd(k,l)-del;
         while dE0d>abs(qe*1e-6)
            if (qe*Vd(k,l)-E0dguess-del)>0
               nde(k,l)=2*4/h/vFm*(abs((qe*Vd(k,l)-E0dguess)^2-del^2))^0.5;
            else
               nde(k,l)=0;
            end
            E0d(k,l)=qe*(qe*nde(k,l)/Cg+Vg(k,l));
            dE0d=abs(E0d(k,l)-E0dguess);
            E0dguess=E0dguess+1e-3*(E0d(k,l)-E0dguess);
         end
```

```
end
if (qe*(Vd(k,l)-Vg(k,l))>=0)&(qe*(Vd(k,l)-Vg(k,l))<=del)
   E0d(k,l)=qe*Vg(k,l);
   nde(k,l)=0;
end
if qe*(Vg(k,l)-Vd(k,l))>del
   E0dguess=qe*Vd(k,l)+del;
   while dE0d>abs(qe*1e-6)
      if (E0dguess-qe*Vd(k,l)-del)>0
         ndh(k,l)=2*4/h/vFm*(abs((qe*Vd(k,l)-E0dguess)^2-del^2))^0.5;
      else
         ndh(k,l)=0;
      end
      E0d(k,l)=qe*(-qe*ndh(k,l)/Cg+Vg(k,l));
      dE0d=abs(E0d(k,l)-E0dguess);
      E0dguess=E0dguess+1e-3*(E0d(k,l)-E0dguess);
   end
end
if (qe*(Vg(k,l)-Vd(k,l))>=0)&(qe*(Vg(k,l)-Vd(k,l))<=del)
   E0d(k,l)=qe*Vg(k,l);
   ndh(k,l)=0;
end
if qe*(Vs-Vg(k,l))>del
```

```
    E0sguess=qe*Vs-del;
    while dE0s>abs(qe*1e-6)
        if (qe*Vs-E0sguess-del)>0
            nse(k,l)=2*4/h/vFm*(abs((qe*Vs-E0sguess)^2-del^2))^0.5;
        else
            nse(k,l)=0;
        end
        E0s(k,l)=qe*(qe*nse(k,l)/Cg+Vg(k,l));
        dE0s=abs(E0s(k,l)-E0sguess);
        E0sguess=E0sguess+1e-3*(E0s(k,l)-E0sguess);
    end
end
if (qe*(Vs-Vg(k,l))>=0)&(qe*(Vs-Vg(k,l))<=del)
    E0s(k,l)=qe*Vg(k,l);
    nse(k,l)=0;
end
if qe*(Vg(k,l)-Vs)>del
    E0sguess=qe*Vs+del;
    while dE0s>abs(qe*1e-6)
        if (E0sguess-qe*Vs-del)>0
            nsh(k,l)=2*4/h/vFm*(abs((qe*Vs-E0sguess)^2-del^2))^0.5;
        else
            nsh(k,l)=0;
```

```
                end
                E0s(k,l)=qe*(-qe*nsh(k,l)/Cg+Vg(k,l));
                dE0s=abs(E0s(k,l)-E0sguess);
                E0sguess=E0sguess+1e-3*(E0s(k,l)-E0sguess);
              end
            end
            if (qe*(Vg(k,l)-Vs)>=0)&(qe*(Vg(k,l)-Vs)<=del)
              E0s(k,l)=qe*Vg(k,l);
              nsh(k,l)=0;
            end
          end
        end
        phiL=E0d/qe;
        phi0=E0s/qe;

        %% calculate hole current with considering pinch off

        for l=199:-1:1 % for loop for different Vg
          k=101;
          Idone(k,l)=currentcalculate_negVd(Vg(k,l),phi0(k,l),phiL(k,l));   % call
function currentcalculate_negVd to calculate current
          for k=102:199 % for loop for Vd
            Idone(k,l)=currentcalculate_negVd(Vg(k,l),phi0(k,l),phiL(k,l));
```

```
            if abs(Idone(k,l)-Idone(k-1,l))<abs(Idone(k-1,l)*0.0001);
               break;
            elseif abs(Idone(k,l))<abs(Idone(k-1,l));
               break;
            elseif abs(Idone(k,l)-Idone(k-1,l))>abs(Idone(k-1,l)-Idone(k-2,l))
               break;
            end
         end
         for kk=k:199
            Idone(kk,l)=Idone(k-1,l);
         end
      end

      %% calculate hole current self consistently with negative Vd

      function [Idone,potential,field]=currentcalculate_negVd1(Vg,phi0,phiL);  %%
numerically calculate the hole current when the carriers experience velocity saturation

      %% constants
      qe=-1.6e-19;
      %% geometry factors
      Cg=0.2e-10;
      L=20e-6;
```

```
%% parameters
mu0=2.7;
vs=2e5;

%% calculation
%step
dx=1e-8;
%guess current
I=-0.5e-6;

phi(2001)=100; % away from real phiL
%calculate current
while abs(phi(2001)-phiL)>0.001;
   phi(1)=phi0;
   nh(1)=Cg/(-qe)*(phi0-Vg);
   phiprime(1)=I*vs/(I*mu0+(-qe)*mu0*vs*nh(1));
   for xindex=1:2000
      phi(xindex+1)=phi(xindex)+phiprime(xindex)*dx;
      nh(xindex+1)=Cg/(-qe)*(phi(xindex+1)-Vg);
      phiprime(xindex+1)=I*vs/(I*mu0+...
         (-qe)*mu0*vs*nh(xindex+1));
   end
   Idone=I;
```

```
    if phi(2001)<phiL;
        I=I*(1-0.001);
    else phi(2001)>phiL;
        I=I*(1+0.001);
    end
end
potential=phi;
field=-phiprime;
```

vFm	Fermi velocity of metallic nanotubes
H	Planck constant
Qe	Electron charge
Vs	Voltage at the source contact (zero because the source is grounded)
Cg	Electrostatic capacitance of nanotube per length
del	Half of nanotube bandgap
Vd	Voltage at the drain contact
Vg	Voltage at the gate
E0d	Potential energy of nanotube right at the drain contact
E0s	Potential energy of nanotube right at the source contact
E0dguess	Guess of E0d for iteration
E0sguess	Guess of E0s for iteration
nde	Electron density of nanotube right at the drain contact
nse	Electron density of nanotube right at the source contact

ndh	Hole density of nanotube right at the drain contact
nsh	Hole density of nanotube right at the source contact
phid	Potential of nanotube right at the drain contact
phis	Potential of nanotube right at the source contact
L	Channel length
mu0	Zero –field mobility
vs	Saturation velocity
I	Current from the drain contact to the source contact
dx	Step size of nanotube channel
phi	Potential of nanotube
nh	Hole density of nanotube
phiprime	Derivative of potential of nanotube with respect to nanotube position
field	Electric field along nanotube

Table B-1. Symbols using in Section B-2.

B.3 Code for Calculating Average Carrier Velocity

%% Calculate carrier velocity from nonequilibrium carrier distribution function by solving steady-state Boltzmann eq.; single band

%% Calculate fermi function

T=300; % unit is K

delta=0.2; % unit is eV

L=20e-6; % unit is m

```
for j=1:9
    n(1,j)=2*10^((j-1)/2); % charge density is ~ n x 10^5 electron /m;
    [gf,k,E,vf,nf,jp,jn,ip,in]=fermi1_k(n(1,j),T,delta,L);  % call function fermi1_k

    %% calculate velocity

    for i=1:50
        V(i,1)=0.2*i;
        [v(i,j),count(i,j),ndone(i,j)]=velocity11(V(i,1),gf,L,vf,jp,jn,ip,in);  % call function velocity11
    end
    for i=51:60
        V(i,1)=10+1*(i-50);
        [v(i,j),count(i,j),ndone(i,j)]=velocity11(V(i,1),gf,L,vf,jp,jn,ip,in);
    end
    for i=61:68
        V(i,1)=20+10*(i-60);
        [v(i,j),count(i,j),ndone(i,j)]=velocity11(V(i,1),gf,L,vf,jp,jn,ip,in);
    end
end
```

```
function [g,k,E,vf,nf,jp,jn,ip,in]=fermi1_k(n,T,delta,L); % A separate function to calculate fermi function; T's unit is K; charge density is ~ n x 10^5 electron /m; delta's unit is eV

% constant; MKS unit
kb=1.38e-23;
qe=1.6e-19;
hbar=1.055e-34;
vfm=9.35e5;

hbaromega=0.16; % unit is eV
k0=delta*qe/hbar/vfm; % unit is 1/m

dk=2*pi/L; % unit is 1/m
delk=dk/(100e-6/L); % unit is 1/m; one delk contain 4/(100e-6/L) e

for i=1:50001 % hyperbolic dispersion relation
   k(i,1)=delk*(i-25001);
   E(i,1)=hbar*vfm*(k(i,1)^2+k0^2)^0.5/qe; % unit is eV
   vf(i,1)=vfm*k(i,1)/(k(i,1)^2+k0^2)^0.5;
end

%% calculation Fermi distribution
```

```
kguess=n/2*dk/4; % 4 means 2 bands and 2 spins
muguess=hbar*vfm*(kguess^2+k0^2)^0.5/qe; % guess mu;
nguess=0;
while abs(nguess-n)>n*1e-3
   for i=1:50001
      g(i,1)=(exp((E(i,1)-muguess)*qe/(kb*T))+1)^(-1);
   end
   nguess=4*sum(g)/(100e-6/L);
   if nguess>n
      muguess=muguess*(1-1e-1);
   else
      muguess=muguess*(1+1e-1);
   end
end
nf=nguess;

%% find the states which are hbaromega=0.16 eV lower than each state k
for i=1:50001
   kp(i,1)=(((k(i,1)^2+k0^2)^0.5+hbaromega*qe/hbar/vfm)^2-k0^2)^0.5;
   kn(i,1)=(((k(i,1)^2+k0^2)^0.5-hbaromega*qe/hbar/vfm)^2-k0^2)^0.5;
end

i=1;
```

```
while int32(kp(i,1)/delk+25001)>50001
   i=i+1;
end
ip=i; % ip is the index of kp larger than 50001

i=1;
while imag(kn(i,1))==0
   i=i+1;
end
in=i; % in is the index of kn starting becoming complex

for i=1:(in-1) % kn is real upto to in-1
   jp(i,1)=int32(kp(i,1)/delk+25001);
   jn(i,1)=int32(kn(i,1)/delk+25001);
end
for i=in:25000
   jp(i,1)=int32(kp(i,1)/delk+25001);
end
i=25001;
jp(i,1)=int32(kp(i,1)/delk+25001);
for i=25002:(50002-in)
   jp(i,1)=50001+1-int32(kp(i,1)/delk+25001);
end
```

```
for i=(50002-(in-1)):50001
   jp(i,1)=50001+1-int32(kp(i,1)/delk+25001);
   jn(i,1)=50001+1-int32(kn(i,1)/delk+25001);
end
```

function [v,count,ndone,gnew]=velocity11(V,g,L,vf,jp,jn,ip,in); A separate function to calculate nonequilibrium carrier distribution by solving Boltzmann equation and then calculate average carrier velocity

```
kb=1.38e-23;
qe=1.6e-19;
hbar=1.055e-34;
vfm=9.35e5;

lpb=10e-9; % unit is m
le=300e-9; % unit is m

dk=2*pi/L; % unit is 1/m
dt=2.07e-15*(L/10e-6);
delk=dk/(100e-6/L); % unit is 1/m; one delk contain 4/(100e-6/L) e

count=0;
kgain=qe*V/L*dt/hbar; % unit is 1/m
```

```
igain=int32(kgain/delk);
v=1; vold=0;
while abs(v-vold)>vold*1e-2 % check whether v stabilize
   for j=1:500 % g evolve 500*dt
      for i=(-igain+1):0
         gnew(i+igain,1)=0;
      end
      for i=1:(ip-1) % jp is bigger than 50001 upto ip-1
         gnew(i+igain,1)=g(i,1)+(1/le*(g(50002-i,1)-g(i,1))-...
            1/lpb*(g(i,1)*((1-g(jn(i,1),1))+(1-g(50002-jn(i,1),1)))))*(-
vf(i,1))*dt; % multiply -vf because ratio of vf and le or lpb is positive
      end
      for i=ip:(in-1)
         gnew(i+igain,1)=g(i,1)+(1/le*(g(50002-i,1)-g(i,1))+...
            1/lpb*((1-g(i,1))*(g(jp(i,1),1)+g(50002-jp(i,1),1))-...
            g(i,1)*((1-g(jn(i,1),1))+(1-g(50002-jn(i,1),1)))))*(-vf(i,1))*dt;
      end
      for i=in:25000
         gnew(i+igain,1)=g(i,1)+(1/le*(g(50002-i,1)-g(i,1))+...
            1/lpb*((1-g(i,1))*(g(jp(i,1),1)+g(50002-jp(i,1),1))))*(-vf(i,1))*dt;
      end
      for i=25001:25001
         gnew(i+igain,1)=g(i,1)+(1/le*(g(50002-i,1)-g(i,1))+...
```

```
            1/lpb*((1-g(i,1))*(g(jp(i,1),1)+g(50002-jp(i,1),1))))*vf(i,1)*dt;
        end
        for i=25002:(50002-in)
            gnew(i+igain,1)=g(i,1)+(1/le*(g(50002-i,1)-g(i,1))+...
                1/lpb*((1-g(i,1))*(g(jp(i,1),1)+g(50002-jp(i,1),1))))*vf(i,1)*dt;
        end
        for i=(50002-(in-1)):(50002-ip)
            gnew(i+igain,1)=g(i,1)+(1/le*(g(50002-i,1)-g(i,1))+...
                1/lpb*((1-g(i,1))*(g(jp(i,1),1)+g(50002-jp(i,1),1))-...
                g(i,1)*((1-g(jn(i,1),1))+(1-g(50002-jn(i,1),1)))))*vf(i,1)*dt;
        end
        for i=(50002-(ip-1)):(50001-igain)
            gnew(i+igain,1)=g(i,1)+(1/le*(g(50002-i,1)-g(i,1))-...
                1/lpb*(g(i,1)*((1-g(jn(i,1),1))+(1-g(50002-jn(i,1),1)))))*vf(i,1)*dt;
        end
        g=gnew;
    end % end of 500 evolutions
    count=count+500;
    vold=v;
    ndone=4*sum(gnew)/(100e-6/L);
    v=sum(gnew.*vf)*4/(100e-6/L)/ndone;
end % end of evolution
```

T	Temperature
Delta	Half of nanotube bandgap
N	Carrier density
L	Channel length
kb	Boltzmann constant
qe	Unit charge
hbar	Planck constant devided by 2π
vfm	Fermi velocity of metallic nanotubes
hbaromega	Optical or zone-boundary phonon energy
dk	Wavevector spacing
delk	Wavevector step in the calculation
k	Wavevector
E	Energy
vf	Fermi velocity
muguess	Guess of chemical potential
kp	The state with hbaromega higher than state k
kn	The state with hbaromega lower than state k
jp	Index of kp
jn	Index of kn
ip	Limit of jp
in	Limit of jn
lpb	Optical or zone-boundary phonon scattering length
le	Acoustic phonon scattering length
dt	Time interval of every iteration

kgain	The increase of k due to electric field
igain	Corresponding index increase of kgain
v	Average carrier velocity
g	Nonequilibrium carrier distribution
Count	Number of iteration

Table B-2. Symbols using in Section B-3.

Bibliography

[1] S. Iijima. Helical Microtubules of Graphitic Carbon. *Nature* **354**, 56-58 (1991).

[2] C. Dekker. Carbon nanotubes as molecular quantum wires. *Physics Today* **52**, 22-28 (1999).

[3] P. L. McEuen, M. S. Fuhrer, and H. K. Park. Single-walled carbon nanotube electronics. *Ieee Transactions on Nanotechnology* **1**, 78-85 (2002).

[4] S. Iijima and T. Ichihashi. Single-Shell Carbon Nanotubes of 1-Nm Diameter. *Nature* **363**, 603-605 (1993).

[5] M. M. J. Treacy, T. W. Ebbesen, and J. M. Gibson. Exceptionally high Young's modulus observed for individual carbon nanotubes. *Nature* **381**, 678-680 (1996).

[6] E. W. Wong, P. E. Sheehan, and C. M. Lieber. Nanobeam mechanics: Elasticity, strength, and toughness of nanorods and nanotubes. *Science* **277**, 1971-1975 (1997).

[7] J. Kong, N. R. Franklin, C. W. Zhou, M. G. Chapline, S. Peng, K. J. Cho, and H. J. Dai. Nanotube molecular wires as chemical sensors. *Science* **287**, 622-625 (2000).

[8] P. G. Collins, K. Bradley, M. Ishigami, and A. Zettl. Extreme oxygen sensitivity of electronic properties of carbon nanotubes. *Science* **287**, 1801-1804 (2000).

[9] S. Chopra, K. McGuire, N. Gothard, A. M. Rao, and A. Pham. Selective gas detection using a carbon nanotube sensor. *Applied Physics Letters* **83**, 2280-2282 (2003).

[10] N. Hamada, S. Sawada, and A. Oshiyama. New One-Dimensional Conductors - Graphitic Microtubules. *Physical Review Letters* **68**, 1579-1581 (1992).

[11] C. L. Kane and M. P. A. Fisher. Transport in a One-Channel Luttinger Liquid. *Physical Review Letters* **68**, 1220-1223 (1992).

[12] J. W. Mintmire, B. I. Dunlap, and C. T. White. Are Fullerene Tubules Metallic. *Physical Review Letters* **68**, 631-634 (1992).

[13] T. W. Odom, J. L. Huang, P. Kim, M. Ouyang, and C. M. Lieber. Scanning tunneling microscopy and spectroscopy studies of single wall carbon nanotubes. *Journal of Materials Research* **13**, 2380-2388 (1998).

[14] T. W. Odom, J. L. Huang, P. Kim, and C. M. Lieber. Atomic structure and electronic properties of single-walled carbon nanotubes. *Nature* **391**, 62-64 (1998).

[15] J. W. G. Wildoer, L. C. Venema, A. G. Rinzler, R. E. Smalley, and C. Dekker. Electronic structure of atomically resolved carbon nanotubes. *Nature* **391**, 59-62 (1998).

[16] S. J. Tans, A. R. M. Verschueren, and C. Dekker. Room-temperature transistor based on a single carbon nanotube. *Nature* **393**, 49-52 (1998).

[17] R. Martel, T. Schmidt, H. R. Shea, T. Hertel, and P. Avouris. Single- and multi-wall carbon nanotube field-effect transistors. *Applied Physics Letters* **73**, 2447-2449 (1998).

[18] J. W. Mintmire and C. T. White. Universal density of states for carbon nanotubes. *Physical Review Letters* **81**, 2506-2509 (1998).

[19] L. X. Zheng, M. J. O'Connell, S. K. Doorn, X. Z. Liao, Y. H. Zhao, E. A. Akhadov, M. A. Hoffbauer, B. J. Roop, Q. X. Jia, R. C. Dye, D. E. Peterson, S. M. Huang, J. Liu, and Y. T. Zhu. Ultralong single-wall carbon nanotubes. *Nature Materials* **3**, 673-676 (2004).

[20] B. H. Hong, J. Y. Lee, T. Beetz, Y. M. Zhu, P. Kim, and K. S. Kim. Quasi-continuous growth of ultralong carbon nanotube arrays. *Journal of the American Chemical Society* **127**, 15336-15337 (2005).

[21] B. I. Yakobson and P. Avouris, in *Carbon Nanotubes* (SPRINGER-VERLAG BERLIN, Berlin, 2001), Vol. 80, p. 287-327.

[22] P. Miaudet, S. Badaire, M. Maugey, A. Derre, V. Pichot, P. Launois, P. Poulin, and C. Zakri. Hot-drawing of single and multiwall carbon nanotube fibers for high toughness and alignment. *Nano Letters* **5**, 2212-2215 (2005).

[23] B. I. Yakobson and R. E. Smalley. Fullerene nanotubes: C-1000000 and beyond. *American Scientist* **85**, 324-337 (1997).

[24] C. L. Kane and E. J. Mele. Size, shape, and low energy electronic structure of carbon nanotubes. *Physical Review Letters* **78**, 1932-1935 (1997).

[25] M. S. Fuhrer, J. Nygard, L. Shih, M. Forero, Y. G. Yoon, M. S. C. Mazzoni, H. J. Choi, J. Ihm, S. G. Louie, A. Zettl, and P. L. McEuen. Crossed nanotube junctions. *Science* **288**, 494-497 (2000).

[26] H. W. C. Postma, T. Teepen, Z. Yao, M. Grifoni, and C. Dekker. Carbon nanotube single-electron transistors at room temperature. *Science* **293**, 76-79 (2001).

[27] J. U. Lee, P. P. Gipp, and C. M. Heller. Carbon nanotube p-n junction diodes. *Applied Physics Letters* **85**, 145-147 (2004).

[28] T. Durkop, S. A. Getty, E. Cobas, and M. S. Fuhrer. Extraordinary mobility in semiconducting carbon nanotubes. *Nano Letters* **4**, 35-39 (2004).

[29] M. S. Fuhrer, B. M. Kim, T. Durkop, and T. Brintlinger. High-mobility nanotube transistor memory. *Nano Letters* **2**, 755-759 (2002).

[30] W. A. Deheer, A. Chatelain, and D. Ugarte. A Carbon Nanotube Field-Emission Electron Source. *Science* **270**, 1179-1180 (1995).

[31] A. G. Rinzler, J. H. Hafner, P. Nikolaev, L. Lou, S. G. Kim, D. Tomanek, P. Nordlander, D. T. Colbert, and R. E. Smalley. Unraveling Nanotubes - Field-Emission from an Atomic Wire. *Science* **269**, 1550-1553 (1995).

[32] J. M. Luttinger. An Exactly Soluble Model of a Many-Fermion System. *Journal of Mathematical Physics* **4**, 1154 (1963).

[33] M. Bockrath, D. H. Cobden, J. Lu, A. G. Rinzler, R. E. Smalley, T. Balents, and P. L. McEuen. Luttinger-liquid behaviour in carbon nanotubes. *Nature* **397**, 598-601 (1999).

[34] Z. Yao, H. W. C. Postma, L. Balents, and C. Dekker. Carbon nanotube intramolecular junctions. *Nature* **402**, 273-276 (1999).

[35] K. Tsukagoshi, B. W. Alphenaar, and H. Ago. Coherent transport of electron spin in a ferromagnetically contacted carbon nanotube. *Nature* **401**, 572-574 (1999).

[36] N. Tombros, S. J. v. d. Molen, and B. J. v. Wees. Separating spin and charge transport in single wall carbon nanotubes. *cond-mat*, 0506538 (2005).

[37] B. Nagabhirava, T. Bansal, G. U. Sumanasekera, B. W. Alphenaar, and L. Liu. Gated spin transport through an individual single wall carbon nanotube. *Applied Physics Letters* **88**, 023503 (2006).

[38] P. R. Wallace. The Band Theory of Graphite. *Physical Review* **71**, 622-634 (1947).

[39] A. G. Souza, A. Jorio, J. H. Hafner, C. M. Lieber, R. Saito, M. A. Pimenta, G. Dresselhaus, and M. S. Dresselhaus. Electronic transition energy E-ii for an

isolated (n,m) single-wall carbon nanotube obtained by anti-Stokes/Stokes resonant Raman intensity ratio. *Physical Review B* **63**, 241404 (2001).

[40] M. S. Dresselhaus, G. Dresselhaus, and P. C. Eklund, *Science of fullerenes and carbon nanotubes* Academic Press, San Diego, 1996.

[41] R. Saito, G. Dresselhaus, and M. S. Dresselhaus, *Physical properties of carbon nanotubes* Imperial College Press, London, 1998.

[42] A. Bachtold, M. S. Fuhrer, S. Plyasunov, M. Forero, E. H. Anderson, A. Zettl, and P. L. McEuen. Scanned probe microscopy of electronic transport in carbon nanotubes. *Physical Review Letters* **84**, 6082-6085 (2000).

[43] D. Mann, A. Javey, J. Kong, Q. Wang, and H. J. Dai. Ballistic transport in metallic nanotubes with reliable Pd ohmic contacts. *Nano Letters* **3**, 1541-1544 (2003).

[44] A. Javey, J. Guo, Q. Wang, M. Lundstrom, and H. J. Dai. Ballistic carbon nanotube field-effect transistors. *Nature* **424**, 654-657 (2003).

[45] Z. Yao, C. L. Kane, and C. Dekker. High-field electrical transport in single-wall carbon nanotubes. *Physical Review Letters* **84**, 2941-2944 (2000).

[46] Y. F. Chen and M. S. Fuhrer. Electric-field-dependent charge-carrier velocity in semiconducting carbon nanotubes. *Physical Review Letters* **95**, 236803 (2005).

[47] A. Javey, J. Guo, M. Paulsson, Q. Wang, D. Mann, M. Lundstrom, and H. J. Dai. High-field quasiballistic transport in short carbon nanotubes. *Physical Review Letters* **92**, 106804 (2004).

[48] B. Q. Wei, R. Vajtai, and P. M. Ajayan. Reliability and current carrying capacity of carbon nanotubes. *Applied Physics Letters* **79**, 1172-1174 (2001).

[49] M. Freitag, J. Chen, J. Tersoff, J. C. Tsang, Q. Fu, J. Liu, and P. Avouris. Mobile ambipolar domain in carbon-nanotube infrared emitters. *Physical Review Letters* **93**, 076803 (2004).

[50] B. M. Kim, Y.-F. Chen, and M. S. Fuhrer, in *ECS*, edited by P. Kamat, D. Guldi and K. Kadish (ECS, 2002), Vol. 12, p. 541-548.

[51] Y. F. Chen and M. S. Fuhrer. Doping Provides High On-Currents in Schottky-Barrier Nanotube Transistors. *submitted to Applied Physics Letters* (2006).

[52] A. Thess, R. Lee, P. Nikolaev, H. J. Dai, P. Petit, J. Robert, C. H. Xu, Y. H. Lee, S. G. Kim, A. G. Rinzler, D. T. Colbert, G. E. Scuseria, D. Tomanek, J. E. Fischer, and R. E. Smalley. Crystalline ropes of metallic carbon nanotubes. *Science* **273**, 483-487 (1996).

[53] J. Kong, A. M. Cassell, and H. J. Dai. Chemical vapor deposition of methane for single-walled carbon nanotubes. *Chemical Physics Letters* **292**, 567-574 (1998).

[54] J. Kong, H. T. Soh, A. M. Cassell, C. F. Quate, and H. J. Dai. Synthesis of individual single-walled carbon nanotubes on patterned silicon wafers. *Nature* **395**, 878-881 (1998).

[55] J. Cao, Q. Wang, and H. Dai. Electron transport in very clean, as-grown suspended carbon nanotubes. *Nature Materials* **4**, 745-749 (2005).

[56] D. E. Resasco, W. E. Alvarez, F. Pompeo, L. Balzano, J. E. Herrera, B. Kitiyanan, and A. Borgna. A scalable process for production of single-walled carbon nanotubes (SWNTs) by catalytic disproportionation of CO on a solid catalyst. *Journal of Nanoparticle Research* **4**, 131-136 (2002).

[57] J. H. Hafner, C. L. Cheung, T. H. Oosterkamp, and C. M. Lieber. High-yield assembly of individual single-walled carbon nanotube tips for scanning probe microscopies. *Journal of Physical Chemistry B* **105**, 743-746 (2001).

[58] H. Dai, A. G. Rinzler, P. Nikolaev, A. Thess, D. T. Colbert, and R. E. Smalley. Single-wall nanotubes produced by metal-catalyzed disproportionation of carbon monoxide. *Chemical Physics Letters* **260**, 471-475 (1996).

[59] T. Brintlinger, Y. F. Chen, T. Durkop, E. Cobas, M. S. Fuhrer, J. D. Barry, and J. Melngailis. Rapid imaging of nanotubes on insulating substrates. *Applied Physics Letters* **81**, 2454-2456 (2002).

[60] S. Rosenblatt, Y. Yaish, J. Park, J. Gore, V. Sazonova, and P. L. McEuen. High performance electrolyte gated carbon nanotube transistors. *Nano Letters* **2**, 869-872 (2002).

[61] G. Binning, H. Rohrer, C. Gerber, and E. Weibel. Surface Studies by Scanning Tunneling Microscopy. *Physical Review Letters* **49**, 57-61 (1982).

[62] G. Binnig, H. Rohrer, C. Gerber, and E. Weibel. 7x7 Reconstruction on Si(111) Resolved in Real Space. *Physical Review Letters* **50**, 120-123 (1983).

[63] G. Binnig, C. F. Quate, and C. Gerber. Atomic Force Microscope. *Physical Review Letters* **56**, 930-933 (1986).

[64] F. J. Giessibl. Atomic-Resolution of the Silicon (111)-(7x7) Surface by Atomic-Force Microscopy. *Science* **267**, 68-71 (1995).

[65] D. Rugar and P. Hansma. Atomic Force Microscopy. *Physics Today* **43**, 23-30 (1990).

[66] F. J. Giessibl. Advances in atomic force microscopy. *Reviews of Modern Physics* **75**, 949-983 (2003).

[67] P. J. de Pablo, C. Gomez-Navarro, A. Gil, J. Colchero, M. T. Martinez, A. M. Benito, W. K. Maser, J. Gomez-Herrero, and A. M. Baro. Visualization of single-walled carbon nanotubes electrical networks by scanning force microspy. *Applied Physics Letters* **79**, 2979-2981 (2001).

[68] P. J. de Pablo, C. Gomez-Navarro, J. Colchero, P. A. Serena, J. Gomez-Herrero, and A. M. Baro. Nonlinear resistance versus length in single-walled carbon nanotubes. *Physical Review Letters* **88**, 036804 (2002).

[69] J. Y. Park, S. Rosenblatt, Y. Yaish, V. Sazonova, H. Ustunel, S. Braig, T. A. Arias, P. W. Brouwer, and P. L. McEuen. Electron-phonon scattering in metallic single-walled carbon nanotubes. *Nano Letters* **4**, 517-520 (2004).

[70] Y. Yaish, J. Y. Park, S. Rosenblatt, V. Sazonova, M. Brink, and P. L. McEuen. Electrical nanoprobing of semiconducting carbon nanotubes using an atomic force microscope. *Physical Review Letters* **92**, 046401 (2004).

[71] T. W. Tombler, C. W. Zhou, J. Kong, and H. J. Dai. Gating individual nanotubes and crosses with scanning probes. *Applied Physics Letters* **76**, 2412-2414 (2000).

[72] M. Freitag, M. Radosavljevic, Y. X. Zhou, A. T. Johnson, and W. F. Smith. Controlled creation of a carbon nanotube diode by a scanned gate. *Applied Physics Letters* **79**, 3326-3328 (2001).

[73] M. Bockrath, W. J. Liang, D. Bozovic, J. H. Hafner, C. M. Lieber, M. Tinkham, and H. K. Park. Resonant electron scattering by defects in single-walled carbon nanotubes. *Science* **291**, 283-285 (2001).

[74] M. Freitag, A. T. Johnson, S. V. Kalinin, and D. A. Bonnell. Role of single defects in electronic transport through carbon nanotube field-effect transistors. *Physical Review Letters* **89**, 216801 (2002).

[75] M. Bockrath, N. Markovic, A. Shepard, M. Tinkham, L. Gurevich, L. P. Kouwenhoven, M. S. W. Wu, and L. L. Sohn. Scanned conductance

microscopy of carbon nanotubes and lambda-DNA. *Nano Letters* **2**, 187-190 (2002).

[76] J. S. Heo and M. Bockrath. Local electronic structure of single-walled carbon nanotubes from electrostatic force microscopy. *Nano Letters* **5**, 853-857 (2005).

[77] Y. Martin, D. W. Abraham, and H. K. Wickramasinghe. High-Resolution Capacitance Measurement and Potentiometry by Force Microscopy. *Applied Physics Letters* **52**, 1103-1105 (1988).

[78] J. E. Stern, B. D. Terris, H. J. Mamin, and D. Rugar. Deposition and Imaging of Localized Charge on Insulator Surfaces Using a Force Microscope. *Applied Physics Letters* **53**, 2717-2719 (1988).

[79] B. D. Terris, J. E. Stern, D. Rugar, and H. J. Mamin. Contact Electrification Using Force Microscopy. *Physical Review Letters* **63**, 2669-2672 (1989).

[80] M. A. Eriksson, R. G. Beck, M. Topinka, J. A. Katine, R. M. Westervelt, K. L. Campman, and A. C. Gossard. Cryogenic scanning probe characterization of semiconductor nanostructures. *Applied Physics Letters* **69**, 671-673 (1996).

[81] R. Crook, C. G. Smith, M. Y. Simmons, and D. A. Ritchie. One-dimensional probability density observed using scanned gate microscopy. *Journal of Physics-Condensed Matter* **12**, L735-L740 (2000).

[82] N. Aoki, C. R. Da Cunha, R. Akis, D. K. Ferry, and Y. Ochiai. Scanning gate microscopy investigations on an InGaAs quantum point contact. *Applied Physics Letters* **87**, 223501 (2005).

[83] N. Aoki, C. R. da Cunha, R. Akis, D. K. Ferry, and Y. Ochiai. Imaging of integer quantum Hall edge state in a quantum point contact via scanning gate microscopy. *Physical Review B* **72**, 155327 (2005).

[84] J. W. P. Hsu, N. G. Weimann, M. J. Manfra, K. W. West, D. V. Lang, F. F. Schrey, O. Mitrofanov, and R. J. Molnar. Effect of dislocations on local transconductance in AlGaN/GaN heterostructures as imaged by scanning gate microscopy. *Applied Physics Letters* **83**, 4559-4561 (2003).

[85] S. J. Tans and C. Dekker. Molecular transistors - Potential modulations along carbon nanotubes. *Nature* **404**, 834-835 (2000).

[86] C. Staii and A. T. Johnson. High frequency scanning gate microscopy and local memory effect of carbon nanotube transistors. *Nano Letters* **5**, 893-896 (2005).

[87] C. Meyer, J. Klijn, M. Morgenstern, and R. Wiesendanger. Direct measurement of the local density of states of a disordered one-dimensional conductor. *Physical Review Letters* **91**, 076803 (2003).

[88] L. J. Guo, E. Leobandung, and S. Y. Chou. A silicon single-electron transistor memory operating at room temperature. *Science* **275**, 649-651 (1997).

[89] A. Nakajima, T. Futatsugi, K. Kosemura, T. Fukano, and N. Yokoyama. Room temperature operation of Si single-electron memory with self-aligned floating dot gate. *Applied Physics Letters* **70**, 1742-1744 (1997).

[90] H. Sunamura, T. Sakamoto, Y. Nakamura, H. Kawaura, J. S. Tsai, and T. Baba. Single-electron memory using carrier traps in a silicon nitride layer. *Applied Physics Letters* **74**, 3555-3557 (1999).

[91] K. Yano, T. Ishii, T. Sano, T. Mine, F. Murai, T. Hashimoto, T. Kobayashi, T. Kure, and K. Seki. Single-electron memory for giga-to-tera bit storage. *Proceedings of the Ieee* **87**, 633-651 (1999).

[92] S. M. Sze, *Physics of semiconductor devices*, New York, 1981.

[93] M. Julliere. Tunneling between Ferromagnetic-Films. *Physics Letters A* **54**, 225-226 (1975).

[94] G. A. Prinz. Device physics - Magnetoelectronics. *Science* **282**, 1660-1663 (1998).

[95] S. A. Wolf, D. D. Awschalom, R. A. Buhrman, J. M. Daughton, S. von Molnar, M. L. Roukes, A. Y. Chtchelkanova, and D. M. Treger. Spintronics: A spin-based electronics vision for the future. *Science* **294**, 1488-1495 (2001).

[96] S. S. P. Parkin, K. P. Roche, M. G. Samant, P. M. Rice, R. B. Beyers, R. E. Scheuerlein, E. J. O'Sullivan, S. L. Brown, J. Bucchigano, D. W. Abraham, Y. Lu, M. Rooks, P. L. Trouilloud, R. A. Wanner, and W. J. Gallagher.

Exchange-biased magnetic tunnel junctions and application to nonvolatile magnetic random access memory (invited). *Journal of Applied Physics* **85**, 5828-5833 (1999).

[97] T. Rueckes, K. Kim, E. Joselevich, G. Y. Tseng, C. L. Cheung, and C. M. Lieber. Carbon nanotube-based nonvolatile random access memory for molecular computing. *Science* **289**, 94-97 (2000).

[98] S. Datta and B. Das. Electronic Analog of the Electrooptic Modulator. *Applied Physics Letters* **56**, 665-667 (1990).

[99] F. J. Jedema, A. T. Filip, and B. J. van Wees. Electrical spin injection and accumulation at room temperature in an all-metal mesoscopic spin valve. *Nature* **410**, 345-348 (2001).

[100] F. J. Jedema, H. B. Heersche, A. T. Filip, J. J. A. Baselmans, and B. J. van Wees. Electrical detection of spin precession in a metallic mesoscopic spin valve. *Nature* **416**, 713-716 (2002).

[101] J. M. Kikkawa and D. D. Awschalom. Lateral drag of spin coherence in gallium arsenide. *Nature* **397**, 139-141 (1999).

[102] G. Schmidt, D. Ferrand, L. W. Molenkamp, A. T. Filip, and B. J. van Wees. Fundamental obstacle for electrical spin injection from a ferromagnetic metal into a diffusive semiconductor. *Physical Review B* **62**, R4790-R4793 (2000).

[103] A. T. Filip, B. H. Hoving, F. J. Jedema, and B. J. van Wees. Experimental search for the electrical spin injection in a semiconductor. *Physical Review B* **62**, 9996-9999 (2000).

[104] B. Zhao, I. Monch, H. Vinzelberg, T. Muhl, and C. M. Schneider. Spin-coherent transport in ferromagnetically contacted carbon nanotubes. *Applied Physics Letters* **80**, 3144-3146 (2002).

[105] S. Sahoo, T. Kontos, C. Schonenberger, and C. Surgers. Electrical spin injection in multiwall carbon nanotubes with transparent ferromagnetic contacts. *Applied Physics Letters* **86**, 112109 (2005).

[106] J. R. Kim, H. M. So, J. J. Kim, and J. Kim. Spin-dependent transport properties in a single-walled carbon nanotube with mesoscopic Co contacts. *Physical Review B* **66**, 233401 (2002).

[107] A. Jensen, J. R. Hauptmann, J. Nygard, J. Sadowski, and P. E. Lindelof. Hybrid devices from single wall carbon nanotubes epitaxially grown into a semiconductor heterostructure. *Nano Letters* **4**, 349-352 (2004).

[108] A. Jensen, J. R. Hauptmann, J. Nygard, and P. E. Lindelof. Magnetoresistance in ferromagnetically contacted single-wall carbon nanotubes. *Physical Review B* **72**, 038419 (2005).

[109] S. Sahoo, T. Kontos, J. Furer, C. Hoffmann, M. Graber, A. Cottet, and C. Schonenberger. Electric field control of spin transport. *Nature Physics* **1**, 99-102 (2005).

[110] R. Meservey and P. M. Tedrow. Spin-Polarized Electron-Tunneling. *Physics Reports-Review Section of Physics Letters* **238**, 173-243 (1994).

[111] D. Y. Petrovykh, K. N. Altmann, H. Hochst, M. Laubscher, S. Maat, G. J. Mankey, and F. J. Himpsel. Spin-dependent band structure, Fermi surface, and carrier lifetime of permalloy. *Applied Physics Letters* **73**, 3459-3461 (1998).

[112] R. D. Gomez, T. V. Luu, A. O. Pak, I. D. Mayergoyz, K. J. Kirk, and J. N. Chapman. Domain wall motion in micron-sized permalloy elements. *Journal of Applied Physics* **85**, 4598-4600 (1999).

[113] D. Rugar, H. J. Mamin, P. Guethner, S. E. Lambert, J. E. Stern, I. McFadyen, and T. Yogi. Magnetic Force Microscopy - General-Principles and Application to Longitudinal Recording Media. *Journal of Applied Physics* **68**, 1169-1183 (1990).

[114] C. Schonenberger and S. F. Alvarado. Understanding Magnetic Force Microscopy. *Zeitschrift Fur Physik B-Condensed Matter* **80**, 373-383 (1990).

[115] F. J. Jedema, M. S. Nijboer, A. T. Filip, and B. J. van Wees. Spin injection and spin accumulation in all-metal mesoscopic spin valves. *Physical Review B* **67**, 085319 (2003).

[116] A. A. Odintsov. Schottky barriers in carbon nanotube heterojunctions. *Physical Review Letters* **85**, 150-153 (2000).

[117] J. Guo, S. Datta, and M. Lundstrom. A numerical study of scaling issues for Schottky-Barrier carbon nanotube transistors. *Ieee Transactions on Electron Devices* **51**, 172-177 (2004).

[118] A. N. Pasupathy, R. C. Bialczak, J. Martinek, J. E. Grose, L. A. K. Donev, P. L. McEuen, and D. C. Ralph. The Kondo effect in the presence of ferromagnetism. *Science* **306**, 86-89 (2004).

[119] E. I. Rashba. Theory of electrical spin injection: Tunnel contacts as a solution of the conductivity mismatch problem. *Physical Review B* **62**, R16267-R16270 (2000).

[120] B. Bourlon, C. Miko, L. Forro, D. C. Glattli, and A. Bachtold. Determination of the intershell conductance in multiwalled carbon nanotubes. *Physical Review Letters* **93**, 176806 (2004).

[121] F. J. Jedema, M. V. Costache, H. B. Heersche, J. J. A. Baselmans, and B. J. van Wees. Electrical detection of spin accumulation and spin precession at room temperature in metallic spin valves. *Applied Physics Letters* **81**, 5162-5164 (2002).

[122] P. G. Collins, M. S. Arnold, and P. Avouris. Engineering carbon nanotubes and nanotube circuits using electrical breakdown. *Science* **292**, 706-709 (2001).

[123] D. Young and A. Christou. Failure-Mechanism Models for Electromigration. *Ieee Transactions on Reliability* **43**, 186-192 (1994).

[124] P. G. Collins, M. Hersam, M. Arnold, R. Martel, and P. Avouris. Current saturation and electrical breakdown in multiwalled carbon nanotubes. *Physical Review Letters* **86**, 3128-3131 (2001).

[125] B. Bourlon, D. C. Glattli, B. Placais, J. M. Berroir, C. Miko, L. Forro, and A. Bachtold. Geometrical dependence of high-bias current in multiwalled carbon nanotubes. *Physical Review Letters* **92**, 026804 (2004).

[126] P. Jarillo-Herrero, S. Sapmaz, C. Dekker, L. P. Kouwenhoven, and H. S. J. van der Zant. Electron-hole symmetry in a semiconducting carbon nanotube quantum dot. *Nature* **429**, 389-392 (2004).

[127] J. A. Misewich, R. Martel, P. Avouris, J. C. Tsang, S. Heinze, and J. Tersoff. Electrically induced optical emission from a carbon nanotube FET. *Science* **300**, 783-786 (2003).

[128] M. Radosavljevic, S. Heinze, J. Tersoff, and P. Avouris. Drain voltage scaling in carbon nanotube transistors. *Applied Physics Letters* **83**, 2435-2437 (2003).

[129] P. Avouris. Carbon nanotube electronics and optoelectronics. *Mrs Bulletin* **29**, 403-410 (2004).

[130] S. Datta, *Electronic transport in mesoscopic systems* Cambridge University Press, Cambridge, 1995.

[131] V. Perebeinos, J. Tersoff, and P. Avouris. Electron-phonon interaction and transport in semiconducting carbon nanotubes. *Physical Review Letters* **94**, 086802 (2005).

[132] G. Pennington and N. Goldsman. Semiclassical transport and phonon scattering of electrons in semiconducting carbon nanotubes. *Physical Review B* **68**, 045426 (2003).

[133] J. A. Cooper and D. F. Nelson. High-Field Drift Velocity of Electrons at the Si-Sio2 Interface as Determined by a Time-of-Flight Technique. *Journal of Applied Physics* **54**, 1445-1456 (1983).

[134] Y. W. Fan, B. R. Goldsmith, and P. G. Collins. Identifying and counting point defects in carbon nanotubes. *Nature Materials* **4**, 906-911 (2005).

[135] N. W. Ashcroft and N. D. Mermin, *Solid state physics* Brooks/Cole, Australia, 1976.

[136] X. J. Zhou, J. Y. Park, S. M. Huang, J. Liu, and P. L. McEuen. Band structure, phonon scattering, and the performance limit of single-walled carbon nanotube transistors. *Physical Review Letters* **95**, 146805 (2005).

[137] V. Perebeinos, J. Tersoff, and P. Avouris. Mobility in semiconducting carbon nanotubes at finite carrier density. *Nano Letters* **6**, 205-208 (2006).

[138] E. Pop, D. Mann, J. Cao, Q. Wang, K. Goodson, and H. J. Dai. Negative differential conductance and hot phonons in suspended nanotube molecular wires. *Physical Review Letters* **95**, 155505 (2005).

[139] M. Lazzeri, S. Piscanec, F. Mauri, A. C. Ferrari, and J. Robertson. Electron transport and hot phonons in carbon nanotubes. *Physical Review Letters* **95**, 236802 (2005).

[140] C. Kittel and P. McEuen, *Introduction to solid state physics* J. Wiley, Hoboken, NJ, 2005.

[141] M. Freitag, V. Perebeinos, J. Chen, A. Stein, J. C. Tsang, J. A. Misewich, R. Martel, and P. Avouris. Hot carrier electroluminescence from a single carbon nanotube. *Nano Letters* **4**, 1063-1066 (2004).

[142] J. Chen, V. Perebeinos, M. Freitag, J. Tsang, Q. Fu, J. Liu, and P. Avouris. Bright infrared emission from electrically induced excitons in carbon nanotubes. *Science* **310**, 1171-1174 (2005).

[143] C. D. Spataru, S. Ismail-Beigi, L. X. Benedict, and S. G. Louie. Excitonic effects and optical spectra of single-walled carbon nanotubes. *Physical Review Letters* **92**, 077402 (2004).

[144] C. D. Spataru, S. Ismail-Beigi, L. X. Benedict, and S. G. Louie. Quasiparticle energies, excitonic effects and optical absorption spectra of small-diameter single-walled carbon nanotubes. *Applied Physics a-Materials Science & Processing* **78**, 1129-1136 (2004).

[145] C. D. Spataru, S. Ismail-Beigi, R. B. Capaz, and S. G. Louie. Theory and ab initio calculation of radiative lifetime of excitons in semiconducting carbon nanotubes. *Physical Review Letters* **95**, 247402 (2005).

[146] V. Perebeinos, J. Tersoff, and P. Avouris. Scaling of excitons in carbon nanotubes. *Physical Review Letters* **92**, 257402 (2004).

[147] V. Perebeinos, J. Tersoff, and P. Avouris. Radiative lifetime of excitons in carbon nanotubes. *Nano Letters* **5**, 2495-2499 (2005).

[148] C. L. Kane and E. J. Mele. Electron interactions and scaling relations for optical excitations in carbon nanotubes. *Physical Review Letters* **93**, 197402 (2004).

[149] V. Perebeinos, J. Tersoff, and P. Avouris. Effect of exciton-phonon coupling in the calculated optical absorption of carbon nanotubes. *Physical Review Letters* **94**, 027402 (2005).

[150] Y. Z. Ma, L. Valkunas, S. L. Dexheimer, S. M. Bachilo, and G. R. Fleming. Femtosecond spectroscopy of optical excitations in single-walled carbon nanotubes: Evidence for exciton-exciton annihilation. *Physical Review Letters* **94**, 157402 (2005).

[151] J. Lefebvre, Y. Homma, and P. Finnie. Bright band gap photoluminescence from unprocessed single-walled carbon nanotubes. *Physical Review Letters* **90**, 217401 (2003).

[152] G. N. Ostojic, S. Zaric, J. Kono, M. S. Strano, V. C. Moore, R. H. Hauge, and R. E. Smalley. Interband recombination dynamics in resonantly excited single-walled carbon nanotubes. *Physical Review Letters* **92** (2004).

[153] J. Tersoff, M. Freitag, J. C. Tsang, and P. Avouris. Device modeling of long-channel nanotube electro-optical emitter. *Applied Physics Letters* **86**, 263108 (2005).

[154] J. Guo and M. A. Alam. Carrier transport and light-spot movement in carbon-nanotube infrared emitters. *Applied Physics Letters* **86**, 023105 (2005).

[155] A. Rahman, J. Guo, S. Datta, and M. S. Lundstrom. Theory of ballistic nanotransistors. *Ieee Transactions on Electron Devices* **50**, 1853-1864 (2003).

[156] F. Leonard and J. Tersoff. Novel length scales in nanotube devices. *Physical Review Letters* **83**, 5174-5177 (1999).

[157] S. Heinze, J. Tersoff, R. Martel, V. Derycke, J. Appenzeller, and P. Avouris. Carbon nanotubes as Schottky barrier transistors. *Physical Review Letters* **89**, 106801 (2002).

[158] J. Appenzeller, J. Knoch, V. Derycke, R. Martel, S. Wind, and P. Avouris. Field-modulated carrier transport in carbon nanotube transistors. *Physical Review Letters* **89**, 126801 (2002).

[159] V. Derycke, R. Martel, J. Appenzeller, and P. Avouris. Carbon nanotube inter- and intramolecular logic gates. *Nano Letters* **1**, 453-456 (2001).

[160] V. Derycke, R. Martel, J. Appenzeller, and P. Avouris. Controlling doping and carrier injection in carbon nanotube transistors. *Applied Physics Letters* **80**, 2773-2775 (2002).

[161] S. J. Wind, J. Appenzeller, R. Martel, V. Derycke, and P. Avouris. Vertical scaling of carbon nanotube field-effect transistors using top gate electrodes. *Applied Physics Letters* **80**, 3817-3819 (2002).

[162] R. Martel, V. Derycke, C. Lavoie, J. Appenzeller, K. K. Chan, J. Tersoff, and P. Avouris. Ambipolar electrical transport in semiconducting single-wall carbon nanotubes. *Physical Review Letters* **87**, 256805 (2001).

[163] J. Appenzeller, M. Radosavljevic, J. Knoch, and P. Avouris. Tunneling versus thermionic emission in one-dimensional semiconductors. *Physical Review Letters* **92**, 048301 (2004).

[164] A. Javey, M. Shim, and H. J. Dai. Electrical properties and devices of large-diameter single-walled carbon nanotubes. *Applied Physics Letters* **80**, 1064-1066 (2002).

[165] S. H. Jhi, S. G. Louie, and M. L. Cohen. Electronic properties of oxidized carbon nanotubes. *Physical Review Letters* **85**, 1710-1713 (2000).

[166] E. D. Minot, Y. Yaish, V. Sazonova, and P. L. McEuen. Determination of electron orbital magnetic moments in carbon nanotubes. *Nature* **428**, 536-539 (2004).

[167] K. S. Novoselov, A. K. Geim, S. V. Morozov, D. Jiang, Y. Zhang, S. V. Dubonos, I. V. Grigorieva, and A. A. Firsov. Electric field effect in atomically thin carbon films. *Science* **306**, 666-669 (2004).

[168] C. Berger, Z. M. Song, T. B. Li, X. B. Li, A. Y. Ogbazghi, R. Feng, Z. T. Dai, A. N. Marchenkov, E. H. Conrad, P. N. First, and W. A. de Heer. Ultrathin epitaxial graphite: 2D electron gas properties and a route toward graphene-based nanoelectronics. *Journal of Physical Chemistry B* **108**, 19912-19916 (2004).

[169] Y. B. Zhang, J. P. Small, M. E. S. Amori, and P. Kim. Electric field modulation of galvanomagnetic properties of mesoscopic graphite. *Physical Review Letters* **94**, 176803 (2005).

[170] Y. B. Zhang, J. P. Small, W. V. Pontius, and P. Kim. Fabrication and electric-field-dependent transport measurements of mesoscopic graphite devices. *Applied Physics Letters* **86**, 073104 (2005).

[171] Y. B. Zhang, Y. W. Tan, H. L. Stormer, and P. Kim. Experimental observation of the quantum Hall effect and Berry's phase in graphene. *Nature* **438**, 201-204 (2005).

[172] K. S. Novoselov, A. K. Geim, S. V. Morozov, D. Jiang, M. I. Katsnelson, I. V. Grigorieva, S. V. Dubonos, and A. A. Firsov. Two-dimensional gas of massless Dirac fermions in graphene. *Nature* **438**, 197-200 (2005).

[173] S. V. Morozov, K. S. Novoselov, F. Schedin, D. Jiang, A. A. Firsov, and A. K. Geim. Two-dimensional electron and hole gases at the surface of graphite. *Physical Review B* **72**, 201401 (2005).

[174] K. S. Novoselov, E. McCann, S. V. Morozov, V. I. Fal'ko, M. I. Katsnelson, U. Zeitler, D. Jiang, F. Schedin, and A. K. Geim. Unconventional quantum Hall effect and Berry's phase of 2 pi in bilayer graphene. *Nature Physics* **2**, 177-180 (2006).

[175] Y. Zhang, Z. Jiang, J. P. Small, M. S. Purewal, Y. W. Tan, M. Fazlollahi, J. D. Chudow, J. A. Jaszczak, H. L. Stormer, and P. Kim. Landau-level splitting in graphene in high magnetic fields. *Physical Review Letters* **96**, 136806 (2006).